NASA/TM–20210024095

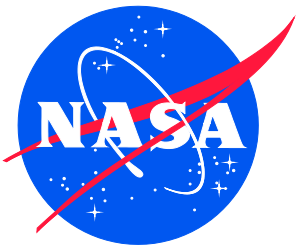

Buckling Test and Analysis of the 8-Foot-Diameter Sandwich Composite Cylinder Test Article CTA8.2 as Part of the Shell Buckling Knockdown Factor Project: Test Dates 5–7 December 2017

Adam Przekop, Marc R. Schultz, Cyrus J. R. Kosztowny, Nathaniel W. Gardner, and Kyongchan Song
Langley Research Center, Hampton, Virginia

Michelle Tillotson Rudd
George C. Marshall Space Flight Center, Huntsville, Alabama

May 2022

NASA STI Program Report Series

Since its founding, NASA has been dedicated to the advancement of aeronautics and space science. The NASA scientific and technical information (STI) program plays a key part in helping NASA maintain this important role.

The NASA STI program operates under the auspices of the Agency Chief Information Officer. It collects, organizes, provides for archiving, and disseminates NASA's STI. The NASA STI program provides access to the NTRS Registered and its public interface, the NASA Technical Reports Server, thus providing one of the largest collections of aeronautical and space science STI in the world. Results are published in both non-NASA channels and by NASA in the NASA STI Report Series, which includes the following report types:

- TECHNICAL PUBLICATION. Reports of completed research or a major significant phase of research that present the results of NASA Programs and include extensive data or theoretical analysis. Includes compilations of significant scientific and technical data and information deemed to be of continuing reference value. NASA counterpart of peer-reviewed formal professional papers but has less stringent limitations on manuscript length and extent of graphic presentations.

- TECHNICAL MEMORANDUM. Scientific and technical findings that are preliminary or of specialized interest, e.g., quick release reports, working papers, and bibliographies that contain minimal annotation. Does not contain extensive analysis.

- CONTRACTOR REPORT. Scientific and technical findings by NASA-sponsored contractors and grantees.

- CONFERENCE PUBLICATION. Collected papers from scientific and technical conferences, symposia, seminars, or other meetings sponsored or co-sponsored by NASA.

- SPECIAL PUBLICATION. Scientific, technical, or historical information from NASA programs, projects, and missions, often concerned with subjects having substantial public interest.

- TECHNICAL TRANSLATION. English-language translations of foreign scientific and technical material pertinent to NASA's mission.

Specialized services also include organizing and publishing research results, distributing specialized research announcements and feeds, providing information desk and personal search support, and enabling data exchange services.

For more information about the NASA STI program, see the following:

- Access the NASA STI program home page at http://www.sti.nasa.gov

- Help desk contact information:

https://www.sti.nasa.gov/sti-contact-form/
and select the "General" help request type.

NASA/TM–20210024095

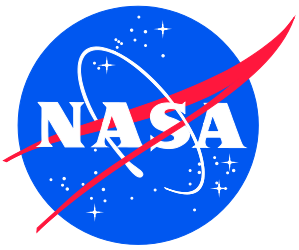

Buckling Test and Analysis of the 8-Foot-Diameter Sandwich Composite Cylinder Test Article CTA8.2 as Part of the Shell Buckling Knockdown Factor Project: Test Dates 5–7 December 2017

Adam Przekop, Marc R. Schultz, Cyrus J. R. Kosztowny, Nathaniel W. Gardner,and Kyongchan Song
Langley Research Center, Hampton, Virginia

Michelle Tillotson Rudd
George C. Marshall Space Flight Center, Huntsville, Alabama

National Aeronautics and
Space Administration

Langley Research Center
Hampton, Virginia 23681-2199

May 2022

Acknowledgements

This work was conducted as part of the NASA Engineering and Safety Center (NESC) Shell Buckling Knockdown Factor Project, NESC assessment number 07-010-E.

The CTA8.2 test article discussed herein was manufactured in an autoclave process by the Composite Technology Center at MSFC (EM42). Dr. Will Guin, Dr. John Bausano, and Mr. Justin Jackson were instrumental in the fabrication and posttest investigation of CTA8.2. Their eagerness and willingness to support the needs of the project is greatly appreciated.

The testing was performed under the direction of Mr. Lucas Day by the Structural Strength Test Group (ET30) at MSFC. The authors thank the test team at MSFC, led by Mr. Lucas Day, for dedicated support of the test activities, including instrumentation of the test article.

The authors wish to acknowledge Mr. Francisco Peña and Mr. Allen R. Parker (both from NASA Armstrong Flight Research Center, Edwards, CA) for facilitating fiberoptic measurements during the CTA8.2 tests.

The authors also acknowledge Mr. Michael C. Lindell (NASA Langley Research Center, Hampton, VA) for providing Python scripts for postprocessing of Abaqus FEA results and for the development of the global-local FEM of the test article.

Available from:

NASA STI Program / Mail Stop 148
NASA Langley Research Center
Hampton, VA 23681-2199
Fax: 757-864-6500

Table of Contents

List of Figures

List of Tables

Nomenclature

3D	Three-dimensional
AFP	Automated fiber placement
AFT	Aft or bottom end of test article
CTA8.2	Cylindrical Sandwich Composite Test Article SBKF-P3-CYL-CTA8.2
D312	LaRC Structural Mechanics and Concepts Branch
DAS	Data Acquisition System
DIC	Digital Image Correlation
DoF	Degree of Freedom
EDI	Electronic Displacement Indicator
EM42	MSFC Advanced Manufacturing Group
ET30	MSFC Structural Strength Test Group
FEA	Finite-element Analysis
FEM	Finite-element Model
fps	Frames per Second
FOSS	Fiber Optic Strain Sensing
FWD	Forward or Top End of Test Article
gsm	Grams per Square Meter
HS	High Speed
HS-DIC	High-speed Digital Image Correlation
IML	Inner Mold Line
in	Inch
kips	1,000 Pounds of Force
LaRC	Langley Research Center
lb	Pound
lbf	Pound Force
LCS	Load Control System
LS	Load Sequence
LTAE	Load Test Annex East
M_{cr}	Linear critical buckling bending moment corresponding to the linear critical axial buckling load
min	Minute
ms	Millisecond
MSFC	Marshall Space Flight Center
NESC	NASA Engineering and Safety Center
OML	Outer Mold Line
P_{cr}	Buckling Load
P_{cr}^{CF}	Closed-form Buckling Load, defined by Eq. (B1)
P_{cr}^{NL}	Geometrically nonlinear global buckling load obtained from finite-element analysis
P_{CS}	Core-shear-instability Load, defined by Eq. (B8)
P_{FD}	Facesheet Dimpling Load, defined by Eq. (B7)
P_{FW}	Facesheet Wrinkling Load, defined by Eq. (B6)
psf	Pounds per Square Foot
S	In-plane Shear Lamina Strength
SBKF	Shell Buckling Knockdown Factor Project
sec	Second

TCP	Test and Checkout Procedure
u	Axial Displacement
X_c	Compressive Lamina Strength in Fiber Direction
X_t	Tensile Lamina Strength in Fiber Direction
Y_c	Compressive Lamina Strength in Direction Perpendicular to Fiber
Y_t	Tensile Lamina Strength in Direction Perpendicular to Fiber
w	Radial Displacement
ε_{xx}	Axial Strain
ε_{yy}	Hoop Strain
δ_{DxxxA}	Axial displacement measurements measured with or calculated from electronic displacement indicators

1.0 Introduction

The buckling response of thin-shell cylinders can be sensitive to small imperfections in the geometry and loading, and has been researched and documented in Reference 1. The NASA Engineering and Safety Center (NESC) Shell Buckling Knockdown Factor Project (SBKF), in NESC Assessment 07-010-E, had the goal of developing buckling design recommendations for select classes of metallic and composite shells. A subset of the completed SBKF work is described in this report. In particular, the test and analysis results from the second SBKF composite test article, SBKF-P3-CYL-CTA8.2, which is herein referred to as CTA8.2, are described. This test was the second in a series of tests on sandwich composite cylinders that can be used to experimentally validate analysis methods, which in turn can be used to develop analysis-based shell buckling design guidelines for sandwich composite launch-vehicle cylindrical structures. CTA8.2 was an 8-ft-diameter honeycomb-core sandwich cylinder that was fabricated and tested at the NASA Marshall Space Flight Center (MSFC). The primary objectives of this test were to interrogate the structural capability of the composite test article, and to verify the test-article design and analysis approach for cylinders subjected to axial compression loads.

Descriptions of the test-article design, fabrication, and test are given in Section 2. The pretest modeling and analysis methods, and corresponding results used in support of the test-article design and test planning, are described in Section 3. Additional posttest modeling and analysis efforts and results are described in Section 4. Selected test results are compared to pretest predictions and posttest analyses in Sections 3 and 4, respectively. Concluding remarks are presented in Section 5. Supplemental information is provided in the appendices.

2.0 Test Description

Test article CTA8.2 was designed by SBKF researchers at the NASA Langley Research Center (LaRC) Structural Mechanics and Concepts Branch (D312). The testing of CTA8.2 occurred at MSFC in Building 4619 Load Test Annex East (LTAE) under the direction of the Structural Strength Test Group (ET30). A special-purpose test apparatus was designed and fabricated for the SBKF test effort. In the tests described herein, a multichannel load control system (LCS) was used to apply the test loads and included load control and displacement control options. Conventional strain and displacement data were obtained from 256 locations on the test article, fiber-optic strain data were obtained from approximately 1214 locations, and full-field displacement data were obtained on the test article outer mold line (OML) by using low-speed and high-speed (HS) digital image correlation (DIC) systems. This section provides a brief overview of the test objectives, test article, instrumentation, test facility, and test load cases. Additional details on the testing of CTA8.2 can be found in the test plan and test procedure (References 2 and 3, respectively).

The test article and corresponding test system and facilities were designed to enable the buckling testing of relevant launch-vehicle-like, thin-walled cylindrical structures. The test article was designed to be representative of a typical composite launch-vehicle cylinder. However, it was not designed to be representative of any specific structure. A testing apparatus was designed and fabricated at MSFC to support experimentation on large cylindrical structures. In particular, the test apparatus was designed to test 8-ft-diameter cylinders subjected to uniform compression loads, or combined compression and bending loads, and in the presence of up to 10 psi internal pressure. The test fixtures are rated to a maximum axial load of 1.5 million pounds in compression.

2.1 Test Objectives

The CTA8.2 test article was the second composite test article designed and tested as part of SBKF. The primary objectives were to

1. Obtain test data to verify the predicted behavioral characteristics of the as-designed, as-built cylinder subjected to an axial compression load.
2. Obtain test data for analysis tool and model validation.

2.2 Test Article

The 8-ft-diameter, 100-in-long test article was manufactured in an autoclave process in the Composite Technology Center at MSFC by the Advanced Manufacturing Group (EM42). The test article design is shown in the manufacturing drawing, Figure A1 of Appendix A. The test article was a honeycomb-core sandwich composite shell constructed with carbon-epoxy faces (IM7/8552-1) and an aluminum core (Hexcel 3.1-1/8-0.0007N-5056)[ϕ]. The quasi-isotropic 6-ply faces had a layup of $[\pm 60/0]_s$ and the core was 0.20 in. thick. The cylinder had co-cured padup plies at each end. The approximate weight of the trimmed test article without the metallic load introduction fixtures was 208.5 lb. The nominal weight of the design was estimated at 207.0 lb; however, this estimate did not include Henkel Hysol EA 9396 paste epoxy adhesive used to fill in honeycomb core splices up to 0.25 in. in width. The trimmed test article (Figure A2 of Appendix A) was potted in pi-cross-section aluminum attachment rings (Figure A3 of Appendix A) as shown in Figure A4 of Appendix A. These aluminum attachment rings were similar to the steel attachment rings described in Reference 4 that were used for the SBKF stiffened metallic test articles.

2.2.1 Design

The CTA8.2 test article was designed to fail by global buckling rather than by material strength failure or by local stability failures. As such, the maximum-strain material failure criterion was used, as were standard sandwich composite failure criteria to check for core shear failure, facesheet wrinkling, and facesheet dimpling. Padups (additional plies within sandwich faces) at either end of the test article were designed to aid in load introduction by reducing the displacements and strains in the test article as it interfaced with the much stiffer end attachment rings, thus reducing the localized response characteristics near the ends of the cylinder.

The fabrication drawing of CTA8.2 is shown in Figure A1 of Appendix A, where the as-manufactured cylinder includes an extra 2 in. of manufacturing runouts at each end that were trimmed off after cure according to the trim drawing, Figure A2 of Appendix A. The quasi-isotropic 6-ply faces were made of 190-gsm Hexcel IM7/8552-1 prepreg and had the acreage layup of $[60/-60/0]_s$. The aluminum honeycomb core was 0.20-in-thick Hexcel 3.1-1/8-0.0007N-5056 with Henkel Hysol EA 9396.6MD epoxy paste adhesive used for the core splices. The core-to-face bond was made using a thin 0.06-psf Cytec FM 2009-1M adhesive film. The padups were designed on both the forward (FWD) and aft (AFT) ends of the cylinder, on both the inner mold line (IML) and OML facesheets. In the first 13.5 in. from the ends (all dimensions here and subsequently given are in the trimmed configuration; i.e., after removing 2 in. from each end according to Figure A2 of Appendix A), both IML and OML padups comprised four plies interleaved with the acreage plies resulting in the layup shown in the bottom row of Table 1. One padup ply was dropped from the IML and OML facesheets at intervals 13.5 in., 14.5 in., 18.0 in., and 20.0 in. The laminations

[ϕ] The mention of a company or product is not an endorsement by NASA.

corresponding to each of the intervals ranges are also shown in Table 1. Since only a single 45° or –45° padup ply would be dropped at the time, the facesheet laminations between 13.5-in. and 20.0-in. stations were not symmetric. However, the IML and OML facesheet laminations were symmetric about the core surface. Furthermore, since the test article was built on a constant diameter tool, the additional thickness of the padups was built up toward the outside only. The remaining acreage region between the padups was 60-in. long.

Table 1. Layups in acreage and padup regions of the IML facesheet (padup plies in bold).

CTA8.2 cylinder sections measured from cylinder ends, in.	**IML* facesheet layup, degrees**
Beyond 20.0 (Acreage)	[60/–60/0/0/–60/60]
18.0 to 20.0	[60/–60/**45**/0/0/–60/60]
14.5 to 18.0	[60/–60/**45**/0/0/–60/–**45**/60]
13.5 to 14.5	[60/–60/**45**/0/0/**45**/–60/–**45**/60]
0 to 13.5	[60/–**45**/–60/**45**/0/0/**45**/–60/-**45**/60]

*OML facesheet layup is symmetric about the cylinder wall midsurface relative to IML layup.

2.2.2 Fabrication

Test article CTA8.2 was fabricated in June 2017 at the Composite Technology Center at MSFC as a complete cylinder on a male aluminum cylindrical tool, as shown in Figure 1. The automated fiber placement (AFP) technique was used to lay up the IML and OML faces, including both acreage and padup plies. After placing the IML acreage and padup plies, the adhesive film was placed manually followed by the 15 segments of the core joined together using the epoxy paste adhesive. After this core placement was completed in several incremental steps, and all epoxy paste adhesive was cured, another layer of adhesive film was placed on top of the core. This step was followed by AFP application of the OML acreage and padup plies. Several debulks were applied during the layup process. Apart from the debulks planned to be performed before the layup process started, some additional debulks were added based on specific ply condition or due to longer pauses in the layup process, e.g., overnight. The entire cylinder was consolidated in the autoclave under vacuum pressure and a temperature of 350°F. The final operations after the cure included trimming to the desired length and machining holes for installation in the metallic top (FWD) and bottom (AFT) attachment rings. The entire process is illustrated in Figure 2.

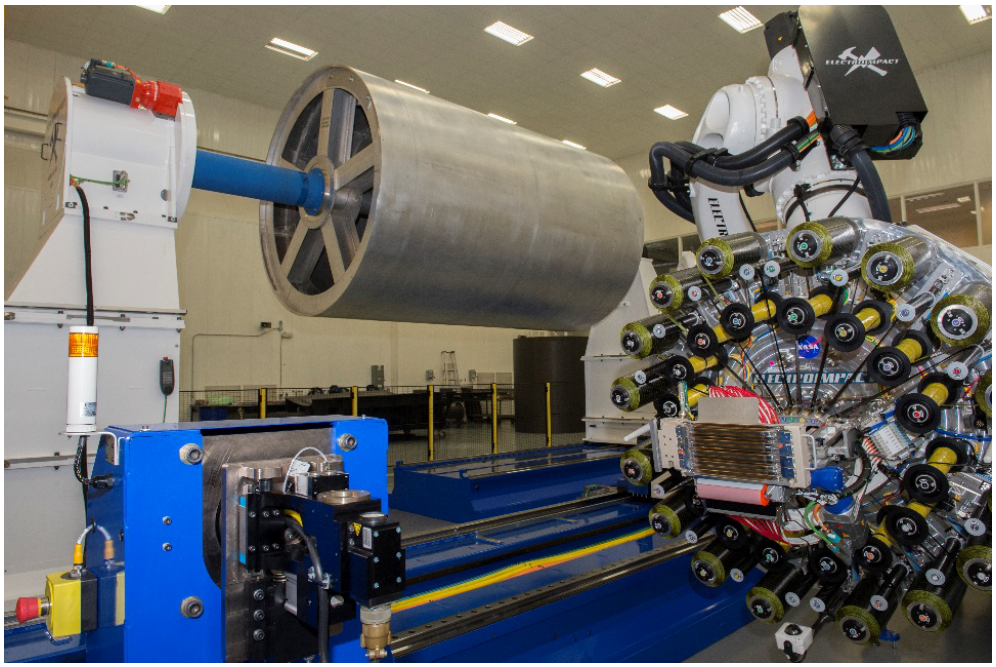

Figure 1. Fabrication tool and AFP effector.

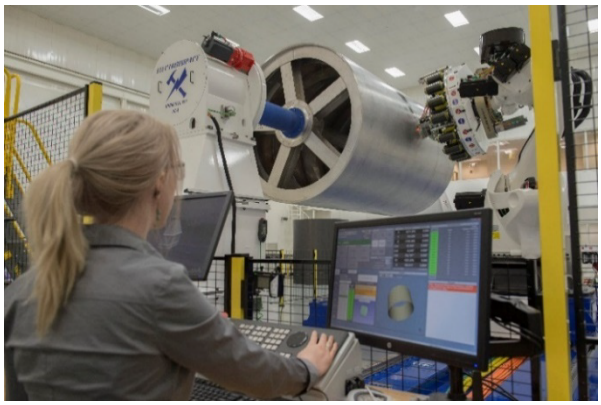

a) IML layup using AFP.

b) Manual adhesive film and honeycomb core application.

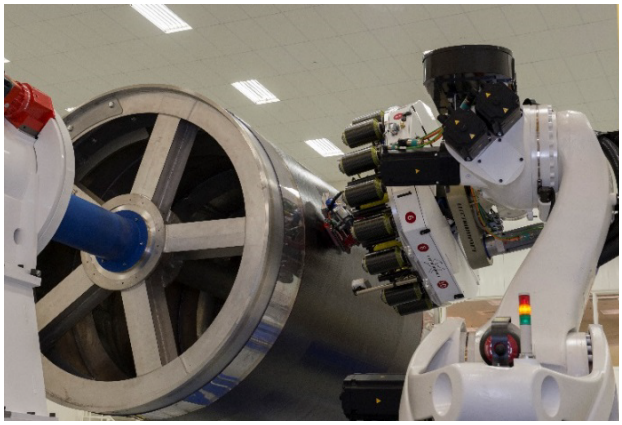

c) OML layup using AFP

d) Autoclave cure

e) Tool removal.

f) Trimming and machining holes in the areas of the load introduction fixtures.

Figure 2. CTA8.2 fabrication.

2.2.3 Nondestructive Evaluation and Structured-Light Geometry Measurement

Visual inspections of the test article were conducted at every stage of the test article processing, i.e., beginning after the autoclave cure until the test article was installed in the test rig. Thermography and vacuum shearography were performed after the test article was trimmed but before it was installed in the metallic attachment rings. There were no identified meaningful

manufacturing imperfections or handling damage that could impact structural performance of the test article.

The OML and IML surfaces were structured-light scanned to determine the manufactured geometry of the test article, including geometric imperfections. The radial imperfections (midsurface and thickness) were later used in the development of the as-manufactured finite element models (FEMs). The midsurface radial position of the test article, and thus midsurface radial imperfections, obtained by averaging the OML and IML position measurements, is shown in Figure 3. The shell thickness, obtained as a difference between the OML and IML position measurements, is shown in Figure 4. When interpreting Figure 3 and 4, it is important to remember that both results account for the presence of the padup plies (at the axial coordinates below –30 in. and above 30 in.) and some of the attachment ring sections that the sandwich cylinder is potted within (below –45.375 in. and above 45.375 in.). The midsurface imperfections, which can most easily be seen by the variation in the acreage region of Figure 3, show a radial oscillatory pattern of a global extent, i.e., varying radii around the circumference of the cylinder extending FWD to AFT. A more localized behavior can also be identified around the circumference at the axial coordinate at approximately 18 in. This imperfection originated from a weld line on the aluminum tool. The thickness imperfections that can be seen in Figure 4 are less organized relative to the radial imperfections. However, some correlation to the core splicing pattern of the core sheet can be identified. As an example, a thicker section of the cylinder is seen in Figure 4 just above the AFT padup in between radial stations 168° and 240°. By referencing this area to the core splicing pattern in Figure A1 of Appendix A, it is observed that core sheet designated as AFT 1 is, to a large extent, coinciding with the increased thickness measurement and may result from core sheet AFT 1 having been slightly thicker than the surrounding core sheets. Further details of how the structured-light data were processed, as well as an overview of the scripting technique developed under the SBKF project to implement geometric midsurface position and shell thickness data of the physical test article, are provided in Reference 5. The previously mentioned weld line near the +18-in. axial location was shown to be present in both the IML and OML surface structured-light scans, but a refinishing of the mandrel surface removed this unintentional feature for the remaining test articles CTA8.2B and CTA8.3. Additional details of the CTA8.2 IML and OML surfaces are also provided in Reference 5.

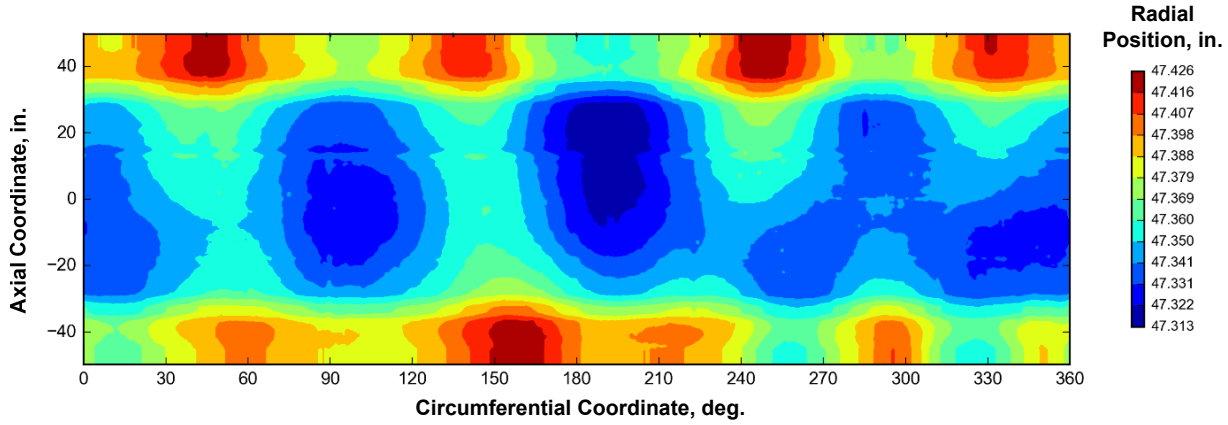

Figure 3. Unrolled image of the as-manufactured midsurface radial position.

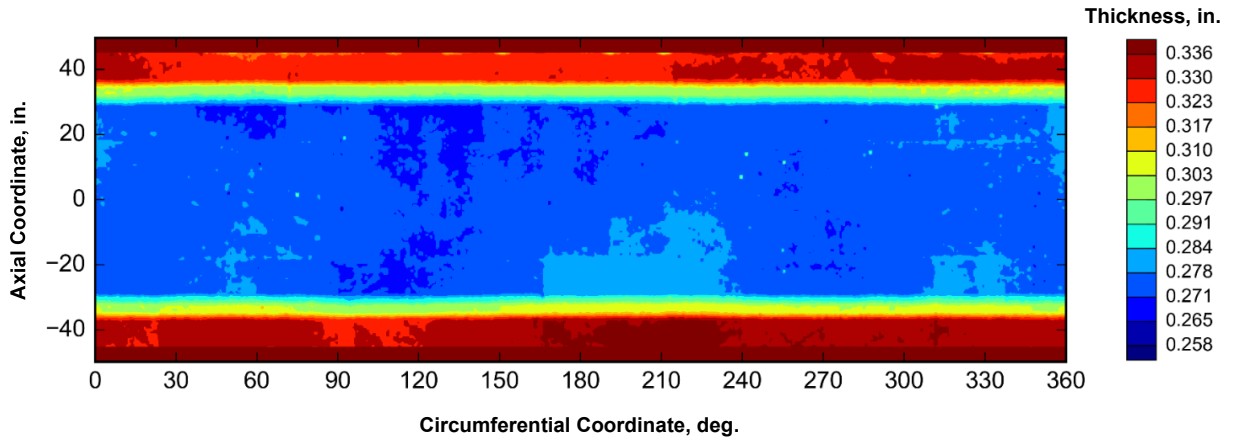

Figure 4. Unrolled image of the as-manufactured thickness.

2.3 Test Facility

The testing was conducted in the MSFC LTAE in building 4619 under the direction of the ET30 Structural Strength Test Group. The test assembly, shown in Figure 5, was designed, analytically verified, and fabricated to meet program test objectives. The MSFC design drawing numbers for each of the components that comprise the test assembly are also indicated in Figure 5. The test assembly was a self-reacting load system composed of an upper and lower load spider, 16 load struts (eight at the top and eight at the bottom), upper and lower transition sections, the test-article assembly, and eight load lines. Each load line consisted of a hydraulic cylinder, 4-in-diameter loading rod (pipe), a load cell, and attachment hardware. The load lines could be controlled independently in load control or stroke (displacement) control to apply uniform compression or combined compression and bending, with a maximum combined load capability of 1.5 million pounds of axial compression force and 80,000 pounds of axial tension force. Application of the bending component of the load was achieved by varying the axial loads between the eight individually controlled load lines. For the testing described herein, the load lines were able to accommodate a stroke of ±2.0 in. during testing. The test-assembly dead weight was removed from the test article prior to beginning each load sequence; the applied load that removed this dead weight is termed the tare load.

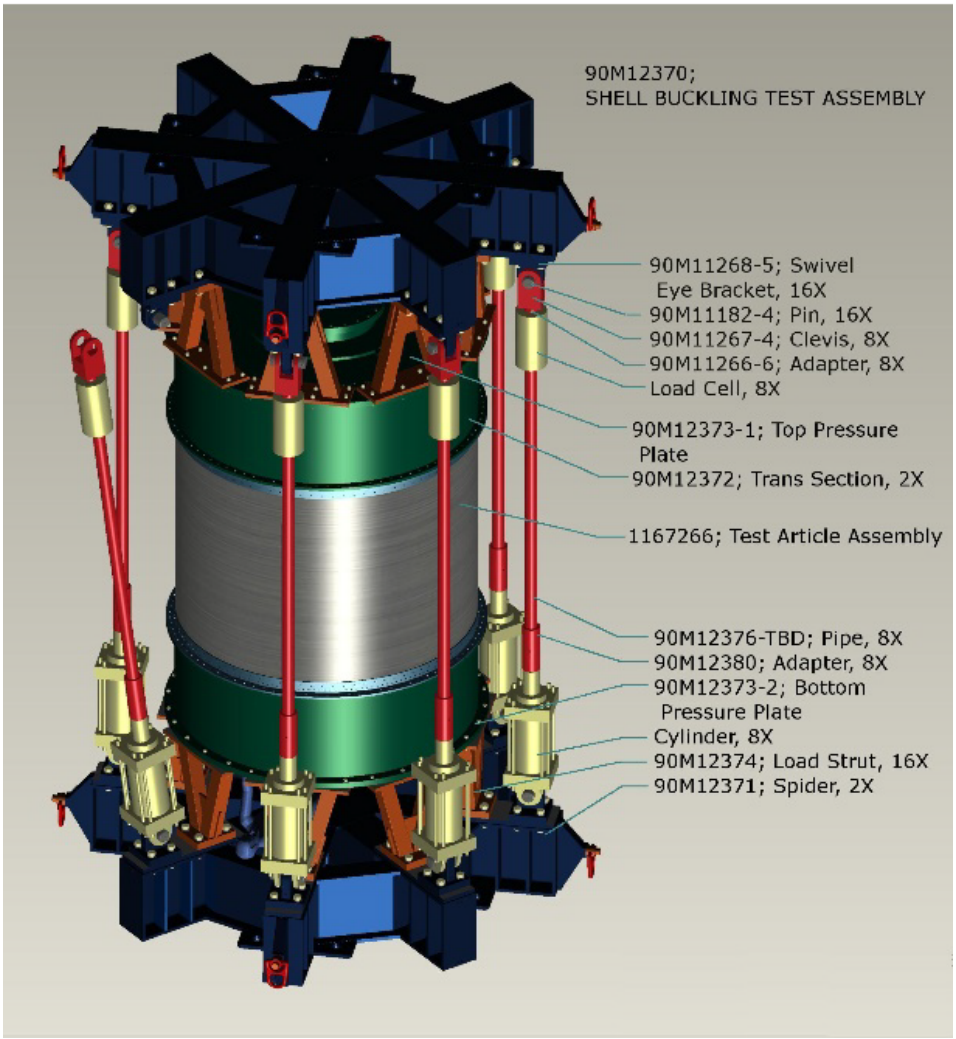

Figure 5. Test Assembly at MSFC.

2.4 Test Article Installation and Alignment

During assembly, the test article was oriented to a known, precise circumferential orientation for testing, as shown in Figure 6. Having a known orientation was important for these tests so that the structural response, including strains and displacements, could be fully compared to the predictions. Knowing the orientation is particularly important during tests that apply a bending moment because the maximum compression load introduced into the test article needed to occur in a specific known location on the cylinder. It was also required that the FWD and AFT loading fixtures be aligned with each other so that the load lines were vertical and oriented parallel with the test article longitudinal axis. Proper alignment of the load lines was intended to ensure that undesirable torsion or bending loads would be negligible during testing. The metallic attachment rings were indexed with respect to the test article circumferential reference location to ensure proper alignment in the built-up test assembly, as specified in the assembly drawing, Figure A4 of Appendix A, and in Reference 2. The attachment ring alignment, specifically relative circumferential index angle, parallelism, and perpendicularity, were verified and documented per the assembly procedure, also within Reference 2.

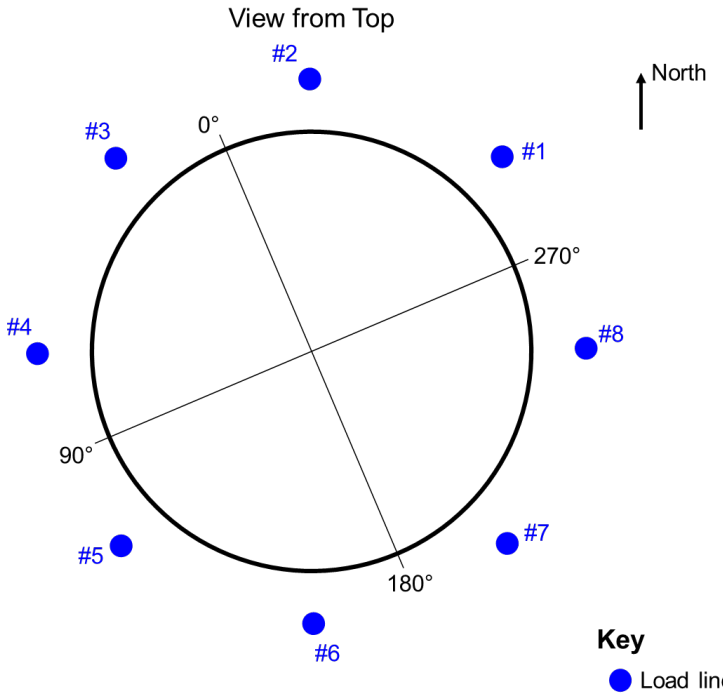

Figure 6. Test article orientation relative to the load-line layout and numbering convention, top view.

The test article interfaced with the test assembly through the set of attachment rings. The attachment rings were one piece, 6061-T6 aluminum rings with an inner and outer attachment flange that interfaced with the transition section (part 90M12372 in Figure 5), and contained a 0.8-in-wide machined groove in which the test article was seated (Figure A3 of Appendix A). The attachment rings weighed approximately 358 pounds each. The test article was placed in the grooves, potted, and mechanically fastened in place according to the assembly procedure described in Figure A4 of Appendix A. Micor Micorox® Standard Grout [6] potting material was used. The potting material was not considered the primary axial loading transfer mechanism between the attachment rings and the test article as a release agent, Loctite® Frekote 700-NC™ was applied in the process of installing CTA8.2 in the attachment rings. The release agent was applied to avoid developing an adhesive bond and instead to rely on the test-article ends being in bearing contact at the "bottom" of the attachment ring grooves. The potting material, however, was considered a part of the primary mechanism against the out-of-plane rotation of the CTA8.2 cylinder wall at the boundary. Furthermore, mechanical fasteners (bolts through both attachment ring flanges, the potting material, and the test articles) were used for handling and as a failsafe feature.

2.5 Test Article Instrumentation

Several types of instrumentation as well as photographic and video systems were utilized during this test and included: conventional (electrical-resistance) strain gauges, displacement transducers, load cells, a fiber-optic (strain) sensing system (FOSS), and low-speed and HS-DIC systems. All measured data obtained during the test were synchronized with respect to time, load signal from load line #1, and a triangle wave signal to enable posttest data synchronization.

2.5.1 Displacement Measurements

Axial, radial, and tangential displacement measurements of the test article, test-article attachment rings, and actuators were obtained during the test.

Actuator displacements were measured using displacement transducers attached to the hydraulic cylinders and were used as position control sensors for the test control system. Additionally, the axial displacement of the AFT and FWD attachment rings were used to calculate the end-shortening of the test article (i.e., the relative axial motion of the FWD attachment ring with respect to the AFT attachment ring). As such, the axial displacement of both attachment rings was measured at four locations spaced 90° around the circumference. The measurement locations are shown in Table 2 and Figure 7, 8, and 9. Additionally, the axial displacement of the AFT attachment ring was measured at one location on the OML attachment ring flange, also shown in Table 2 and Figure 7, 8, and 9. This additional OML measurement was used to calculate rotation (about the tangent) of the AFT attachment ring.

The axial end-shortening of the test article was calculated at the four axial-measurement locations around the circumference (0°, 90°, 180°, and 270°) as follows:

$$0°: \ \delta_{D000A} = \delta_{D113A} - \delta_{D317A} \tag{1a}$$

$$90°: \ \delta_{D090A} = \delta_{D114A} - \delta_{D318A} \tag{1b}$$

$$180°: \ \delta_{D180A} = \delta_{D115A} - \delta_{D319A} \tag{1c}$$

$$270°: \ \delta_{D270A} = \delta_{D116A} - \delta_{D320A} \tag{1d}$$

where δ_{D113A}, δ_{D114A}, δ_{D115A}, δ_{D116A} and δ_{D317A}, δ_{D318A}, δ_{D319A}, δ_{D320A} correspond to electronic displacement indicator (EDI) measurements on the AFT and FWD attachment rings, respectively, and δ_{D000A}, δ_{D090A}, δ_{D180A}, δ_{D270A} correspond to the derived end-shortening displacements at the 0°, 90°, 180°, and 270° locations, respectively. These end-shortening displacement equations presume that the measured AFT and FWD displacements are negative downward. The measurement locations are shown in Table 2 and Figure 7, 8, and 9.

The axial displacement of the AFT and FWD padup areas was used to calculate the shortening of the test article over its section that excludes the potted ends. This axial displacement was measured at four equally spaced locations around the circumference at 45°, 135°, 225°, and 315°. The measurement locations are shown in Table 2 and Figure 7 and 8. The axial end-shortening of this section of test article was calculated at the four axial-measurement locations around the circumference (45°, 135°, 225°, and 315°) as follows:

$$45°: \ \delta_{D045A} = \delta_{D530A} - \delta_{D529A} \tag{2a}$$

$$135°: \ \delta_{D135A} = \delta_{D532A} - \delta_{D531A} \tag{2b}$$

$$225°: \ \delta_{D225A} = \delta_{D534A} - \delta_{D533A} \tag{2c}$$

$$315°: \ \delta_{D315A} = \delta_{D536A} - \delta_{D535A} \tag{2d}$$

where δ_{D530A}, δ_{D532A}, δ_{D534A}, δ_{D536A} and δ_{D529A}, δ_{D531A}, δ_{D533A}, δ_{D535A} correspond to EDI measurements on the AFT and FWD padups, respectively, and δ_{D045A}, δ_{D135A}, δ_{D225A}, δ_{D315A} correspond to the derived shortening displacements at the 45°, 135°, 225°, and 315° padup locations, respectively. These shortening displacement equations assume that the measured AFT and FWD displacements are negative downward.

The radial displacement in the proximity of the predicted global buckling event origination was measured using four additional EDIs installed on the IML side of the cylinder. These EDIs designated D425R through D428R were installed as shown in Table 2 and Figure 7 and 8.

The out-of-plane deflections of the test article and attachment rings were measured at 13 locations. Specifically, displacements were measured at the midlength (see note in Table 2 for additional midlength location information) of the test article and on both attachment rings at four circumferential locations spaced 90° as shown in Table 2 and Figure 7, 8, and 9.

The relative rotational movement of the AFT and FWD attachment rings was monitored by measuring the tangential motion of both attachment rings at one circumferential location as shown in Table 2 and Figure 7, 8, and 10. These tangential displacement measurements were used to characterize the rotation of the attachment rings about the cylinder axis (tangent to the edge of the attachment ring).

Table 2. Description of EDIs.

EDI ID	Measurement range	Measurement description	Sign convention
D101R^{+}, D102R*, D103R^{+}, D104R^{+}, D309R^{+}, D310R*, D311R^{+}, D312R^{+}	±1.0 in.	Radial displacement on the AFT and FWD attachment rings to characterize local or rigid-body displacements	Outward radial displacement: +
D205R$^{+\#}$, D206R*$^{\#}$, D207R$^{+\#}$, D208R$^{+\#}$	±2.0 in.	Radial displacement at the midlength of the test article*	Outward radial displacement: +
D113A, D114A, D115A, D116A	±1.0 in.	Axial displacement of the AFT attachment ring on the IML flange (for test-article end-shortening and ring-rotation calculations)	Upward axial displacement: +
D317A, D318A, D319A, D320A	±2.0 in.	Axial displacement of the FWD attachment ring on the IML flange (for test-article end-shortening calculation)	Upward axial displacement: +
D121T, D322T	±1.0 in.	Tangential displacement at a point on the AFT and FWD attachment rings to characterize relative torsional displacements	Displacement in positive theta: +
D123S*	±1.0 in.	Radial displacement on the AFT and attachment ring to characterize ring clevis rotation or deformation	Outward radial displacement: +
D124O	±1.0 in.	Axial displacement of the AFT attachment ring on the OML flange (for test-article end-shortening and ring-rotation calculations)	Upward axial displacement: +
D425R, D426R, D427R, D428R	±1.0 in.	Radial displacement at selected locations associated with the global buckling onset	Outward radial displacement: +
D530A, D532A, D534A, D536A	±1.0 in.	Axial displacement in the AFT IML padup area (for test-article end-shortening excluding attachment ring potting effects)	Upward axial displacement: +
D529A, D531A, D533A, D535A	±1.0 in.	Axial displacement in the FWD IML padup area (for test-article end-shortening excluding attachment ring potting effects)	Upward axial displacement: +

*All radial EDIs on the 90° line are 0.5 in. right from IML (in negative circumferential direction).

$^{\#}$All EDIs on the midlength are 0.5 in. above (in positive axial direction).

$^{+}$All other radial EDIs on the 0°, 180°, and 270° lines are 0.5 in. left from IML (in positive circumferential direction).

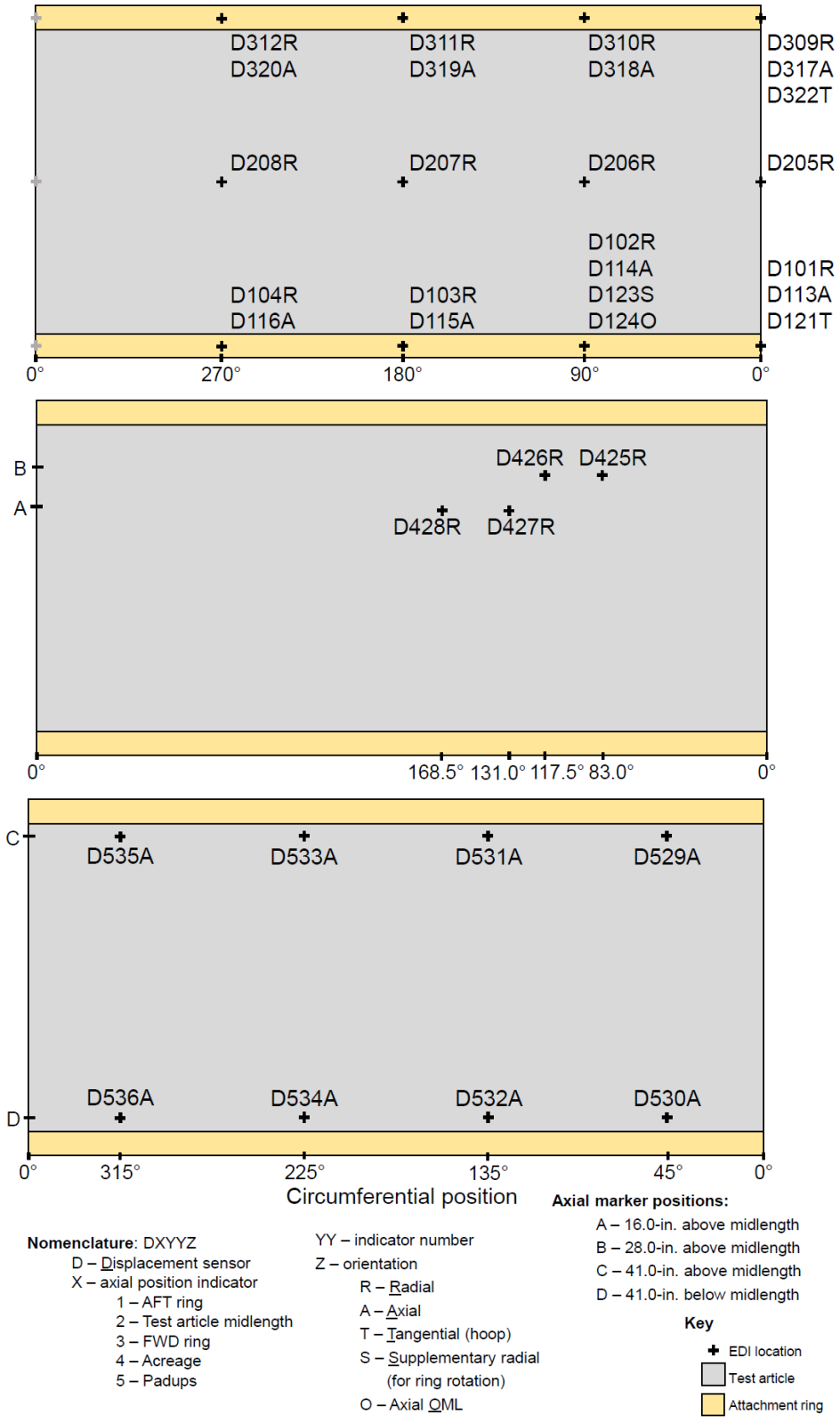

Figure 7. Locations of EDI measurements, unrolled view from IML.

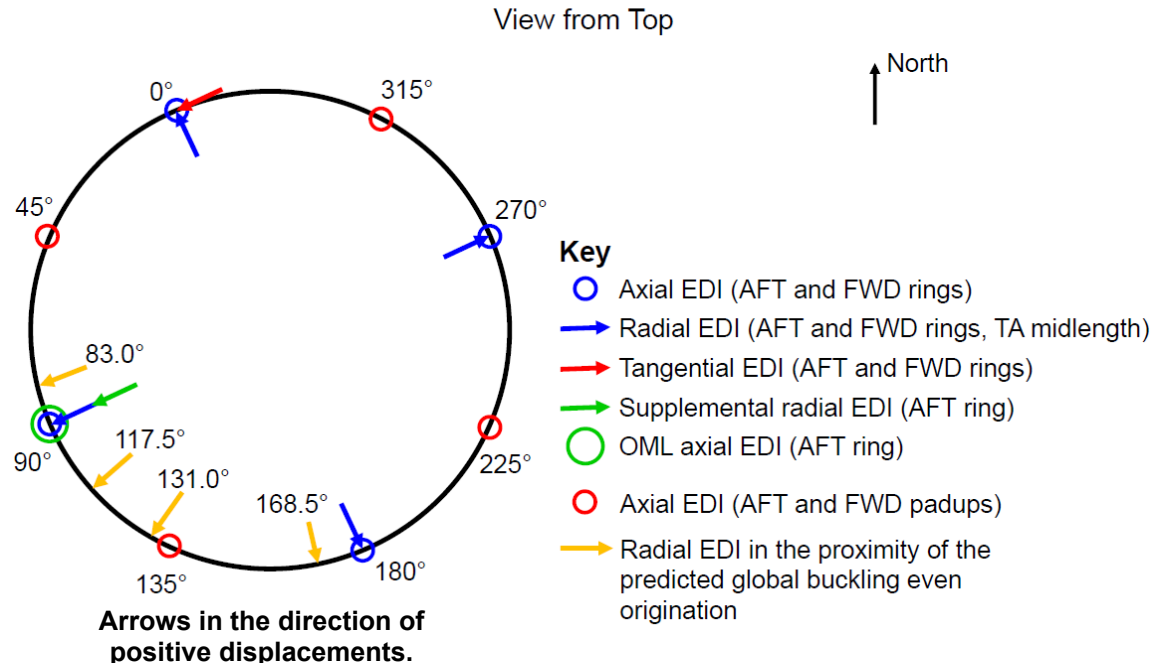

Figure 8. EDI locations as seen from the top of the test article.

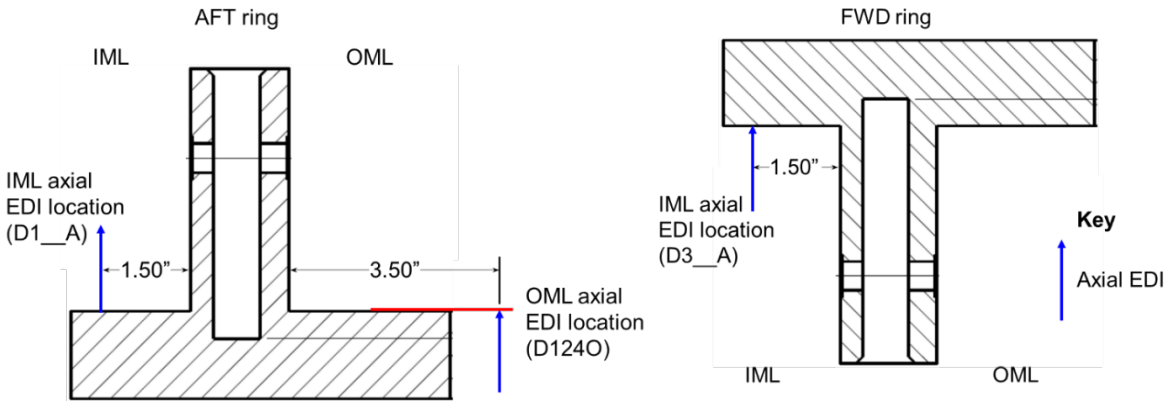

a) Axial EDI locations

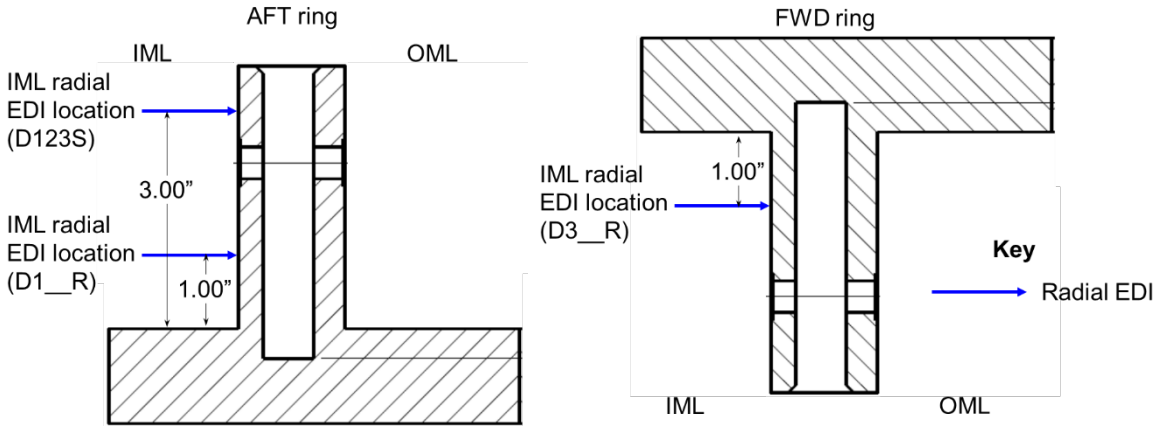

b) Radial EDI locations

Figure 9. Cross-sectional view of the EDI locations on the attachment rings. Arrows in the direction of positive displacements.

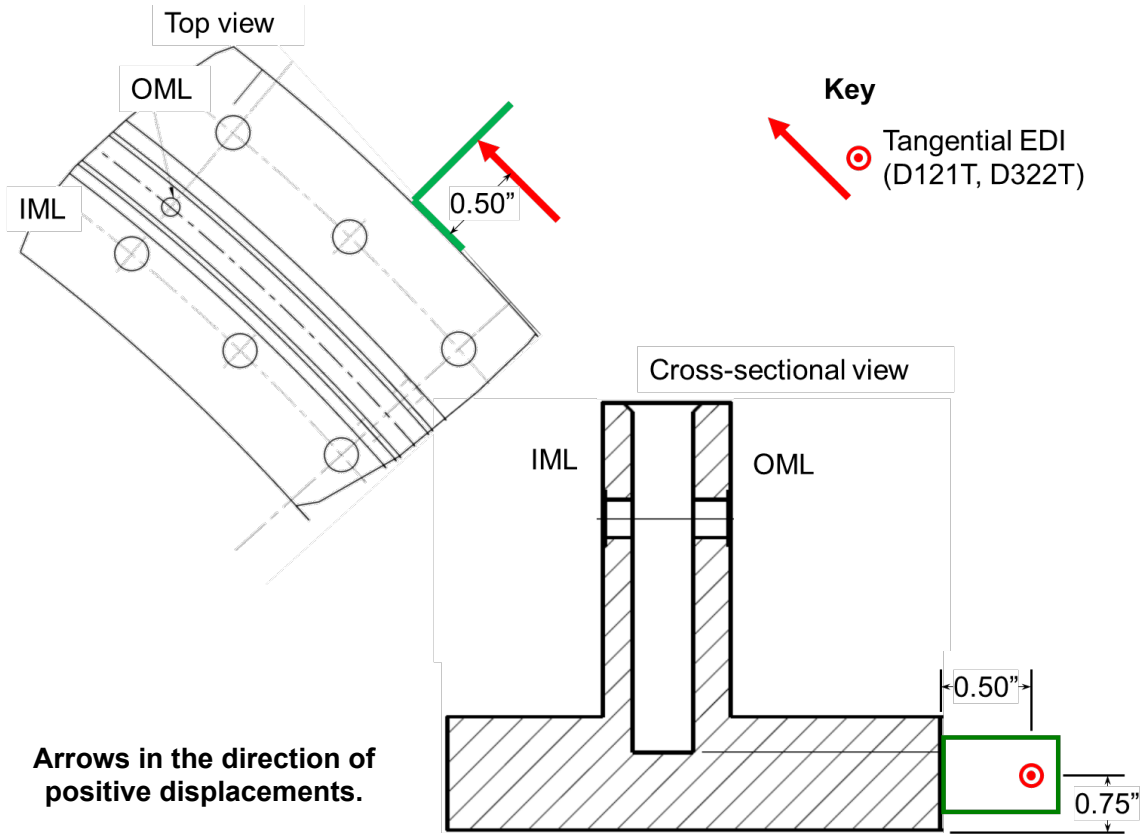

Figure 10. Tangential EDI location on the attachment rings.

2.5.2 Conventional Strain Measurements

Strain measurements on the test article were required to assess uniformity of the load introduction into the shell during loading, and to monitor the local strain response of the test article during the prebuckling and postbuckling phases of testing. Two types of Micro-Measurements strain gages were used: CEA-06-187UW-350 (uniaxial) and CEA-06-125UT-350 (biaxial). The gage patterns and labeling convention are specified in Figure A5 of Appendix A. Each gage was installed per manufacturer’s recommendations for graphite-epoxy composite application surface and the MSFC Test Team standard installation procedures.

2.5.3 Fiber-Optics Strain Measurements

FOSSs were placed according to the diagram in Figure A6 of Appendix A to provide additional strain measurements. The FOSS pattern was setup such that there would be near-continuous circumferential measurements 2 in. away from the AFT attachment ring and 2 in. away from the FWD attachment ring.

2.5.4 Three-Dimensional Digital Image Correlation (3D-DIC)

This photogrammetry technique is used to track pixel subsets through a series of images from the undeformed to the deformed state, and allows for surface shape, displacements, and strains to be calculated. This technique utilizes pairs of cameras, in a stereo configuration, to view and monitor a speckle pattern as it changes during loading and deformation. In order to do so, the outer surface of the entire test article had a high-contrasting speckle pattern of black speckles on a white background applied. Using such a high-contrasting speckle pattern, along with proper lighting,

camera system calibrations, and camera parameters (e.g., sensor resolution direction, focus, lens aperture settings and depth-of-field, and relative angles (stereo angles) per system) allows the maximum resolution displacement and strain data to be generated.

2.5.4.1 Low-speed Digital Image Correlation

The locations of the eight 3D low-speed DIC camera systems, which were equally spaced around the circumference of the OML (centered approximately 45° apart) with an overlapping field-of-view in order to fully capture and characterize the behavior of the test article, are shown in Figure 11. Each field-of-view was approximately 100-in. tall, which included the test article acreage and the attachment rings, and 70° wide (allowing for 15° overlap between adjacent systems). All of the DIC systems were synchronized, and the synchronization was verified and documented. The analog load signal from load line #1 and a triangle-wave synchronization signal were recorded for posttest correlation. The low-speed DIC systems recorded one image every 5 sec.

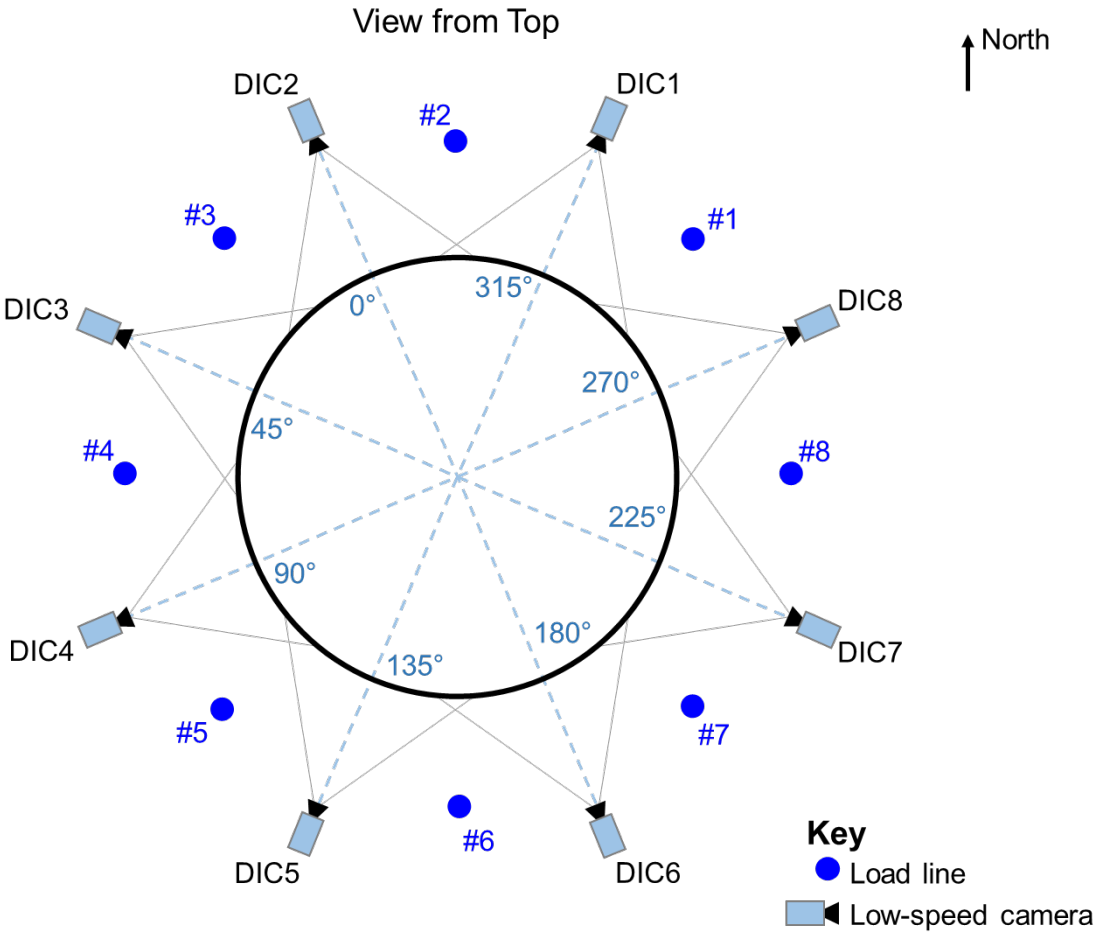

Figure 11. The low-speed DIC system.

2.5.4.2 High-speed Digital Image Correlation

A total of six HS camera pairs were set-up around the circumference of the OML, as shown in Figure 12, to continuously record at 10,000 frames per second (fps). Due to the number of camera pairs and the test stand (camera mounting locations), the camera systems were not equally spaced; however, they were still located in positions to allow for overlapping coverage between adjacent camera systems. The HS camera systems were installed to measure the displacement response of

the entire OML during all load sequences, but were primarily used during the failure load sequence to capture the dynamic failure event including damage initiation and propagation. Due to the high frame rate (10,000 fps) and the limited resolution of the cameras, the optimal speckle size was larger than that of the low-speed systems, 0.45 in. to 0.65 in. In order to properly correlate over the field-of-view and provide the best accuracy and data for all DIC systems, the speckle pattern of the low-speed system was adjusted to be closer to the lower end of the optimal size for the HS system. Consequently, a global speckle pattern of 0.35 in. to 0.5 in. was chosen for the entire acreage of the test article. The cameras were synchronized with respect to each other and had a common, manual, post-trigger recording function (i.e., all data from before the trigger are pressed and no data after the trigger). The cameras were programmed to acquire images at a rate of 10,000 fps in a continuous write-overwrite loop, with a total recording time of approximately 2.55 sec, to the buffer in each camera until the HS-DIC operator triggered the manual post-trigger recording after the buckling or failure event.

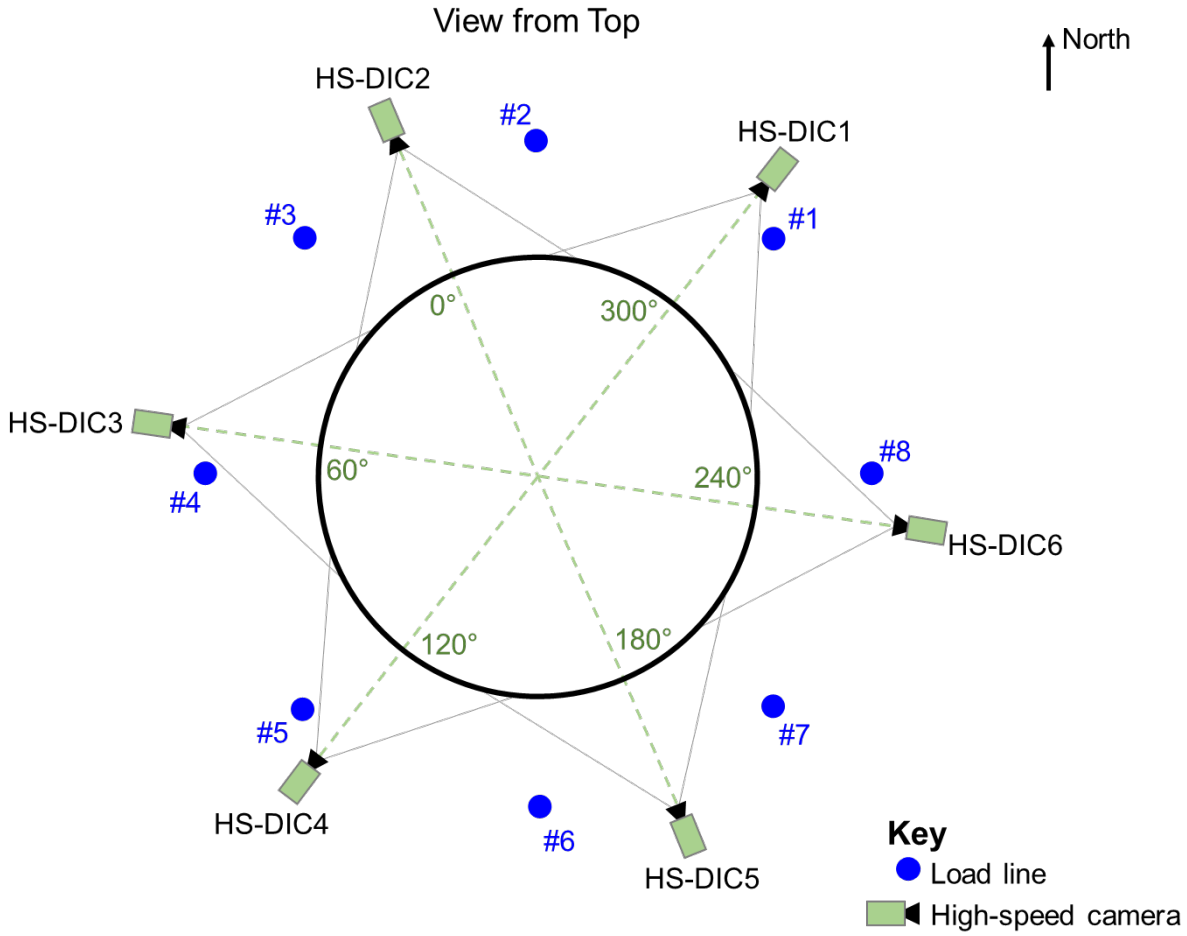

Figure 12. The HS-DIC system.

2.6 Test Load Sequence

A series of eight load sequences (LS1 – LS8) were planned before commencing the tests. Seven of those load sequences, LS1 – LS7, were considered subcritical in that the load levels applied to the test article were not expected to cause buckling or structural failure. The final planned load sequence, LS8, was to load the test article in uniform axial compression until buckling or another form of failure occurred. The predicted linear axial buckling load, P_{cr}, for the idealized,

geometrically perfect test article with the attachment rings and subjected to a uniform compression load was 913,920 lbf and was obtained using a Lanczos eigenanalysis. A transient geometrically nonlinear analysis of a FEM with the as-manufactured radial and thickness imperfections and the entire test apparatus predicted the axial buckling load, P_{cr}^{NL}, at 864,159 lbf. For the purposes of the test, the critical bending moment, M_{cr}, was defined as the bending moment that would produce a maximum compressive line load that is equivalent to the uniform line load at P_{cr} for uniform axial compression. As such, M_{cr} was calculated to be 21.93×10^6 in-lbf. Each load sequence was defined in terms of the sum of a percentage of the critical axial compression load, P_{cr}, and a percentage of the critical bending moment, M_{cr}. The eight load sequences are described in the following sections.

During the testing, after load sequences LS1 – LS7 were executed and before the final load to failure, LS8, was attempted, one additional load sequence, designated as LS9, up to a uniform compressive load of 0.5 P_{cr}, was added and executed in addition to the originally planned load sequences. The motivation for including LS9 was to even out potential nonuniform settling of the test article in the metallic attachment rings due to the series of LS4 – LS7, which all included a bending component. The summary of the test load sequences is presented in Table 3, and more detailed descriptions follow in the subsequent subsections 2.6.x. Each load sequence is started by ramping to the tare load (i.e., the actuator loads that remove the weight of the upper loading structure from the test article), the instrumentation is re-zeroed at the tare load, and then the loads in Table 3 are applied from tare. Positive load values in Table 3 through Table 12 correspond to a tension load in the load line and result in a compression load in the test article. A pause occurred at the end of each load step indicated in Table 3 through Table 11 to assess the behavior of the test article and test system. The maximum allowed variation between measured and commanded loads during the load sequences was specified as ±5.0% of the maximum actuator load, as defined in Table 3, or ±1000 lbf, whichever was greater. The loading rate did not exceed 10,000 lbf/min. During controlled unloading, the unloading rate did not exceed 20,000 lbf/min.

Table 3. Maximum actuator loads for each test condition (lbf).

Actuator number (Figure 6)	LS1 Axial	LS2 Axial	LS3 Axial	LS4 Axial + Bend (0°)*	LS5 Axial + Bend (90°)*	LS6 Axial + Bend (180°)*	LS7 Axial + Bend (270°)*	LS 9 Axial	LS 8 Axial†
1	22,848	45,696	68,543	29,207	7496	16,489	38,199	57,120	137,087
2	22,848	45,696	68,543	38,199	16,489	7496	29,207	57,120	137,087
3	22,848	45,696	68,543	38,199	29,207	7496	16,489	57,120	137,087
4	22,848	45,696	68,543	29,207	38,199	16,489	7496	57,120	137,087
5	22,848	45,696	68,543	16,489	38,199	29,207	7496	57,120	137,087
6	22,848	45,696	68,543	7496	29,207	38,199	16,489	57,120	137,087
7	22,848	45,696	68,543	7496	16,489	38,199	29,207	57,120	137,087
8	22,848	45,696	68,543	16,489	7496	29,207	38,199	57,120	137,087
Total load	182,784	365,568	548,344	182,782	182,782	182,782	182,782	456,960	1,096,696

*Circumferential location of maximum line load

†Greatest expected maximums calculated as 1.2x the predicted buckling load for geometrically perfect test article

2.6.1 LS1: 0.2 P_{cr}

A uniform axial compression load was applied to the test article up to a maximum of 182,784 lbf total applied load according to the load steps specified in Table 4, and then was unloaded to the tare load. The purpose of this test was to exercise the test apparatus, remove slack from the system, check for uniformity of load application, and check the functionality of all control and measurements systems involved in the test. Actuator loads for LS1 are summarized in Table 4.

Table 4. Actuator loads (lbf) for LS1.

Load Step	Actuator #1	Actuator #2	Actuator #3	Actuator #4	Actuator #5	Actuator #6	Actuator #7	Actuator #8	Total Load
#1	4570	4570	4570	4570	4570	4570	4570	4570	36,560
#2	9139	9139	9139	9139	9139	9139	9139	9139	73,112
#3	13,709	13,709	13,709	13,709	13,709	13,709	13,709	13,709	109,672
#4	18,278	18,278	18,278	18,278	18,278	18,278	18,278	18,278	146,224
#5	22,848	22,848	22,848	22,848	22,848	22,848	22,848	22,848	182,784

2.6.2 LS2: 0.4 P_{cr}

A uniform axial compression load was applied to the test article in LS2. The load was increased to a maximum of 365,568 lbf compression over the load steps specified in Table 5, and then gradually unloaded to the tare load. The purpose of this load sequence was to exercise the test system, verify that the applied loads matched closely the desired input loads, and ensure measured displacements and strains were in reasonable agreement with predicted values. Actuator loads for LS2 are summarized in Table 5.

Table 5. Actuator loads (lbf) for LS2.

Load Step	Actuator #1	Actuator #2	Actuator #3	Actuator #4	Actuator #5	Actuator #6	Actuator #7	Actuator #8	Total Load
#1	9139	9139	9139	9139	9139	9139	9139	9139	73,112
#2	18,278	18,278	18,278	18,278	18,278	18,278	18,278	18,278	146,224
#3	27,417	27,417	27,417	27,417	27,417	27,417	27,417	27,417	219,336
#4	36,557	36,557	36,557	36,557	36,557	36,557	36,557	36,557	292,456
#5	45,696	45,696	45,696	45,696	45,696	45,696	45,696	45,696	365,568

2.6.3 LS3: 0.6 P_{cr}

A uniform axial compression load was applied to the test article in LS3. The load was increased to a maximum of 548,344 lbf compression over the load steps specified in Table 6, and then gradually unloaded to the tare load. The purpose of this test was again to exercise the test system, verify that the applied loads matched closely the desired input loads, and ensure measured displacements and strains were in reasonable agreement with predicted values. Actuator loads for LS3 are summarized in Table 6.

Table 6. Actuator loads (lbf) for LS3.

Load Step	Actuator #1	Actuator #2	Actuator #3	Actuator #4	Actuator #5	Actuator #6	Actuator #7	Actuator #8	Total Load
#1	11,424	11,424	11,424	11,424	11,424	11,424	11,424	11,424	91,392
#2	22,848	22,848	22,848	22,848	22,848	22,848	22,848	22,848	182,784
#3	34,272	34,272	34,272	34,272	34,272	34,272	34,272	34,272	274,176
#4	45,696	45,696	45,696	45,696	45,696	45,696	45,696	45,696	365,568
#5	57,119	57,119	57,119	57,119	57,119	57,119	57,119	57,119	456,952
#6	68,543	68,543	68,543	68,543	68,543	68,543	68,543	68,543	548,344

2.6.4 LS4: 0.2 P_{cr} + 0.2 M_{cr} (Maximum Compression at the 0° Circumferential Location)

A combined axial compression and bending load was applied to the test article in LS4. The load was increased to a total load of 182,782 lbf (total of all load line loads) with the maximum compression load occurring at the 0° circumferential location according to the load steps specified in Table 7, and then gradually unloaded to the tare load. The purpose of this test was to exercise the test system in the presence of combined axial compression and bending (bending in which maximum compression loads were applied to the test article between load lines 2 and 3), verify that the applied loads matched closely the desired input loads, and verify measured displacements and strains were in reasonable agreement with predicted values. Actuator loads for LS4 are summarized in Table 7.

Table 7. Actuator loads (lbf) for LS4.

Load Step	Actuator #1	Actuator #2	Actuator #3	Actuator #4	Actuator #5	Actuator #6	Actuator #7	Actuator #8	Total Load
#1	5841	7640	7640	5841	3298	1499	1499	3298	36,556
#2	11,683	15,280	15,280	11,683	6596	2,998	2998	6596	73,114
#3	17,524	22,919	22,919	17,524	9893	4498	4498	9893	109,668
#4	23,366	30,559	30,559	23,366	13,191	5997	5997	13,191	146,226
#5	29,207	38,199	38,199	29,207	16,489	7496	7496	16,489	182,782

2.6.5 LS5: 0.2 P_{cr} + 0.2 M_{cr} (Maximum Compression at the 90° Circumferential Location)

A combined axial and bending load was applied to the test article in LS5. The load was increased to a total load of 182,782 lbf (total of all load line loads) with the maximum compression load occurring at the 90° circumferential location based on the load steps specified in Table 8, and then the system was unloaded to the tare load. The purpose of this test was to exercise the test system in the presence of combined axial compression and bending (bending in which maximum compression loads were applied to the test article between load lines 4 and 5), verify that the applied loads matched closely the desired input loads, and check that measured displacements and strains were in reasonable agreement with predicted values. Actuator loads for LS5 are summarized in Table 8.

Table 8. Actuator loads (lbf) for LS5.

Load Step	Actuator #1	Actuator #2	Actuator #3	Actuator #4	Actuator #5	Actuator #6	Actuator #7	Actuator #8	Total Load
#1	1499	3298	5841	7640	7640	5841	3298	1499	36,556
#2	2998	6596	11,683	15,280	15,280	11,683	6596	2998	73,114
#3	4498	9893	17,524	22,919	22,919	17,524	9893	4498	109,668
#4	5997	13,191	23,366	30,559	30,559	23,366	13,191	5997	146,226
#5	7496	16,489	29,207	38,199	38,199	29,207	16,489	7496	182,782

2.6.6 LS6: 0.2 P_{cr} + 0.2 M_{cr} (Maximum Compression at the 180° Circumferential Location)

A combined axial and bending load was applied to the test article in LS6. The load was increased to a total load of 182,782 lbf (total of all load line loads) with the maximum compression load occurring at the 180° circumferential location, as shown in the load steps in Table 9, and then was unloaded to the tare load. The purpose of this test was to exercise the test system in the presence of combined axial compression and bending (bending in which maximum compression loads were applied to the test article between load lines 6 and 7), verify that the applied loads matched closely the desired input loads, and ensure measured displacements and strains were in reasonable agreement with predicted values. Actuator loads for LS6 are summarized in Table 9.

Table 9. Actuator loads (lbf) for LS6.

Load Step	Actuator #1	Actuator #2	Actuator #3	Actuator #4	Actuator #5	Actuator #6	Actuator #7	Actuator #8	Total Load
#1	3298	1499	1499	3298	5841	7640	7640	5841	36,556
#2	6596	2998	2998	6596	11,683	15,280	15,280	11,683	73,114
#3	9893	4498	4498	9893	17,524	22,919	22,919	17,524	109,668
#4	13,191	5997	5997	13,191	23,366	30,559	30,559	23,366	146,226
#5	16,489	7496	7496	16,489	29,207	38,199	38,199	29,207	182,782

2.6.7 LS7: 0.2 P_{cr} + 0.2 M_{cr} (Maximum Compression at the 270° Circumferential Location)

A combined axial and bending load was applied to the test article in LS7. The load was increased to a total load of 182,782 lbf (total of all load line loads) with maximum compression load occurring at the 270° circumferential location according to the load steps specified in Table 10, and then was unloaded to the tare load. The purpose of this test was to exercise the test system in the presence of combined axial compression and bending (bending in which maximum compression loads were applied to the test article between load lines 1 and 8), verify that the applied loads matched closely the desired input loads, and confirm measured displacements and strains were in reasonable agreement with predicted values. Actuator loads for LS7 are summarized in Table 10.

Table 10. Actuator loads (lbf) for LS7.

Load Step	Actuator #1	Actuator #2	Actuator #3	Actuator #4	Actuator #5	Actuator #6	Actuator #7	Actuator #8	Total Load
#1	7640	5841	3298	1499	1499	3298	5841	7640	36,556
#2	15,280	11,683	6596	2998	2998	6596	11,683	15,280	73,114
#3	22,919	17,524	9893	4498	4498	9893	17,524	22,919	109,668
#4	30,559	23,366	13,191	5997	5997	13,191	23,366	30,559	146,226
#5	38,199	29,207	16,489	7496	7496	16,489	29,207	38,199	182,782

2.6.8 LS9: 0.5 P_{cr}

A uniform axial compression load was applied to the test article in LS9. The load was increased to a maximum of 456,952 lbf compression based on the load steps specified in Table 11, and then the system was unloaded to the tare load. The purpose of this test was to remove any potential uneven settling of the test article in the metallic attachment rings after the series of non-uniform load sequences LS4 – LS7. Actuator loads for LS9 are summarized in Table 11.

Table 11. Actuator loads (lbf) for LS9.

Load Step	Actuator #1	Actuator #2	Actuator #3	Actuator #4	Actuator #5	Actuator #6	Actuator #7	Actuator #8	Total Load
#1	11,424	11,424	11,424	11,424	11,424	11,424	11,424	11,424	91,392
#2	22,848	22,848	22,848	22,848	22,848	22,848	22,848	22,848	182,784
#3	34,272	34,272	34,272	34,272	34,272	34,272	34,272	34,272	274,176
#4	45,696	45,696	45,696	45,696	45,696	45,696	45,696	45,696	365,568
#5	57,119	57,119	57,119	57,119	57,119	57,119	57,119	57,119	456,952

2.6.9 LS8: Test to Failure under Uniform Axial Compression

A uniform axial compression load was applied to the test article in LS8 until failure of the test article, resulting in a significant drop in load. The intended load steps are specified in Table 12 in black and grey fonts. The final failure is indicated in the red font, thus the intended load steps shown in the grey font were not reached. A pause occurred at the end of load steps #1 through #6 to assess the behavior of the test article and test system. The control system in LS8 was set up to load the test article in load control up to buckling or failure of the test article at a load rate of 30,000 lbf/min, based on the total load (or 3750 lbf/min in each load line). The pretest predictions indicated that for the sandwich wall construction of CTA8.2 the global buckling event will be almost instantenously followed by the material failure (rupture). When the test article exhibited a significant load drop, i.e., a drop exceeding a 5000-lbf reduction in the load applied in any load line, the LCS initiated a system HOLD by maintaining the last EDI-measured positions of actuators. At this time, the data acquisition system (DAS) operator triggered the HS DAS and sent a signal to start the HS FOSS, the HS-DIC operator triggered the HS camera recording, and the DIC operator captured the DIC image number associated with the load drop event. Once test article failure (rupture) was confirmed using video images, it was determined that there was no need to proceed with loading the test article into the post-ruptured range of loading, and all the actuators were unloaded at a slow rate.

The actuator loads for LS8 are summarized in Table 12. Load levels identified in Table 12 as 70% and 100% of the predicted critical load (see footnotes 1 and 2) correspond to the minimum and maximum expected failure load during the test, respectively.

Table 12. Actuator loads (lbf) for LS8.

Load Step	Percent P_{cr}	Actuator #1	Actuator #2	Actuator #3	Actuator #4	Actuator #5	Actuator #6	Actuator #7	Actuator #8	Total Load
#1	20%	22,848	22,848	22,848	22,848	22,848	22,848	22,848	22,848	182,784
#2	30%	34,272	34,272	34,272	34,272	34,272	34,272	34,272	34,272	274,176
#3	40%	45,696	45,696	45,696	45,696	45,696	45,696	45,696	45,696	365,568
#4	50%	57,119	57,119	57,119	57,119	57,119	57,119	57,119	57,119	456,952
#5	60%	68,543	68,543	68,543	68,543	68,543	68,543	68,543	68,543	548,344
#6	70%[1]	79,967	79,967	79,967	79,967	79,967	79,967	79,967	79,967	639,736
	77.5%	88,491	88,530	88,566	88,502	88,457	88,454	88,504	88,591	708,095
#7	80%	91,391	91,391	91,391	91,391	91,391	91,391	91,391	91,391	731,128
#8	90%	102,815	102,815	102,815	102,815	102,815	102,815	102,815	102,815	822,520
#9	100%[2]	114,239	114,239	114,239	114,239	114,239	114,239	114,239	114,239	913,912
#10	110%	125,663	125,663	125,663	125,663	125,663	125,663	125,663	125,663	1,005,304
#11	120%	137,087	137,087	137,087	137,087	137,087	137,087	137,087	137,087	1,096,696
	Facility max load	187,500	187,500	187,500	187,500	187,500	187,500	187,500	187,500	1,500,000

[1] Indicated before test as the minimum expected buckling load
[2] Indicated before test as the maximum expected buckling load

During LS8, the test article failed at a load of 708.1 kips, i.e., between load steps 6 and 7, at 77.5% P_{cr}. At the failure load, a perfectly uniform loading distribution would correspond to 88,512 lbf per actuator. As measured, the actuator forces varied between 88,454 lbf and 88,591 lbf, i.e., –58 lbf and +79 lbf (–0.07% and +0.09%) from the mean. Therefore, the uniformity of the load at failure was deemed very good and was not a factor that would initiate a premature failure. In addition, the load versus averaged end-shortening data was examined from all uniform compression load sequences, namely LS1 – LS3, LS9 (after the series of the combined compression and bending load cases LS4 through LS7), and LS8. These checks were exercised based on the EDI measurements of the movement of the attachment rings, Figure 13(a), and the EDI measurements between the FWD and AFT padups, Figure 13(b), as described in Section 2.5.1. In other words, end-shortening in Figure 13(a) is based on averaging results from Eqs. (1a) through (1d), and end-shortening in Figure 13(b) is based on averaging results from Eqs. (2a) through (2d).

A more nonlinear response is observed in Figure 13(b) when compared to Figure 13(a). The results shown in Figure 13(b) are measured between the so called “diving boards” (similar to those shown in green in Figure 10) attached in the FWD and AFT padup areas of the test article. Consequently, under loading, these areas deformed more in the radial directions than the aluminum attachment rings did; i.e., where the measurements represented in Figure 13(a) were obtained. Radial deformation of the cylinder wall effectively produced OML surface rotation and the “diving boards” were subjected not only to vertical displacements of their attachment points, but also to the vertical displacement component resulting from “diving board” rotations. Since rotations were larger in the padup areas than in the attachment ring sections, the rotation-induced vertical displacement component was larger in the padup areas and manifested itself as an amplified nonlinear axial displacement response seen in Figure 13(b).

The perfect overlapping of the curves in Figure 13 indicates that no appreciable change in the test article stiffness characteristics occurred between the individual load sequences. Furthermore, the repeatability of end-shortening with and without the attachment rings indicates that no appreciable

slippage or other detrimental interaction between the attachment rings and the sandwich composite cylinder occurred before the failure.

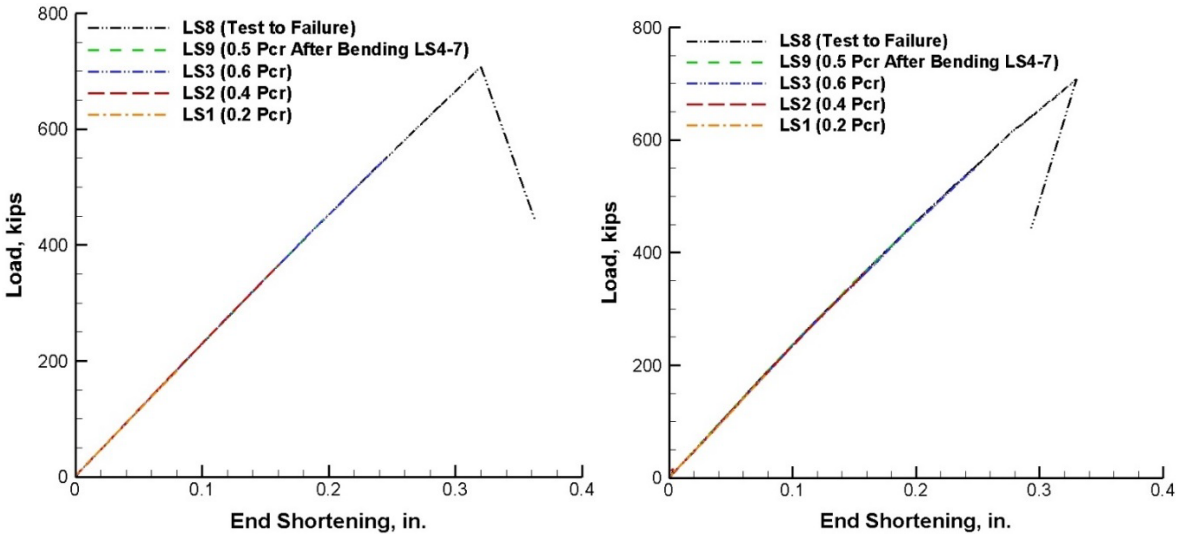

a) Measured between the attachment rings. b) Measured between the test article padups

Figure 13. Averaged end-shortening of test article as function of applied load.

The failure, circled in Figure 14, occurred in the proximity of the FWD attachment ring. The test article was removed from the test stand and the attachment rings. As a part of the failure investigation, sections of the FWD end of the test article were cut out. Visual inspection of these sections in the proximity of the failure location revealed significant core damage consistent with both transverse shearing and through-the-thickness compression/crushing. A cross-section of the failed test article in the proximity of the FWD attachment ring termination is shown in Figure 15. Subsequently, re-examination of the thickness of the sandwich structure in the direct proximity of the attachemnt rings was also performed based on the calculated thickness measurements from the structured-light scan data. A portion of the thickness data in the proximity of the FWD attachment ring is shown in Figure 16(a). Large sandwich thickness variations of approximately 0.08 in. were identified to be circumferentially aligned with the fitting bolts that connect the attachment rings and the cylinder. The top of the plot with the areas of reduced thickness shown as blue patches coincides with the axial coordinate where the sandwich wall enters the groove of the attachment ring. For perspective, the core is 0.2 in. thick. Sections of the test article were also removed from the AFT end near the bolt-hole locations, and revealed indications of core crushing localized to the hole locations seen in Figure 16(b). These indications demonstrated that core crushing had occurred in the same areas as those identified in Figure 16(a). It was concluded that the torque specified for the installation of the attachment ring bolts was likely too high and caused webs of the attachment rings to deform excessively resulting in the core crushing. It was recognized that the torque specification was carried over from the previous assembly procedures intended for metallic test articles that could tolerate much larger through-the-thickness compression and used stiffer steel attachment rings. Since the subject bolts were not in the primary load path, but merely served as a post-failure safety feature, there existed no rationale for torqueing the bolts as prescribed in the assembly procedure.

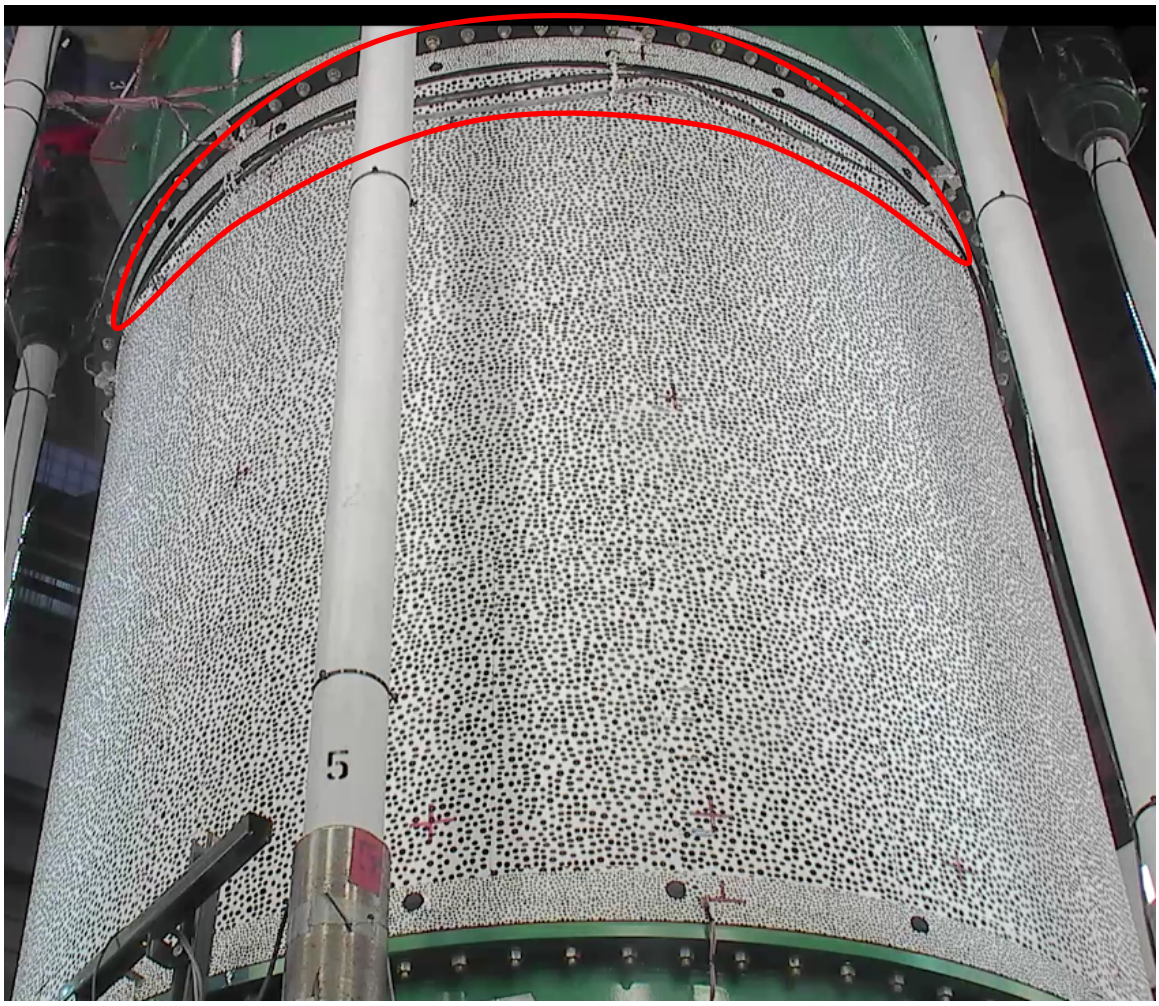

Figure 14. Final failure location in the proximity of the FWD metallic attachment ring termination.

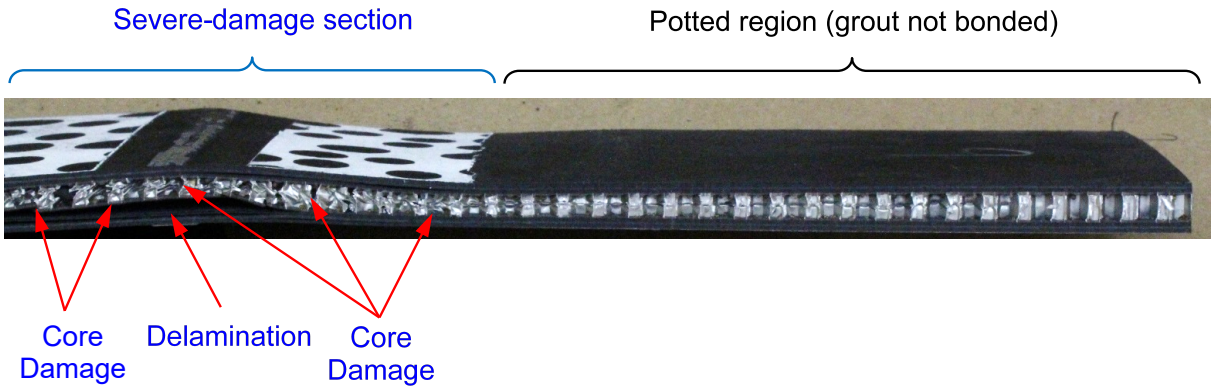

Figure 15. Posttest cross-section in the proximity of the FWD attachment ring.

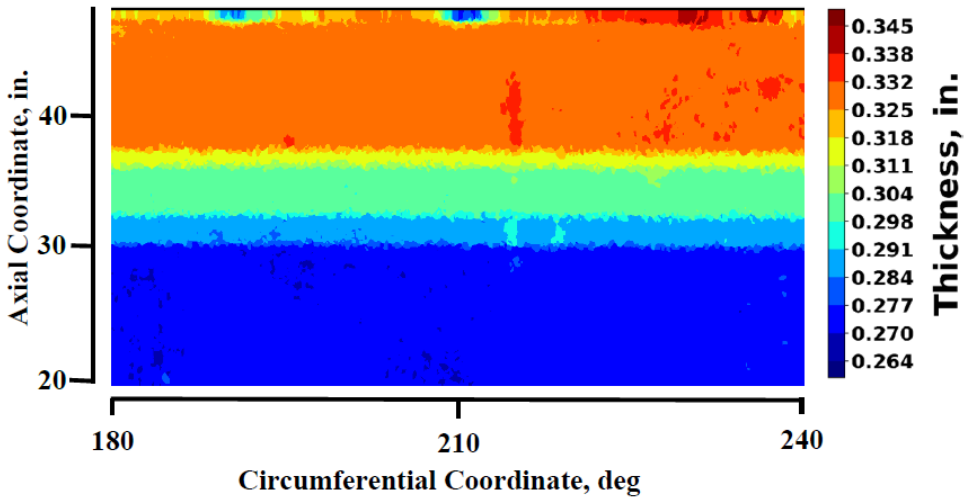

a) As-manufactured thickness measurement for a portion of the FWD end.

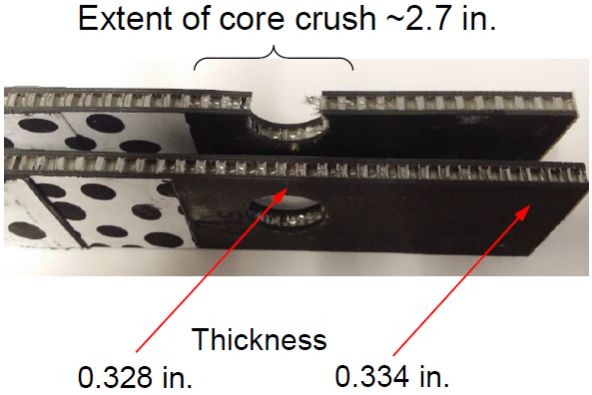

b) Posttest cross-section in the proximity of the AFT load introduction fixture.

Figure 16. As-manufactured thickness measurement for a portion of the FWD end, and posttest cross-section in the proximity of the AFT load introduction fixture.

A series of transverse displacement images obtained using the HS-DIC5 in the proximity of the location shown in Figure 16(a) was examined next. The 10 images shown in Figure 17 were obtained in the 100-ms time intervals during the test article failure event. Considering the quasi-static characteristic of the load application, the transverse displacement amplitude grew very rapidly in the image series, while the increase in the axial uniform end-shortening was minimal. In the first four images of Figure 17, (a) through (d), the amplitude growth is smaller than that on the subsequent three images, and the maximum radial displacement location slowly migrates toward higher circumferential and axial coordinates (to the right and upward within the individual images). The amplitude growth and the rate of the maximum displacement location movement accelerates in the next three images, (e) through (g), although the maximum displacement area retains generally an oval boundary. The area of the maximum radial displacement changes into a more circumferentially elongated pattern in the last three images of Figure 17, (h) through (j), which is likely an indication of the OML facesheet damage consistent with the OML damage shown in Figure 14. While the coordinate of the first rupture of the OML facesheet (as well as the coordinates of the IML facesheet rupture and the honeycomb core damage) cannot be determined with precise accuracy, a reasonable assumption can be made that the final failure originated in the

proximity of the largest radial deformations shown in Figure 17, and that the thickness variations due to pre-existing core damage shown in Figure 16(a) were causal to the failure of the test article.

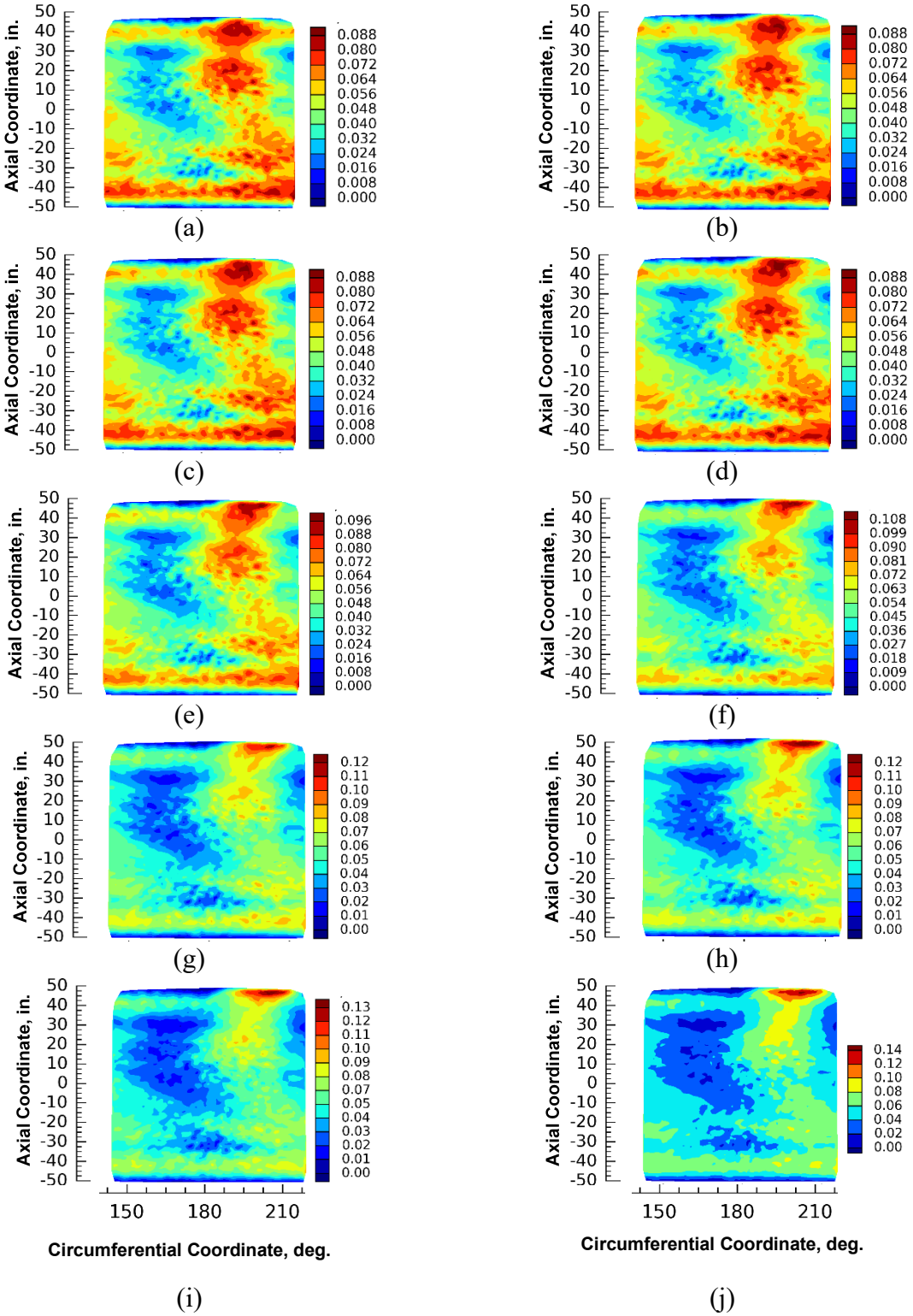

Figure 17. Test radial displacements obtained from the HS DIC in the proximity of the failure load: consecutive images (a) through (j) captured in 100 ms intervals.

3.0 Pretest Analysis And Test Comparison

The pretest predictions were performed using closed-form solutions and shell-element-based finite element analysis (FEA). The closed-form solutions are summarized in Section 3.1, and the finite element modeling and analysis results are summarized in Section 3.2.

3.1 Closed-Form Solutions

The closed-form critical buckling load, P_{cr}^{CF}, for an idealized cylinder without padups was estimated as an initial step in the test article design process. The closed-form loads were also obtained for the following failure modes shown in Figure 18: facesheet wrinkling, P_{FW}, facesheet dimpling, P_{FD}, and core shear crimping, P_{CS}.

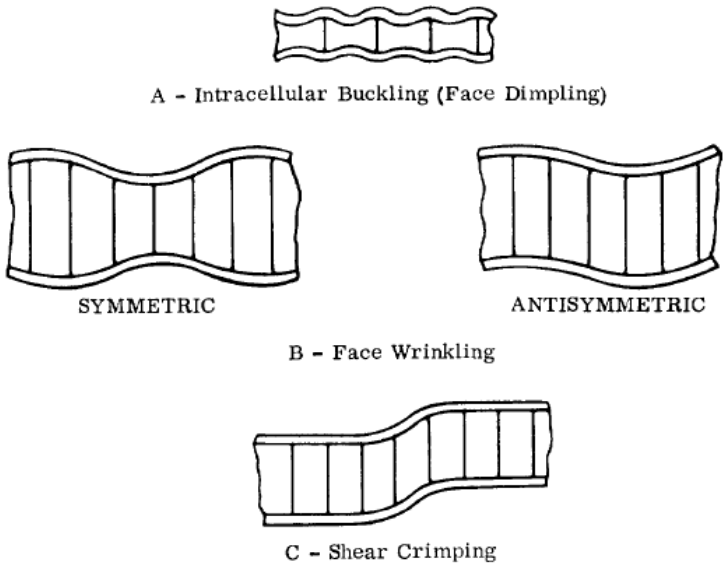

Figure 18. Failure modes considered using closed-form solutions.

Several different formulations were evaluated, and the ones yielding the most conservative results were used and are detailed in Appendix B. The summary of the closed-form results is presented in Table 13. For loads other than the critical buckling load, the corresponding multipliers of the critical buckling load are also presented in Table 13. The most critical damage mode beyond the critical buckling load, P_{cr}, was associated with the core shear crimpling expected to occur at the load that was 2.77 times larger. Consequently, the separation of the desired global buckling mode load over the next possible damage mode load was considered satisfactory.

Table 13. Closed-form loads obtained for the idealized cylinder.

P_{cr}, kips	P_{CS}, kips	P_{FW}, kips	P_{FD}, kips
	P_{CS}/P_{cr} Ratio	P_{FW}/P_{cr} Ratio	P_{FD}/P_{cr} Ratio
973	2700	9200	55,000
	2.77	9.46	56.5

3.2 Global Finite Element Analysis

The global FEM of the cylinder is described in detail in Reference 7 and shown in Figure 19. While in the initial analyses were conducted using the complete model, including the test facility, seen in Figure 19(a), it was quickly ascertained that the compliance of the test stand was insignificant and

did not appreciably affect the FEA results of the test article itself. Consequently, to gain computational expediency, the simplified model, shown in Figure 19(b), was predominantly used for all analyses other than the ones used for real-time test monitoring, i.e., the ones that required test setup-specific outputs, such as individual actuator forces and actuator axial displacements. The global FEA analysis results presented in Sections 3.2 and 4.3 use the simplified model.

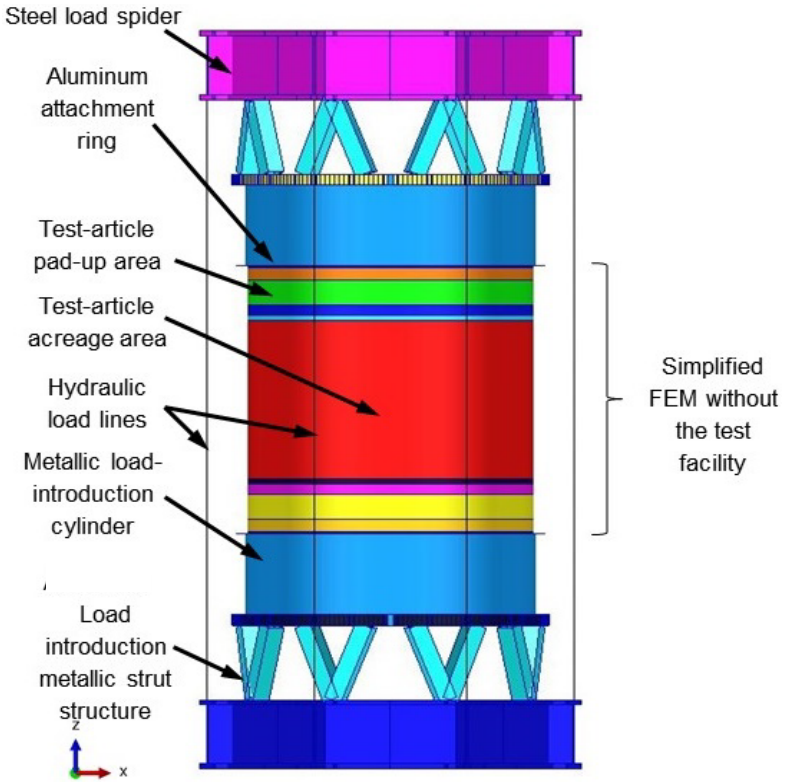

a) Complete, including the test facility.

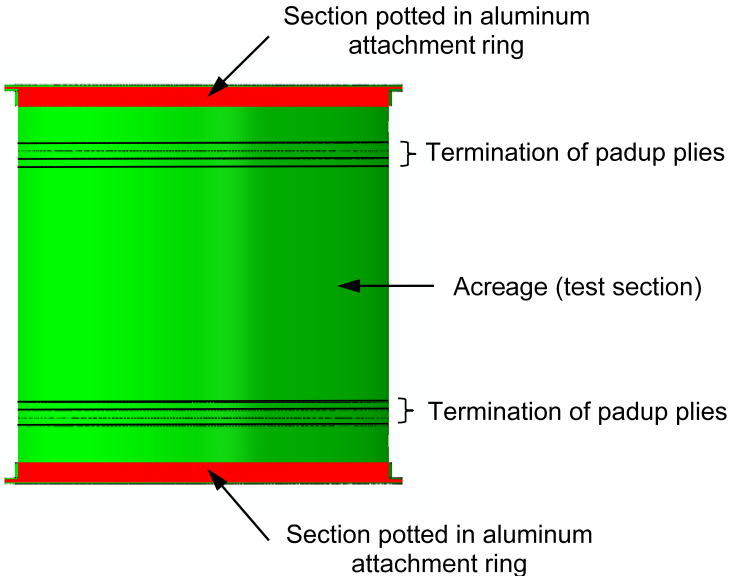

b) Simplified without the test facility.

Figure 19. Global FEM.

The commercial finite element package, Abaqus [8], was used in all FEA efforts. In the simplified FEM, S4R reduced-integration shell elements were used to model the entire sandwich cylinder and the attachment rings. The element size was 0.5 in. in the axial direction and 0.5° (or approximately 0.41 in.) in the circumferential direction. This mesh size resulted in approximately 154,000 elements and 932,000 degrees of freedom (DoFs). The basic material properties (in-plane extensional stiffnesses E_{11} and E_{22}, and in-plane Poisson's ratio ν_{12}) of IM7/8552-1 used in the FEA were obtained from the SBKF-commissioned testing conducted by a vendor [9]. The lamina strength properties (X_t, X_c, Y_t, Y_c, and S) were sourced from an internal NASA memorandum [10]. The properties of the 3.1-pcf aluminum honeycomb core were obtained from Reference 11.

The FWD and AFT attachment ring flanges were attached via kinematic constraints to a single top and a single bottom node, respectively, located on the cylinder axis and in-plane with the test article ends. The bottom node was also fixed, and the top node was displaced axially to compress the cylinder. For computational efficiency, the initial part of the simulation was typically conducted using a static nonlinear solver, and a transient dynamic solver was used near the estimated buckling loading. As a part of the pretest analysis efforts, three types of global FEMs were developed and analyzed: geometrically perfect, with radial imperfections only (per Figure 3), and with both radial and thickness imperfections (per Figure 3 and 4). While the first two analysis types were useful in assessing the imperfection sensitivities, the one with both radial and thickness imperfections was the best pretest attempt to model the as-manufactured test article and, therefore, is the focus of this pretest results section. The effects of using only the radial imperfections and using the combined radial and thickness imperfections on the predicted buckling load are shown in Figure 20. Each geometric configuration of the test-article and their two solutions, labeled *Strains* and *Tsai-Hill*, are presented in Figure 20. The solutions labeled *Strains* used the default layered composite definition used in Abaqus; i.e., three integration points across the thickness of each ply, and were used to obtain all displacement and strain results presented in this report. The solutions labeled *Tsai-Hill* used only a single integration point across the thickness of individual facesheet plies and were used exclusively to obtain the failure indices defined as

$$Failure\ Index = \frac{\text{Analysis Result}}{\text{Allowable}}, \tag{3}$$

where a *Failure Index* greater than one indicates failure. The departure from the Abaqus analysis default of using three integration points across single ply thickness only for the solutions labeled as *Tsai-Hill* was motivated by reducing the size of the solution database file relative to the one labeled as *Strains*. As presented in Figure 20, when end-shortening versus load results were examined, no appreciable differences between the *Strains* and *Tsai-Hill* solutions were noted for the models with only the radial imperfection and with both radial and thickness imperfections. The *Strains* and *Tsai-Hill* solutions for the perfect geometry also compared very well for the majority of the end-shortening versus the applied load curve, and differed slightly only in the plateau region near the load drop. A discussion dedicated to the reasons for the predicted plateau behavior and the solution reliability in this region is presented in Reference 7. The slight difference between the two analysis variants in the plateau region was not perceived as a concern.

The predicted buckling load using the perfect-geometry transient nonlinear FEA was 984 kips, slightly higher than 973 kips predicted by the closed-form solution. At least part of this difference can be attributed to the presence of the padup regions in the FEM, which were not accounted for in the closed-form solution. The plateau behavior seen in Figure 20 might have also contributed to

the nonlinear FEA solution resulting in a higher load relative to the closed-form analysis. The predicted buckling load using the FEA solution with both the radial and thickness imperfections was 864 kips, i.e., 88.8% of the closed-form buckling load.

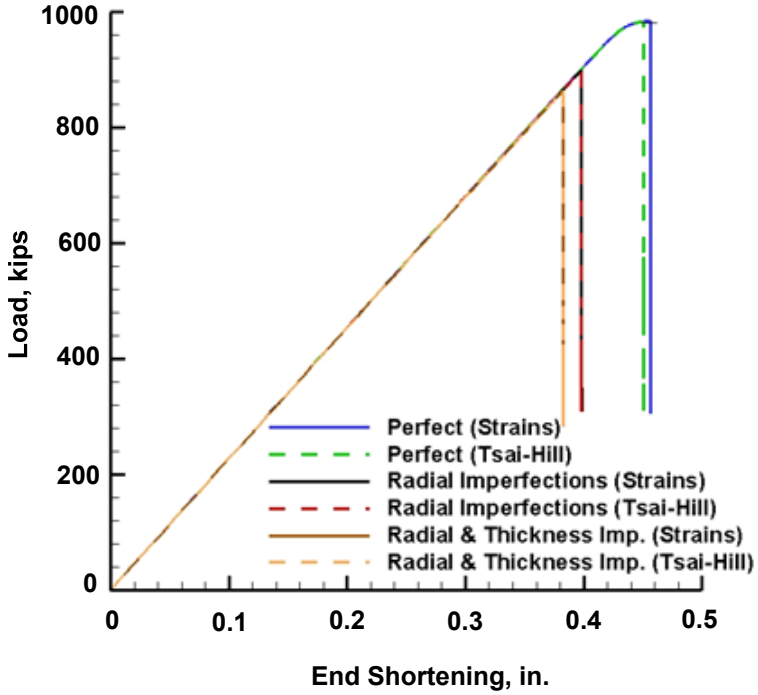

Figure 20. Predicted load versus end-shortening of the test article.

A comparison of the load versus end-shortening results from the test LS8 (load to failure) along with the pretest prediction from the *Strains* variant (per Figure 20) of the solution with both radial and thickness imperfections is shown in Figure 21.

The test article failed at 708 kips, before developing global buckling, with indications that the core failure in the padup region near the attachment rings initiated the failure. The test failure load represented 81.9% of the predicted global buckling load of 864 kips. The test data shown in Figure 21 indicate that the linear stiffness of the test article was accurately captured by the FEM as the test and prediction curves have matching slopes initially. The test article, however, showed indications of slightly nonlinear response characteristics starting around 400 kips, while the prediction curve remained nearly linear up to the peak load. A nonlinear behavior under compressive loading was seen in the material testing conducted in support of the CTA8.2 material characterization, and was also experienced and reported previously in CTA8.1 testing [12].

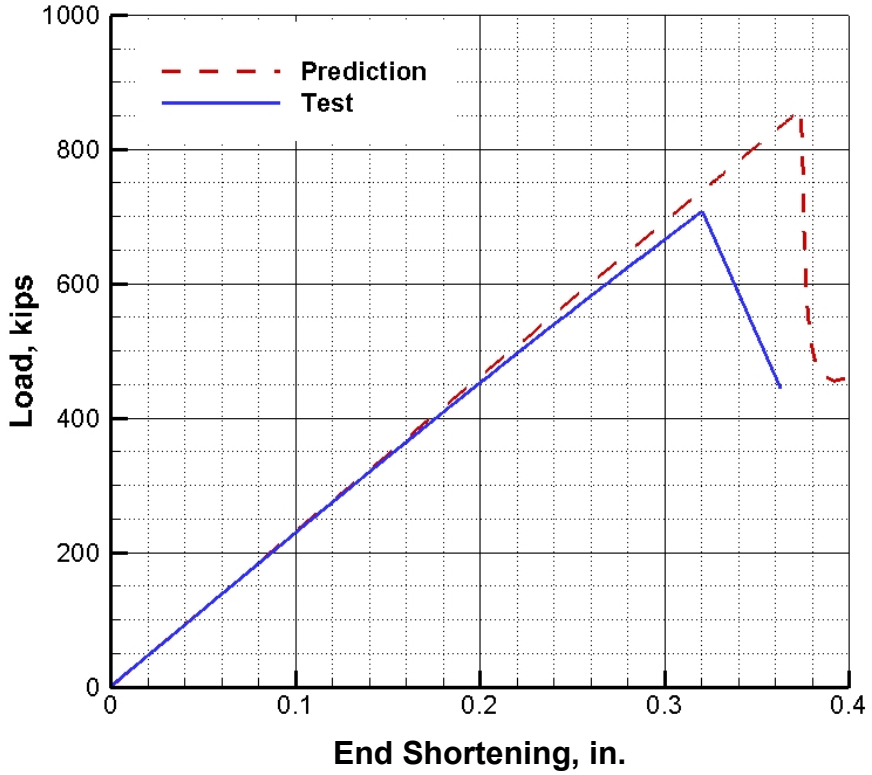

Figure 21. Load versus end-shortening – test versus pretest prediction.

All FEA results presented in the remainder of this section (Figure 22 through 37) were obtained using the as-manufactured geometry presented in Figure 3 and 4. The FEA axial and radial displacement, axial and hoop strain, and Tsai-Hill failure index results corresponding to the predicted failure load of 864 kips are presented in Figure 22 through 29. In these and all other figures of the unrolled test article in Sections 3 and 4, the horizontal dash lines signify termination of padups at the axial coordinates of ±30 in.

The axial displacement, shown in Figure 22, is uniform around the circumference of the cylinder, but the radial displacement, shown in Figure 23, is indicative of incipient buckling. The most prominent radial deformations are observed in the proximity of the termination of the upper padup, i.e., near the axial coordinate of 30 in.

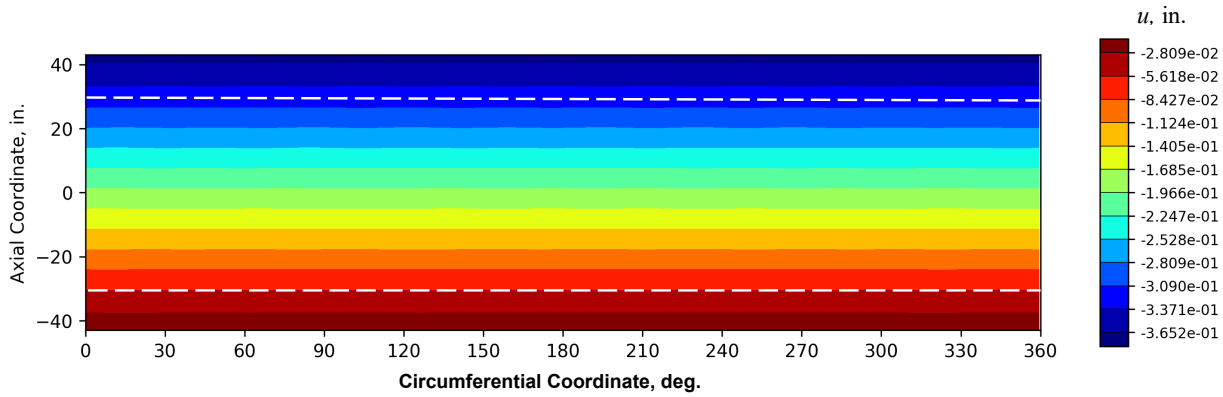

Figure 22. Axial deformation at the predicted buckling load.

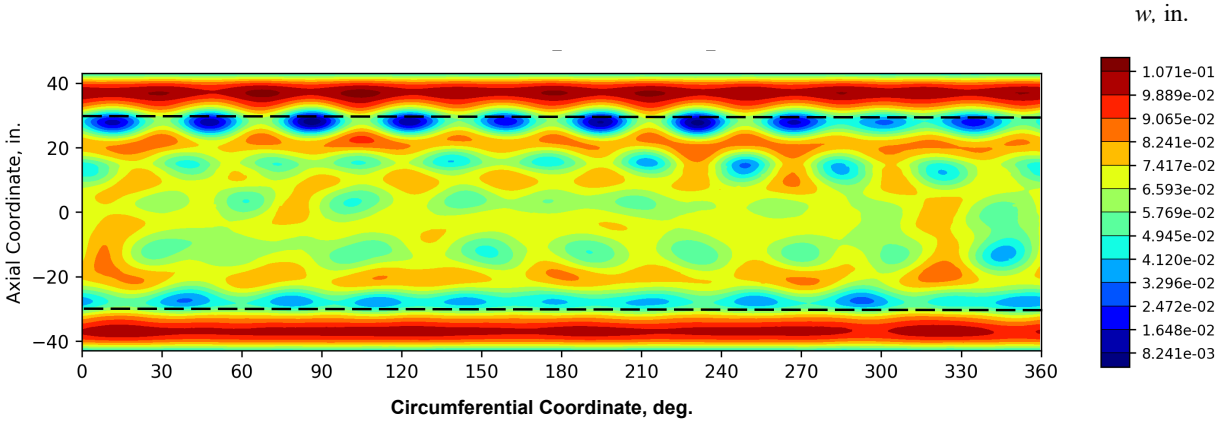

Figure 23. Radial deformation at the predicted buckling load.

The strain results, shown in Figure 24 through 27, also point to the largest axial compressive and tensile hoop strains existing in the proximity of the FWD padup termination. The axial compressive strains are larger in magnitude on the OML facesheet (5314 με), seen in Figure 25, than on the IML facesheet (5151 με) in Figure 24. The average of the OML and IML strain is often referred to as the membrane strain component, and the difference between facesheet strains and membrane strain is referred to as the bending strain. A bending strain component arises due to radial deformations: the minimum (most compressive) axial strain location in the OML facesheet occurs where the total strain is a result of the axial compressive membrane strain and the most negative bending component of the axial strain.

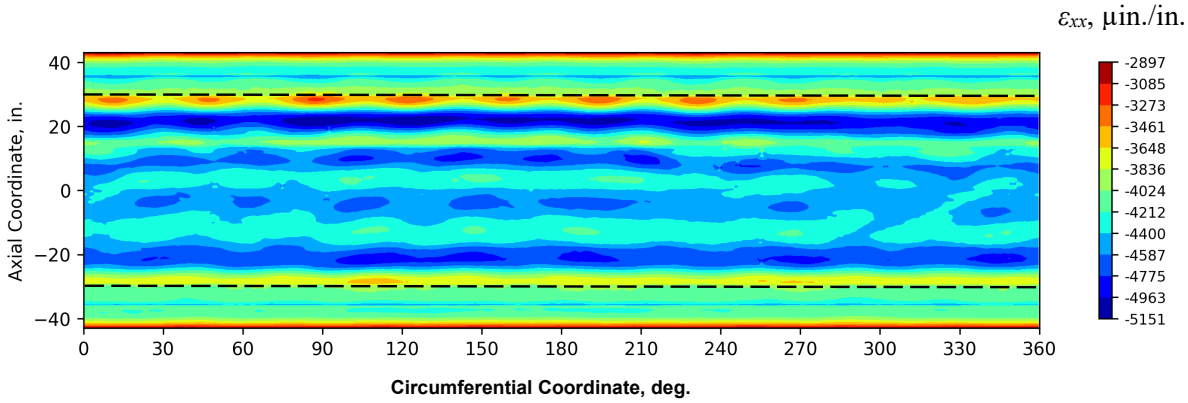

Figure 24. Axial IML pretest predicted strain at the predicted buckling load.

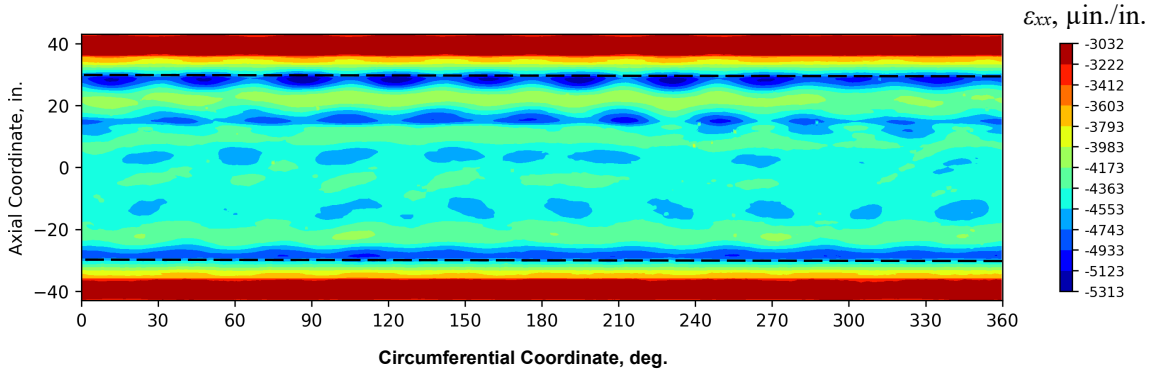

Figure 25. Axial OML pretest predicted strain at the predicted buckling load.

The largest tensile hoop strain occurs in the FWD padup area just outside the attachment rings; i.e., where the cylinder wall experiences a significant and sudden loss of support constraining the hoop expansion. The maximum hoop strains differ only by a small margin between the IML facesheet (2277 με), shown in Figure 26, and the OML facesheet (2232 με), shown in Figure 27. The small difference between the IML and OML tensile hoop strain can be attributed to limited cylinder wall bending in the circumferential directions.

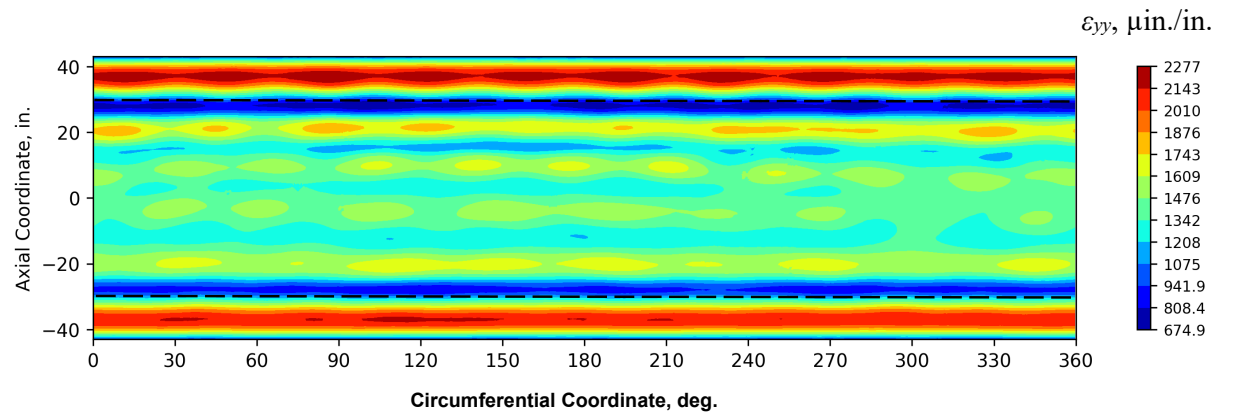

Figure 26. Hoop IML pretest predicted strain at the predicted buckling load.

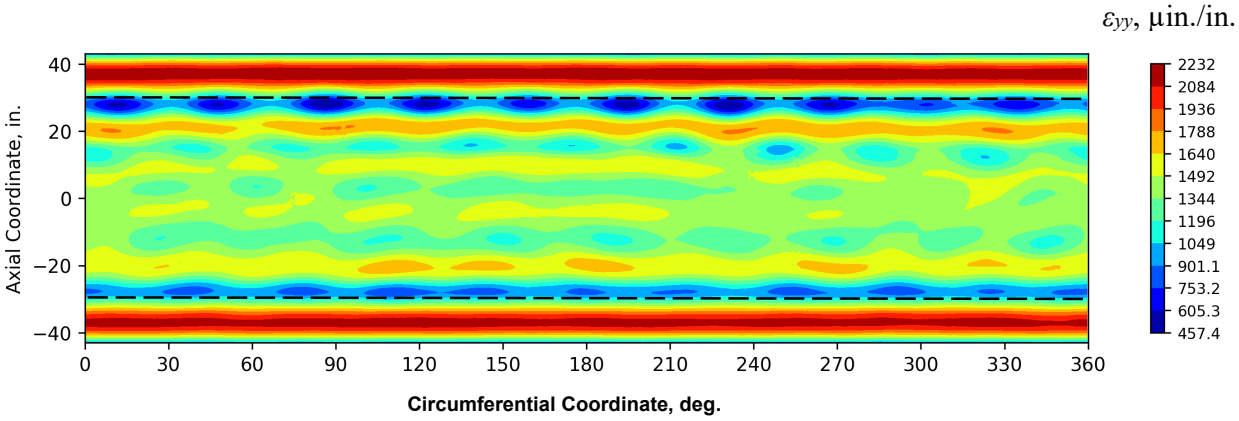

Figure 27. Hoop OML pretest predicted strain at the predicted buckling load.

The Tsai-Hill failure index results are presented in the composite image in Figure 28. The composite representation means that the largest failure index is represented in the plot irrespective of which ply this index was identified in. While a composite plot is informative to ascertain the overall safety margin remaining, it does not provide insight about which ply produces the most critical failure index. Examination of each individual ply is required for such identification. After ply-by-ply examination, the outermost 0-degree ply in the OML facesheet was identified as producing the largest Tsai-Hill failure index and is shown in Figure 29. Since the numbering of the plies in the Abaqus model is sequential, when the overall number of plies changes in the structure, their ordering numbers do so as well. Consequently, a ply represented by a certain ordering number in the acreage area will have a different number in the padup section as additional plies are interleaved. For this reason, only the acreage section of the critical ply is captured in Figure 29. Based on the strain and Tsai-Hill failure index results, the pretest analysis indicated that no facesheet damage should occur before the global buckling event is initiated.

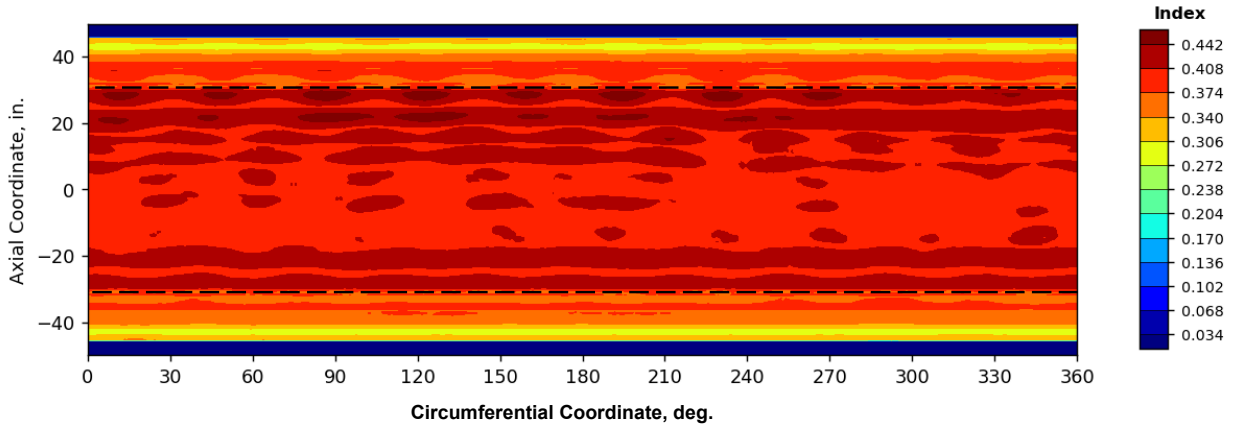

Figure 28. Envelope plot of the pretest predicted Tsai-Hill failure index at the predicted buckling load.

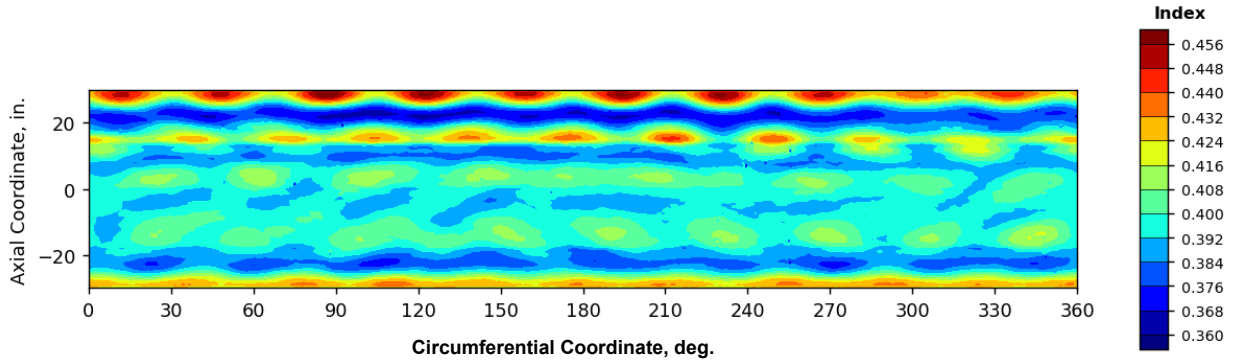

Figure 29. Pretest predicted Tsai-Hill failure index for the critical ply at the predicted buckling load.

Since the predicted failure load was not achieved during testing, the test and predicted axial and radial displacements, and axial and hoop strains are instead compared at the lower load levels where both results were available. Two load levels were selected for the comparison: the last LS8 hold at 643 kips and the incipient failure load of 708 kips. Identical sets of results to those presented below were compared for two additional LS8 hold levels of 456 kips and 541 kips, and no appreciable differences in the quality of agreement between the test and analysis results were noted. Thus, only the 643-kips level is presented for brevity as a representation of subcritical load levels. The results at the incipient failure load of 708 kips are presented to highlight the comparison of the predictive analysis at the largest load achieved in the test even though the quality of this comparison is not significantly different from that achieved at subcritical levels.

The test and pretest predicted results at 643 kips load are presented in Figure 30 through 33. The axial displacement agreement is favorable, as shown in Figure 30. The most noticeable difference between the test and the pretest prediction is a slightly closer alignment of the pretest prediction displacement field with the perfectly axisymmetric pattern while the test results show more pronounced departure from this pattern. The radial displacement comparison in Figure 31 is far less favorable. While both test and prediction show the maximum radial displacements in the padup areas, the displacement patterns are quite distinct. The test results produce generally larger radial displacement amplitudes and exhibit six periodic patterns around the circumference that noticeably lean away from the axial direction. Both the axial strain comparison (Figure 32) and

the hoop strain comparison (Figure 33) are generally acceptable when it comes to the overall strain levels and global distributions. The test results, however, are characterized by far less axisymmetrical pattern with larger strain variations around the circumferential and axial directions.

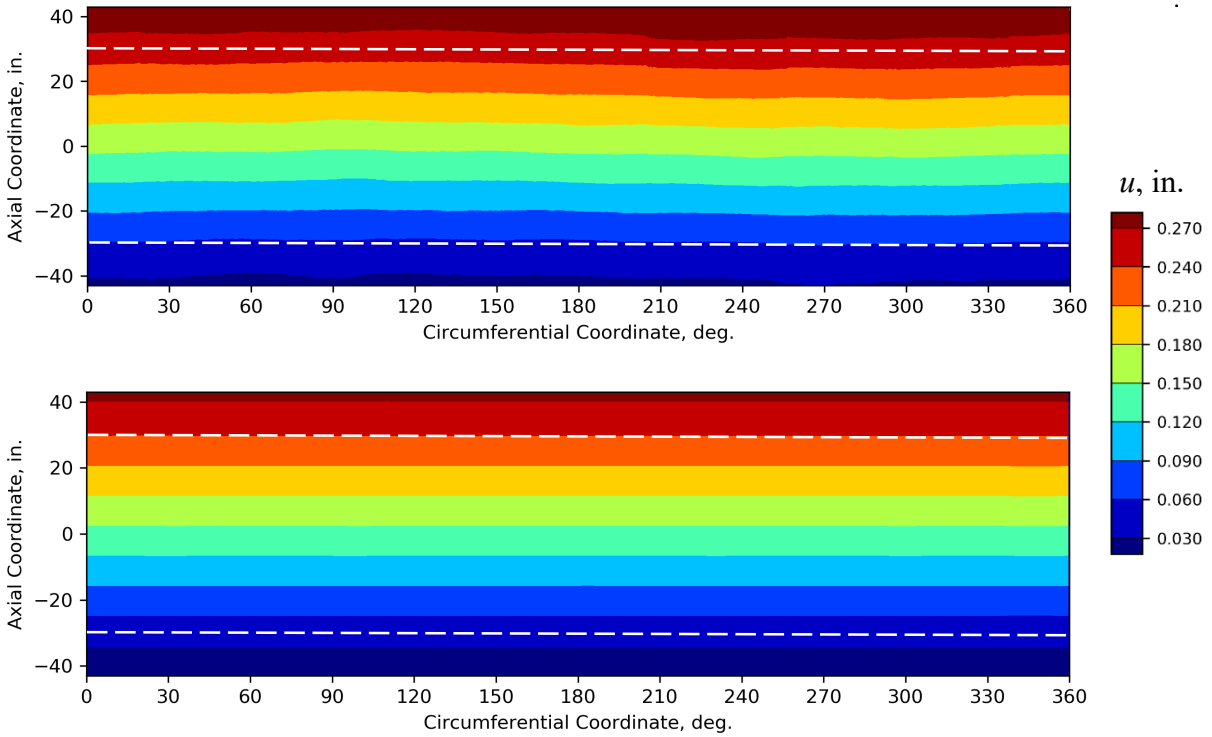

Figure 30. Axial displacement at 643 kips from: test (top) and shell FEA (bottom).

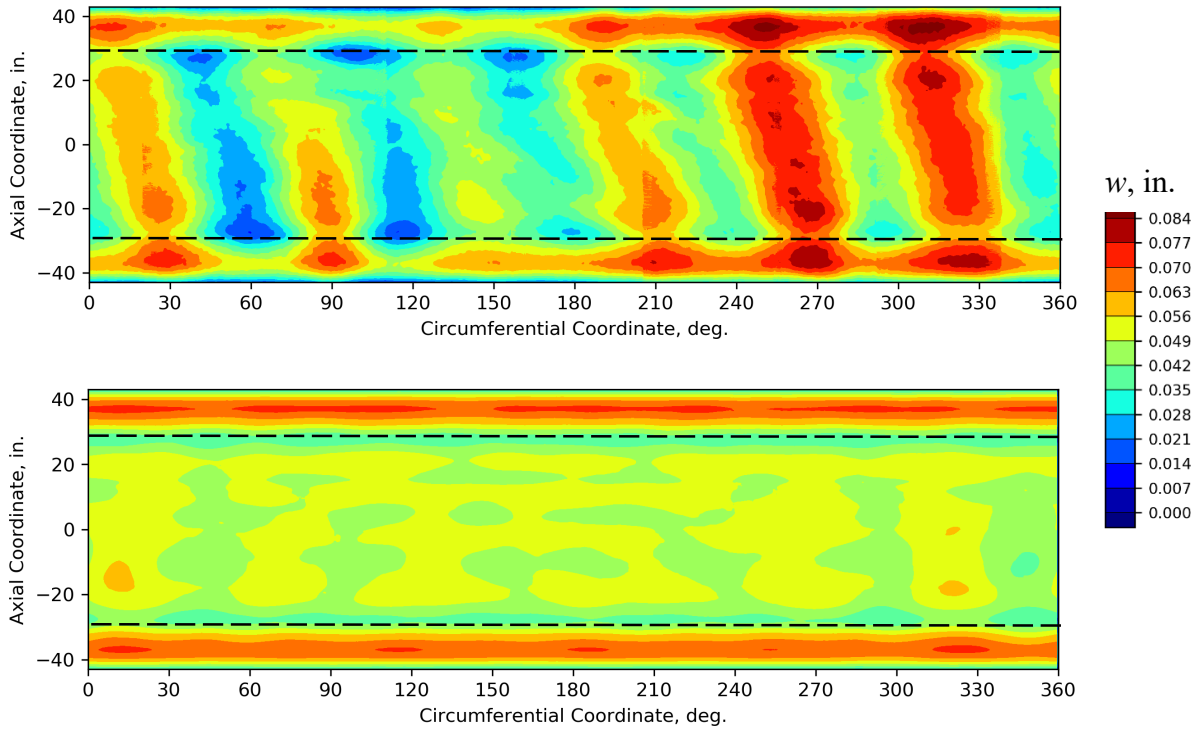

Figure 31. Radial displacement at 643 kips from: test (top) and shell FEA (bottom).

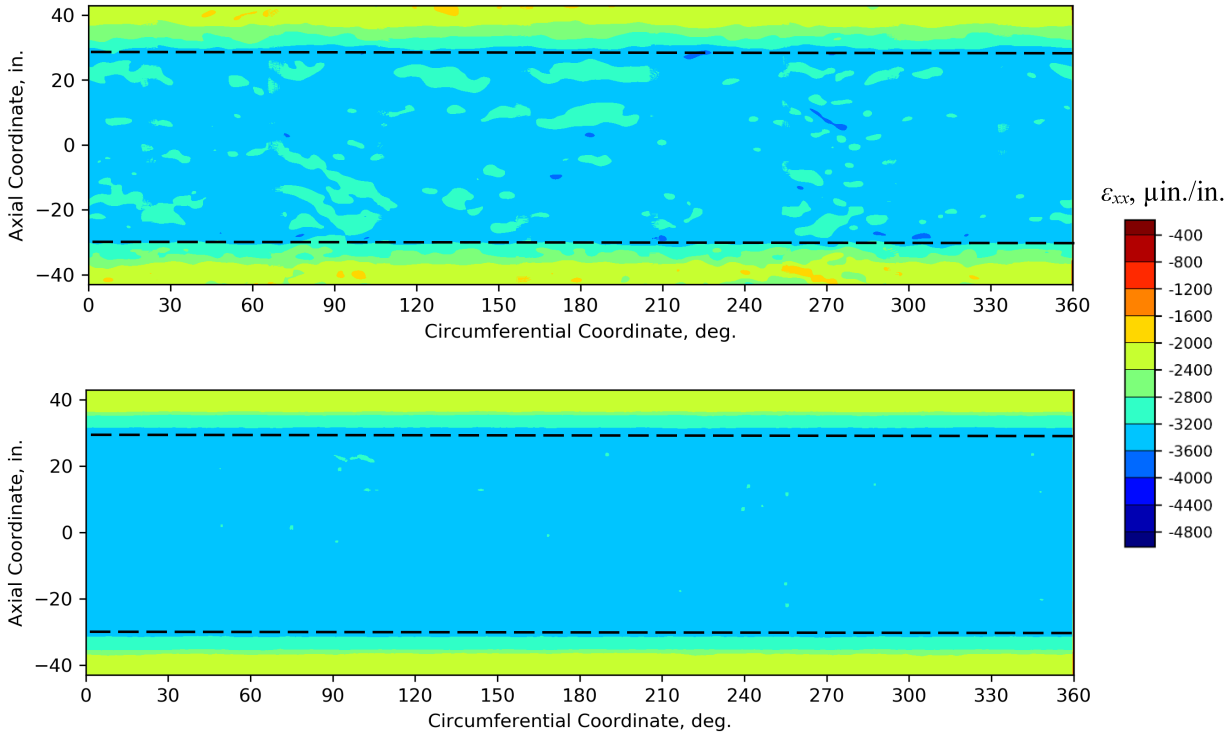

Figure 32. Axial strain at 643 kips from: test (top) and shell FEA (bottom).

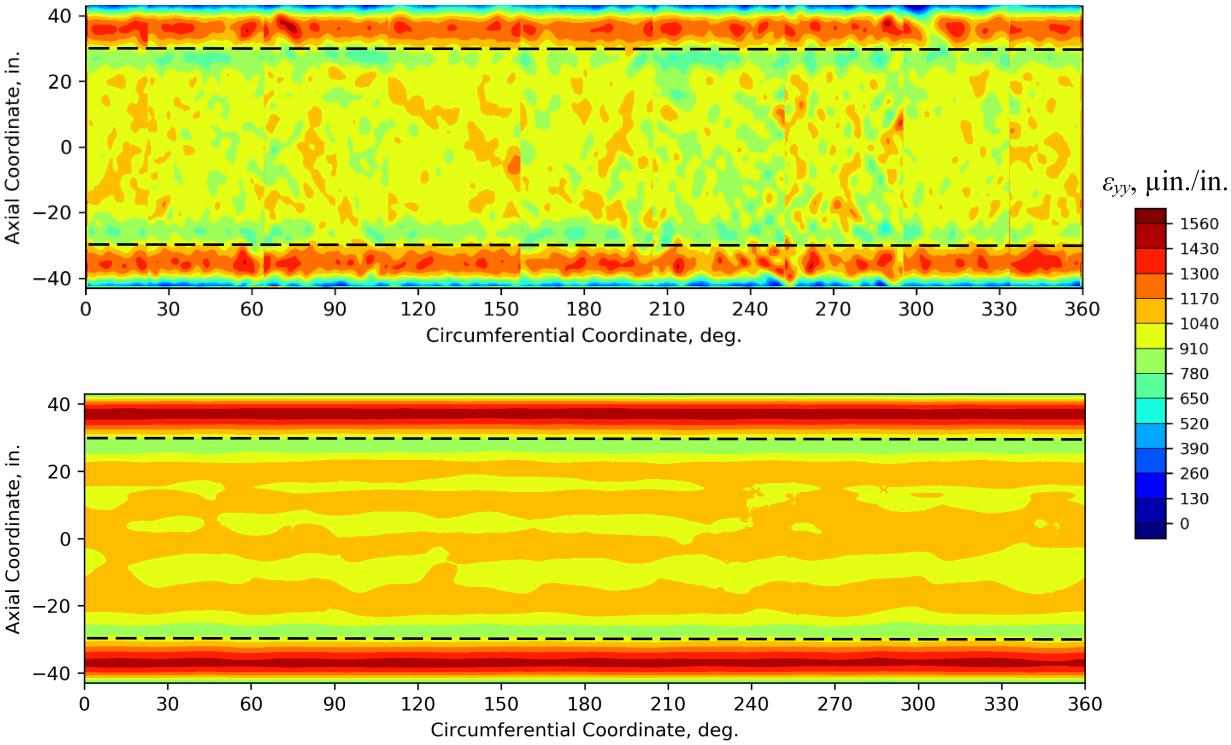

Figure 33. Hoop strain at 643 kips from: test (top) and shell FEA (bottom).

The pretest predictions and test results at the test failure load of 708 kips are presented in Figures 34 through 37. The axial displacement results (Figure 34) compare favorably, with only the test results showing some minor departure from the axisymmetric pattern. This type of response,

however, is not unique to the incipient failure load, and similar but slightly less pronounced departure from the axisymmetric distribution was observed at the lower load level as shown in Figure 30. The radial displacement comparison in Figure 35 is consistently less favorable. The test results and predictions showed the maximum radial displacements in the padup areas, but the displacement patterns and magnitudes showed significant differences again. The test results showed larger radial displacement amplitudes than the predicted results in both the padup and acreage areas. The test response in the acreage was dominated by the six periodic patterns around the circumference that lean away from the vertical axis of the cylinder. Both the axial strain comparison (Figure 36) and the hoop strain comparison (Figure 37) are generally acceptable when the overall strain levels and global distributions are considered. Similar to the results at the 643 kips load level, the test results are characterized by far less axisymmetrical pattern than the analysis results, with larger strain variations around the circumferential and axial directions.

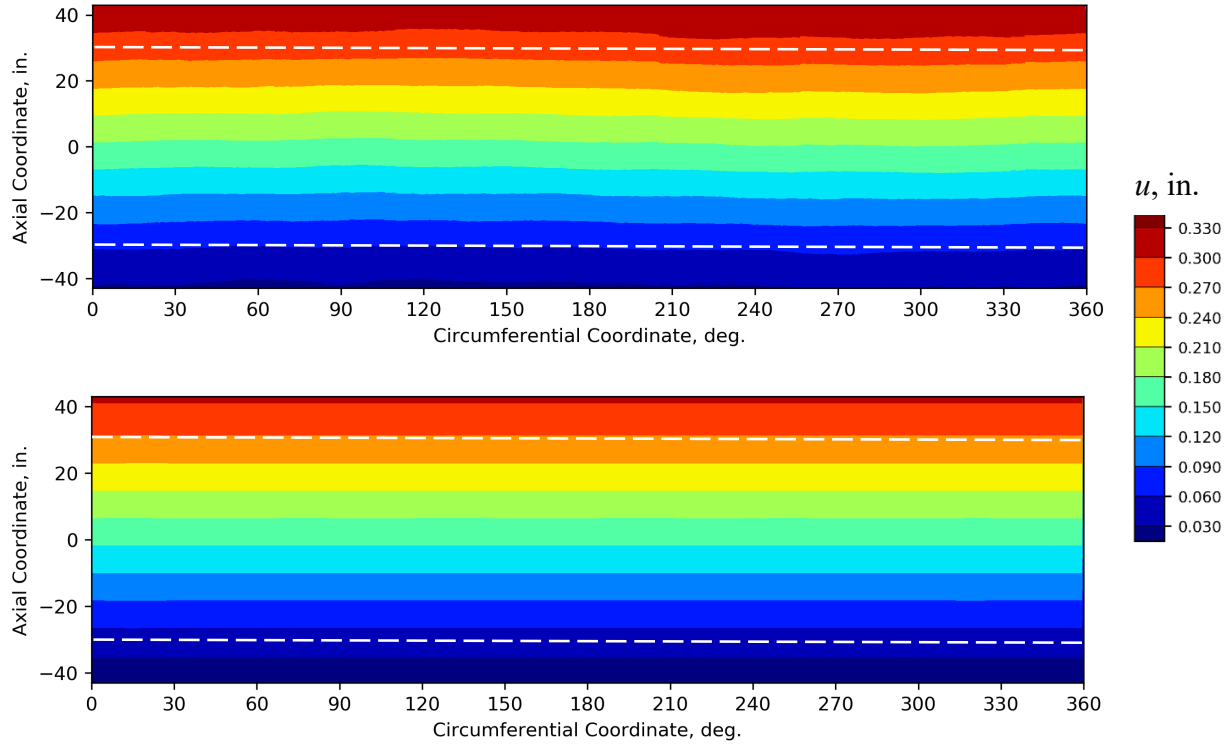

Figure 34. Axial displacement at 708 kips from: test (top) and shell FEA (bottom).

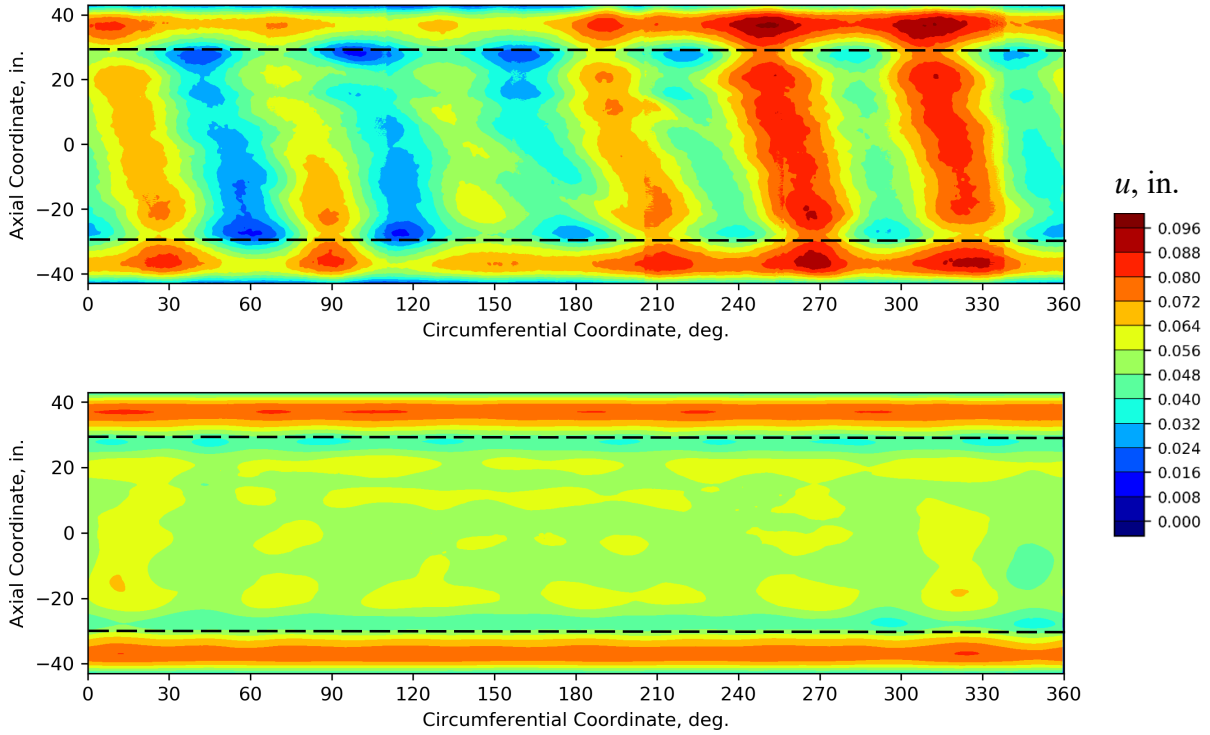

Figure 35. Radial displacement at 708 kips from: test (top) and shell FEA (bottom).

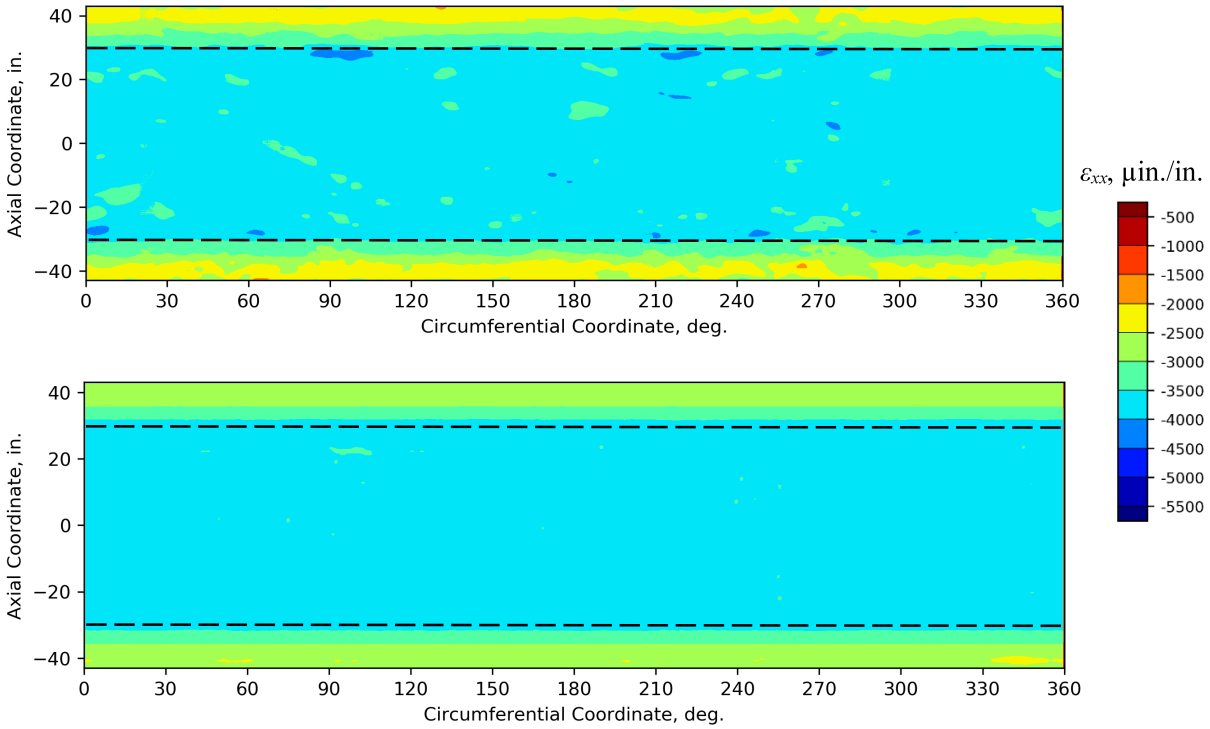

Figure 36. Axial strain at 708 kips from: test (top) and shell FEA (bottom).

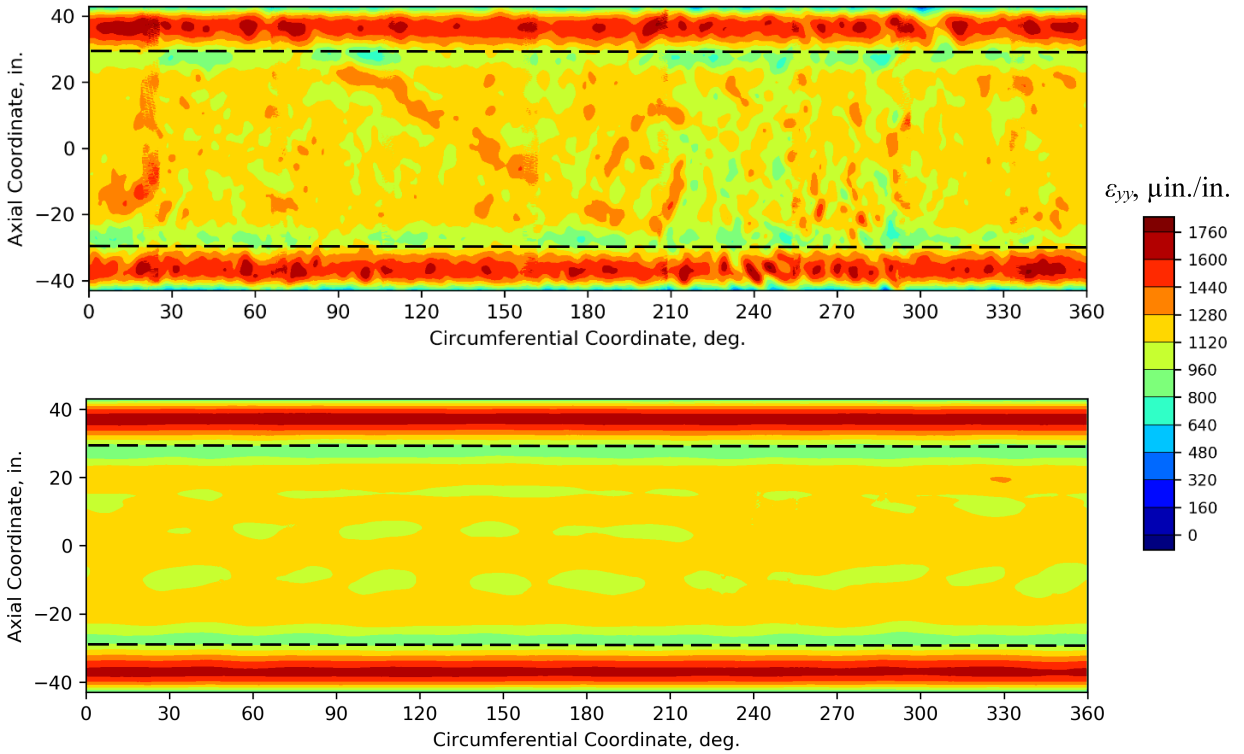

Figure 37. Hoop strain at 708 kips from: test (top) and shell FEA (bottom).

The results presented in Figure 30 through 37 indicate that consistently good agreement of the pretest predictions was limited to the compressive axial displacements. While the axial and hoop strains compared with marginal to acceptable quality, the radial displacement predictions did not capture the essential characteristic of the response, i.e., the six undulations with a pattern noticeably departing from the axial alignment. The number of undulations or alignment of the pattern could not be correlated to any known features of the test article and experimental set up, such as the core splicing pattern, number of bolts in the load introduction fixtures, or number of actuators in the test stand. Furthermore, the pretest FEA based on the shell element model was not suitable for gaining insight into honeycomb core performance under normal (crushing) and transverse shear responses. Consequently, additional posttest analyses with revised modeling assumptions were sought in order to better understand performance of the honeycomb core and to improve the test-analysis correlation.

4.0 Posttest Analysis and Test Comparison

The two honeycomb core failure modes identified in Section 2.6.9, namely core transverse shear failure and core crushing, were not evaluated in the pretest analyses due to the limitations of the closed-form solutions and application of the global shell element-based FEA. Consequently, posttest observations indicated one of these failure modes may have caused the premature failure of CTA8.2. Therefore, an additional investigation of the core performance was conducted that was based on the axisymmetric element-based FEA and is summarized in Section 4.1. Effects of padup ply drops on core performance were also investigated with this model. A drawback of this axisymmetric analysis is that any geometric imperfections introduced into the axisymmetric model would have a non-realistic axisymmetric shape. To that end, an additional FEM with a combination of continuous shell and solid elements (referred to herein as a global-local model) was also

developed to aid in gaining insight into the effects of the realistic imperfections on the core performance. The same global-local model was also used to ascertain if any analysis fidelity loss could be attributed to the shell element modeling of the entire sandwich composite cylinder wall rather than using the solid elements to model the honeycomb core, and the continuous shell elements to model the facesheets, including padups. The global-local model was also intended for investigating the effects of ply drops in the padup areas. The global-local analysis is summarized in Section 4.2. Finally, another global shell-element-based FEM was created using the initial radial imperfections from the full-field DIC systems measured with the test article already installed in the test stand. The analysis using this FEM is referred to as "with as-installed imperfections," and is presented in Section 4.3.

4.1 Axisymmetric Finite Element Analysis

The axisymmetric element-based FEM is shown in Figure 38 and was primarily used to interrogate the core crush and core transverse shear strength failures, but was also used to interrogate core-to-facesheet interface stresses. Abaqus four-noded CAX4 axisymmetric elements were predominantly used to model half of the cylinder height, including the sandwich structure facesheets and core, as well as the attachment rings and the potting grout. Individual plies were each modeled with one layer of CAX4 elements. The sandwich core, attachment ring, and potting grout were modeled with multiple CAX4 elements across the thickness (i.e., in the radial direction). The ply drops were modeled to occur over a distance of twice a ply thickness, using CAX4 elements and a small number of three-noded CAX3 axisymmetric elements, as shown in the ply drop inset at the top of Figure 38. Using micrographs that became available after the analysis was completed, the as-modeled ply-drop dimension was found to be unrealistically short. The axisymmetric model included approximately 220,000 elements and 685,000 DoF. A geometrically nonlinear solver was used to obtain solutions.

The decision to model only half of the cylinder height was motivated by improving computational efficiency, and the observation that the largest displacements, stresses, and strains in the core of the perfect-geometry model were expected to be near the ends of the test article. The bottom of the model was fixed and the midlength location was represented by assigning the symmetrical boundary conditions and an axial compressive load. These end conditions effectively meant that only odd numbers of axial halfwaves were allowed in the solution (an even number of halfwaves would require application of the antisymmetric boundary conditions at the midlength location). However, realistic geometric imperfections and buckling modes with circumferential variation also could not be implemented or predicted with the axisymmetric model, so this model was constructed using only the perfect cylinder geometry and was not used for primary assessment of the buckling response. Rather, the axisymmetric model was used to evaluate the core crush and transverse shear stresses up to the buckling load because these stresses were not available from the shell element-based FEA. Even if the shell model and the axisymmetric model would produce different buckling shapes, the core response metrics obtained slightly below the buckling load from the axisymmetric analysis were still valuable for the assessment of the core at incipient buckling.

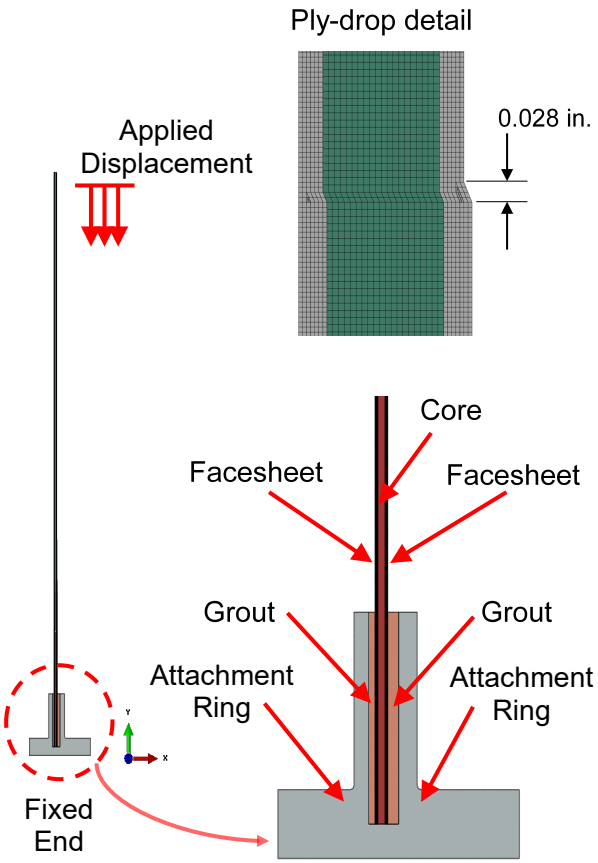

Figure 38. Axisymmetric FEM.

Several variants of the axisymmetric analysis were performed. The main difference between these variants was in how the interaction between the sandwich cylinder wall and the potting grout within the groove of the attachment ring was modeled. Specifically, that interface was modeled as both sliding contact and fixed (fully bonded) interactions. As discussed in Section 2.4, mold release was applied to the test article and attachment rings prior to potting to preclude bonding at those interfaces. Therefore, a sliding contact interaction, i.e., allowing sliding and/or separation between both OML and IML facesheets and the potting grout, was assumed to be the modeling baseline. This variation of the axisymmetric model is referred to as *sliding* in the remainder of this report, and the sliding interactions were modeled to be frictionless. A sensitivity study with a wide range of friction coefficients showed that, short of being completely fixed, there was little influence of friction on the predicted response. Analyses using the Abaqus tie command to fix the surfaces, termed the *tied* condition, were also performed. This condition was representative of an ineffective application of the mold release to the ends of the test article and the attachment rings in the potting process.

Beyond the baseline sliding interaction and the tied interaction, another constraint condition variation was the assumption that the OML facesheet surface was tied to the grout in the attachment ring while the IML facesheet surface had the sliding interaction, i.e., free to slide and/or separate from the grout. This analysis variant is used to simulate the condition where the growing radial expansion of the loaded cylinder at its potted ends resulted in a large surface pressure being exerted by the OML facesheet on the grout. It was envisioned that such a pressure combined with the insufficient application of the release agent could result in the locking of the two surfaces. This

variation of the axisymmetric model is later referred as *sliding IML/tied OML*. The tied and sliding IML/tied OML model variants were intended to give insight into "the worst-case scenario," i.e., when the cylinder-grout interactions were off-nominal. Additionally, a presence of a slight grout fillet at the end of the metallic attachment ring grove was noted in the process of installing the test article into the attachment rings. When modeled in the axisymmetric analysis it was found to mitigate some of the high core stress conditions at the attachment ring termination. Consequently, the results with and without the grout *fillet* feature were also obtained.

The axisymmetric analysis results were first checked against the already available shell element-based analysis results. Specifically, the load versus end-shortening curves (Figure 39) and radial displacement profiles in the proximity of the predicted failure load (Figure 40) were selected for the comparison. The load end-shortening agreement shown in Figure 39 was favorable overall, with the axisymmetric element-based analysis with the sliding boundary condition (with and without fillet) showing slightly softer responses than the remaining analyses. The axisymmetric element-based analysis with the sliding boundary condition was the only analysis in Figure 39 where relative movement between both test-article facesheets and the potting grout within the attachment ring was permitted and observed to take place, including observed separation of the IML facesheet from the grout. This modeling feature and response characteristic was likely responsible for the increased compliance of the sliding boundary model relative to the remaining models.

The agreement of the radial displacement profiles, shown in Figure 40, was also good overall, especially when the far field results away from the attachment ring/potting area were considered. The axisymmetric analysis solution using the sliding boundary condition (with and without fillet) appeared to be in the best agreement with the shell element analysis solution, while the axisymmetric analysis solution with the sliding IML/tied OML boundaries appeared to compare least favorably. To better interpret the results in Figure 40, it was important to consider that the radial displacement in the shell element model was obtained from a single node located approximately in the midsurface of the element. Furthermore, in the attachment-ring area, the shell element model had a significant thickness that accounted for the metallic attachment ring, potting grout, and the sandwich cylinder wall with the padup plies, all within one layered shell element. The radial displacements for all the axisymmetric model variants were obtained from the outer-most node of the OML facesheet. While radial displacements obtained from the two distinct model types and node locations were perceived as comparable outside the attachment ring, the comparison within the fitting was likely more affected by the above-discussed modeling differences. Therefore, the best agreement between the shell analysis results and the axisymmetric analysis results with the sliding boundary might have been incidental due to the modeling oversimplification within the shell element model in the attachment-ring section.

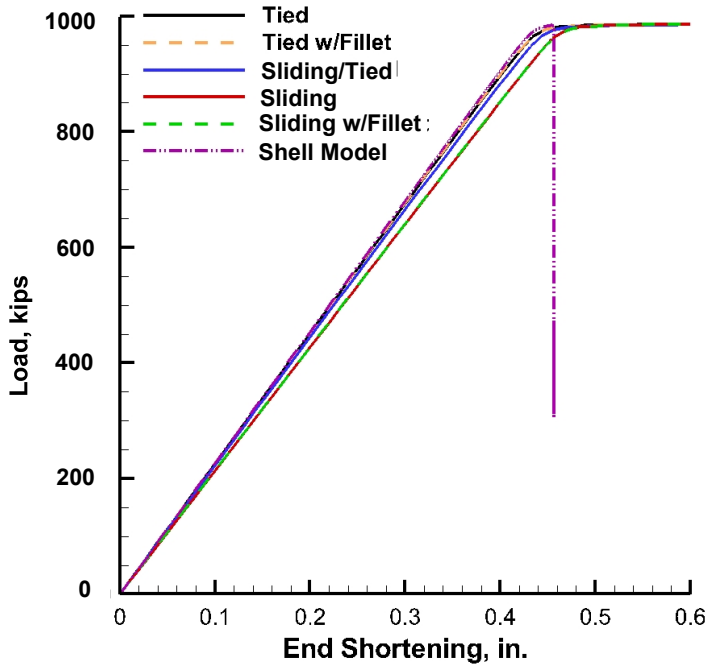

Figure 39. Predicted load versus end-shortening of the test article obtained from shell and different axisymmetric FEA variations.

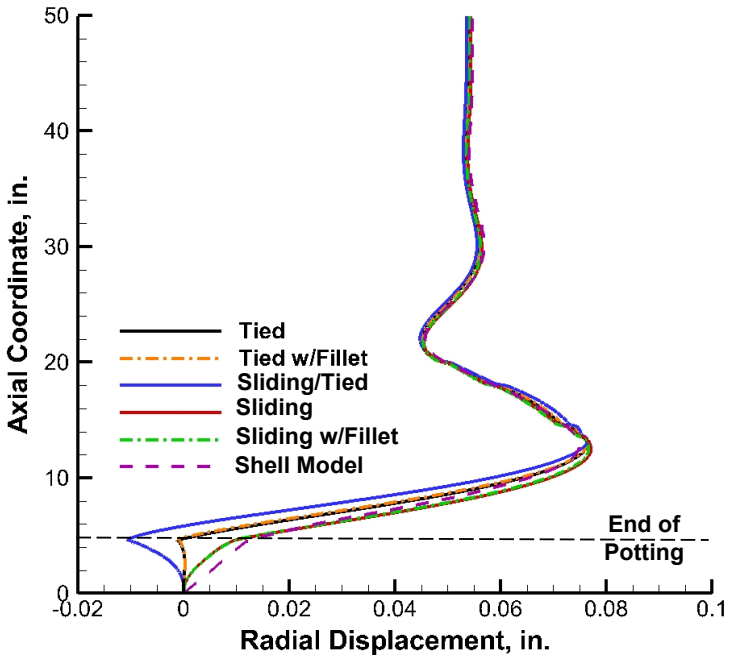

Figure 40. Radial displacement at the failure load of 708 kips obtained from the shell and different axisymmetric FEA variations.

The general areas of high crush and transverse shear stresses identified by the axisymmetric analyses are highlighted in Figure 41. The peak crush stresses were identified on the OML side of the honeycomb core at the location coinciding with the termination of the attachment rings, as shown in Figure 41(a). This result was quite intuitive due to the abrupt change in the radial stiffness occurring at this location. High transverse core shear stresses were identified at two locations, one

above (positive transverse core shear stress) and one below (negative transverse core shear stress) the termination of the attachment ring webs, as shown in Figure 41(b). The high transverse core shear response above the web termination extended farther away from the edges of the attachment ring web (the section of the core shown in red) than the response within the attachment ring grove (the section of the core shown in light blue). Finally, the spatial extent of the high transverse shear stresses and the peak stress location varied only slightly (not shown) depending on the type of interactions (tied, sliding, or sliding IML/tied OML) assumed between the sandwich cylinder wall and the potting grout.

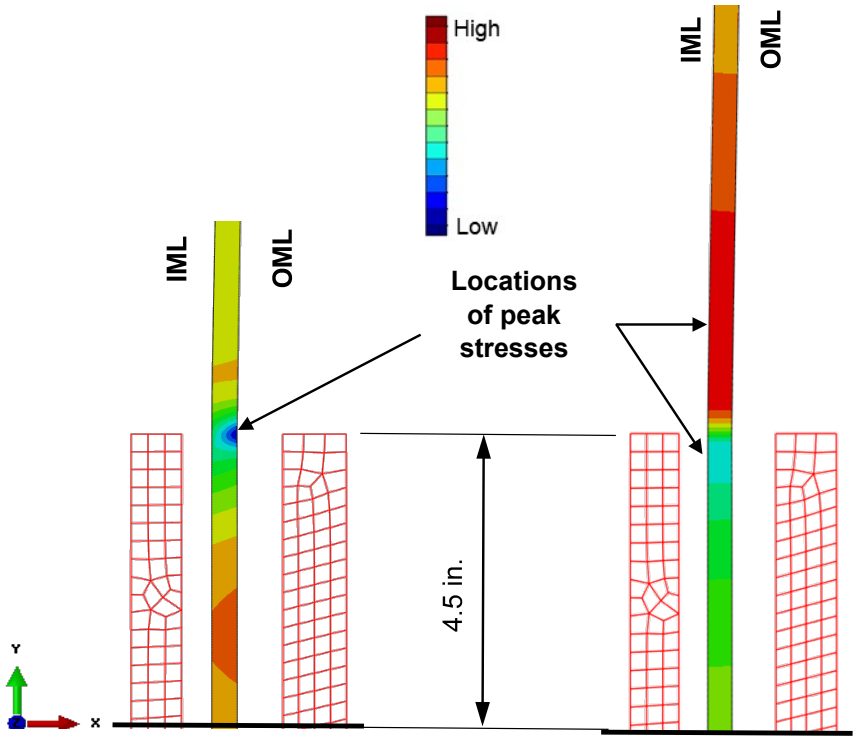

a) Crush. b) Transverse shear.

Figure 41. Core stress components distribution in the proximity of the metallic attachment ring at the test failure load of 708 kips (the potting grout is not shown).

The peak crush and transverse shear stresses inside and outside the attachment ring are shown in Table 14. Each entry in the red font indicates the failure index exceeding a value of one; i.e., resulting in failure. For each metric in Table 14, two failure indices were computed, one based on the typical core failure stresses and one based on the minimum core failure stresses, as published by the core manufacturer [11]. As shown in Table 14, the core crushing was the more critical failure mode when compared to the core transverse shear. The absolute values of the core transverse shear were higher at the location within the attachment ring than outside the ring for the two variations of the tied boundary conditions. The trend was reversed for the remianing boundary conditions. The boundary interactions, other than sliding with fillet, could result in the premature failure of the test article, especially if an adhesive bond developed and was sustained throughout the entire load application sequence. More specifically, when the minimum crush core properties were considered, a failure index in excess of three was obtained for the fully tied interaction, and a failure index in excess of two was obtained for the sliding IML/tied OML interaction. Even for the sliding boundary conditions, a failure index around 0.99 was obtained for the configuration

with the grout fillet and 1.13 without the fillet. Since the failure index of one or greater indicates failure, these results substantiated a strong possibility of the core failure initiating the final failure during LS8. In the posttest examination of the cylinder it was noted that some core damage originating from the attachment ring installation might have existed before the test, so referencing minimum core properties rather than typical appeared more appropriate. The results presented in Table 14 further emphasized the importance of proper application of the release agent during the potting operation, and showed how sensitive the load introduction design was to the details of the test article preparation.

When reviewing the core analysis results in Table 14, it is noted that the failure indices computed for the crush and transverse shear modes were considered in isolation. In other words, the homogenized treatment of the core in the axisymmetric analysis did not facilitate accounting for the cumulative effect of core crushing and transverse shearing.

Table 14. Summary of analysis results for different variations of the axisymmetric FEM under the test failure load of 708 kips.

Model	**Failure Metric and Location**								
	Through the Thickness Compression (Crush Load)			**Transverse Shear Outside the Attachment Ring**			**Transverse Shear Inside the Attachment Ring**		
	Predicted Stress σ_{11}, psi	**Failure Index Using**		**Predicted Stress σ_{13}, psi**	**Failure Index Using**		**Predicted Stress σ_{13}, psi**	**Failure Index Using**	
		Typical Strength	**Min. Strength**		**Typical Strength**	**Min. Strength**		**Typical Strength**	**Min. Strength**
Tied, No Fillet	-970	2.77	3.73	220	0.88	1.10	-269	1.08	1.35
Tied, w/Fillet	-824	2.35	3.17	220	0.88	1.10	-255	1.02	1.28
Sliding, No Fillet	-295	0.84	1.13	182	0.73	0.91	-141	0.56	0.71
Sliding w/Fillet	-258	0.74	0.99	181	0.72	0.91	-138	0.55	0.69
Sliding IML/Tied OML, No Fillet	-670	1.91	2.58	269	1.08	1.35	-262	1.05	1.31

The results pertaining to the core-to-facesheet normal stress and the shear stress over the test article height are shown in Figure 42 and 43, respectively. Both normal and shear stresses shown in these figures are computed in the smeared sense; i.e., they are averaged over the facesheet areas. Only half of the total height is presented on the vertical axis of the figures due to the model symmetry, and the 0-in. station corresponds to the bottom of the attachment ring. The normal stresses, shown in Figure 42, were generally low, except for a few characteristic locations. Apart from the metallic attachment ring termination at the 4.625-in. station, indicated with the blue dashed line, the remaining normal stress spikes were associated with the padup ply drops, indicated with the red dashed lines at stations 13.5 in., 14.5 in., 18 in., and 20 in. These stress spikes associated with attachment ring termination and padup ply drops each occurred in spatial domains confined within few individual CAX4 elements of the axisymmetric model and were smaller than the actual honeycomb cell sizes. This dimensional relationship, combined with the homogenized core

modeling assumption, made the localized high normal stress values unreliable and essentially highlighted a limitation of the axisymmetric analysis with the homogenized core modeling.

The core-to-facesheet shear stresses are shown in Figure 43. Observations similar to those made for the normal stress results in Figure 42 could be made for the shear stresses as well. The shear stresses were generally low, except for the same few characteristic locations. Apart from the proximity of the attachment ring termination at the 4.625-in. station, indicated with the blue dashed line, the remaining transverse shear stress spikes were associated with the padup ply drops indicated with the red dashed lines at stations 13.5 in., 14.5 in., 18 in., and 20 in. These stress spikes also occurred in spatial domains confined within few individual CAX4 elements and much smaller than the actual honeycomb cell sizes. This dimensional relationship, combined with the homogenized core modeling assumption, made the localized high shear stress values unreliable and essentially again highlighted the limitation of the axisymmetric analysis with the homogenized core modeling.

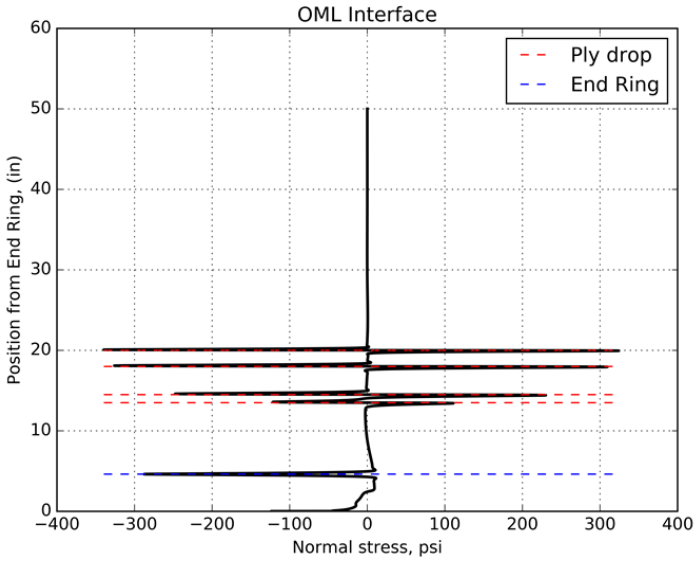

Figure 42. Smeared normal stress in the honeycomb core.

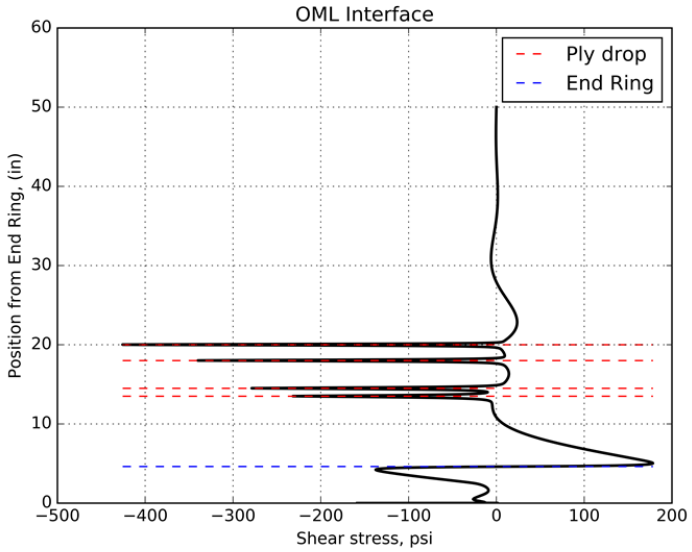

Figure 43. Smeared transverse shear in the honeycomb core.

4.2 Global-Local Finite Element Analysis

The global-local analysis was primarily used to assess the honeycomb core performance without the limitations of the axisymmetric analysis stated in Section 4.1, most importantly the inability to incorporate realistic geometric imperfections in the axisymmetric model. For the global-local model, the global part of the analysis was performed with the shell FEM, as described in Section 3.2. Spatial domains for the local modeling were chosen based on what was perceived as a possible performance-critical core location based on the global analysis. This selection methodology constituted possibly the weakest attribute of the approach: while large rates of radial deformation and/or facesheet strain levels might have been a good indication of core critical performance locations, there was no guarantee that such a selection criterion would be a completely reliable selector for the spatial domains subjected to the local analysis. The selected spatial domains, Local 1 and Local 2, of the local models are highlighted with black rectangles in Figure 44.

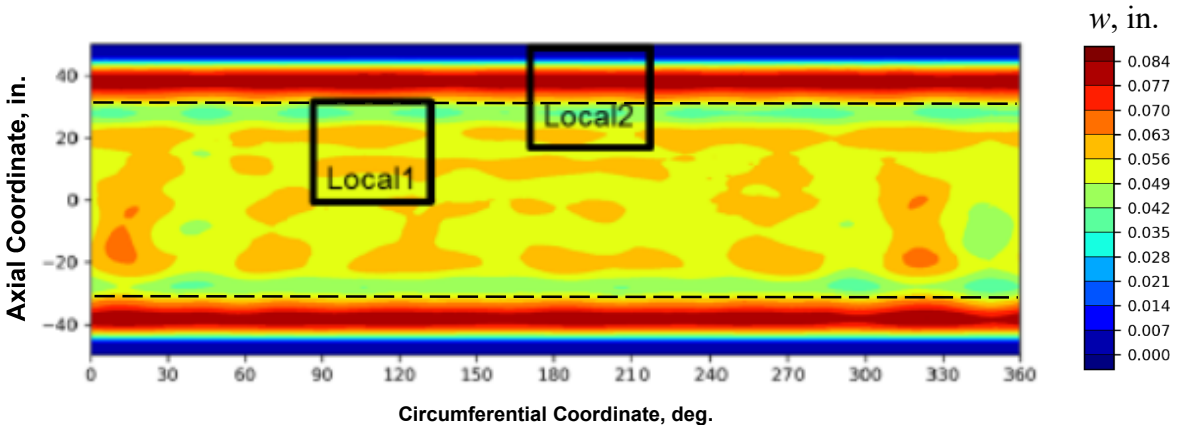

Figure 44. Locations selected for the global-local analyses overlayed on the radial displacement results.

The global-local analysis was accomplished by applying what is referred to in the Abaqus documentation [8] as the node-based submodeling technique. In the submodeling technique, the local region is assumed not to have a major or driving influence on the overall global solution. The practical implication of this limitation for the problem at hand was that the limiting assumption of the technique would be violated if the analysis was extended to the incipient buckling or the postbuckled response, especially if the buckling event originated in the local spatial domain of the model. The local model was constructed using solid elements (C3D8R) to model the core in a homogenized fashion, and continuum shell elements (SC8R) to model the facesheets in both the acreage and padup sections, as shown in Figure 45. The displacements from the global shell FEA obtained along the boundaries of the local model constituted the continuity of the two models. More specifically, the driven (enforced) DoF in the local model was chosen automatically by Abaqus based on the distance between the driven solid-element node and the midsurface of the shell. If the distance was less than 10% of the maximum shell thickness, all displacement components were driven. For the nodes outside the 10% threshold, only the displacement components parallel to the shell midsurface were driven. In other words, the solid-element nodes outside the 10% thickness threshold were not driven in the direction perpendicular to the surface of the shell. The amount of work performed by the interface nodes of the global domain and by the interface nodes of the local domain was computed and compared for a sandwich cylinder very similar to CTA8.2 (designated as CTA8.2B and fabricated after the CTA8.2 test) to assess the goodness of the interaction of the global and local domains. Only small differences were found

and are documented in Reference 7. Another check of the global-local model involved comparing the displacement response to the one obtained from the shell model. The result of this comparison was favorable and is not shown here for brevity.

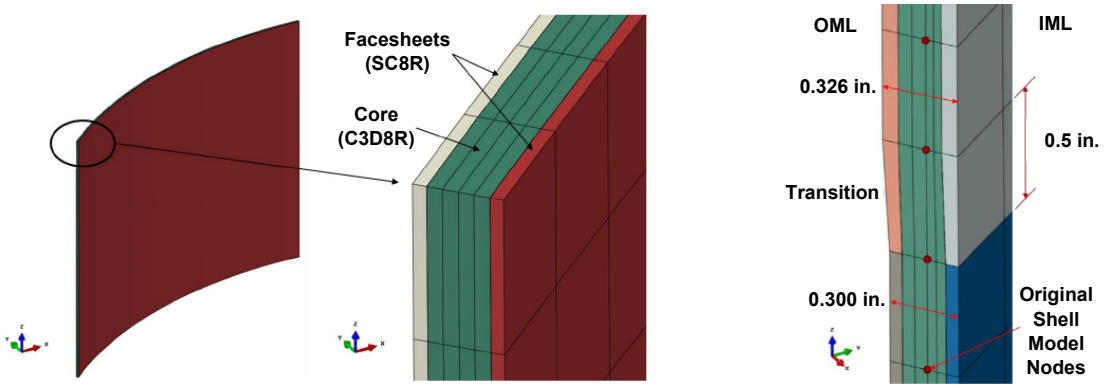

a) General sandwich cross-section. b) Ply drop-off.

Figure 45. Details of the local models.

A geometrically nonlinear implicit solver was used to obtain global-local solutions. In general, the approach undertaken to develop the local models permitted modeling of both radial and core thickness imperfections. However, in the results presented, only the radial imperfections were included. The normal (crush) and transverse shear stress results obtained in the local domain of the imperfect global-local model at incipient failure (708 kips) are shown in Figure 46 for domain Local 1, and in Figure 47 for domain Local 2. As annotated in Figure 46, the spatial domain of Local 1 model included a geometric imperfection originating from the tooling weld line, as seen in Figure 3. As annotated in Figure 47, the spatial domain of Local 2 included termination of all the padup plies and the proximity of the metallic attachment ring. By examining the minima and maxima core stresses, it was concluded that the manufacturing radial imperfection can increase the core stress levels when compared to more pristine sections of the structure. This observation was especially applicable to the core shear stress component, as shown in Figure 46(b), while the rise in the normal stress component was far more moderate, as shown in Figure 46(a). However, by examining the results shown in Figure 47(b), it was observed that the transverse shear stress levels in the proximity of the attachment ring were larger than those resulting from the manufacturing imperfection. While increased normal and shear core stresses were observed in the padup termination area, these results were considered likely overestimated, similar to those from the axisymmetric analysis. Nevertheless, it was also observed that an extended ply drop transition area in the local model (0.5 in. as shown in Figure 45(b), compared to 0.028 in. in Figure 48) reduced the core stress spikes relative to those obtained from the axisymmetric analysis. Overall, the global-local analysis confirmed that the metallic attachment ring installation effect was the primary driver of the core response, and the manufacturing radial imperfections had a significantly lesser impact on the core response. This effectively yielded an important conclusion: despite the pristine geometry limitation in the axisymmetric modeling, the axisymmetric analysis should be adequate for evaluation of the most critical honeycomb core normal and shear stresses, even under the presence of typical manufacturing imperfections.

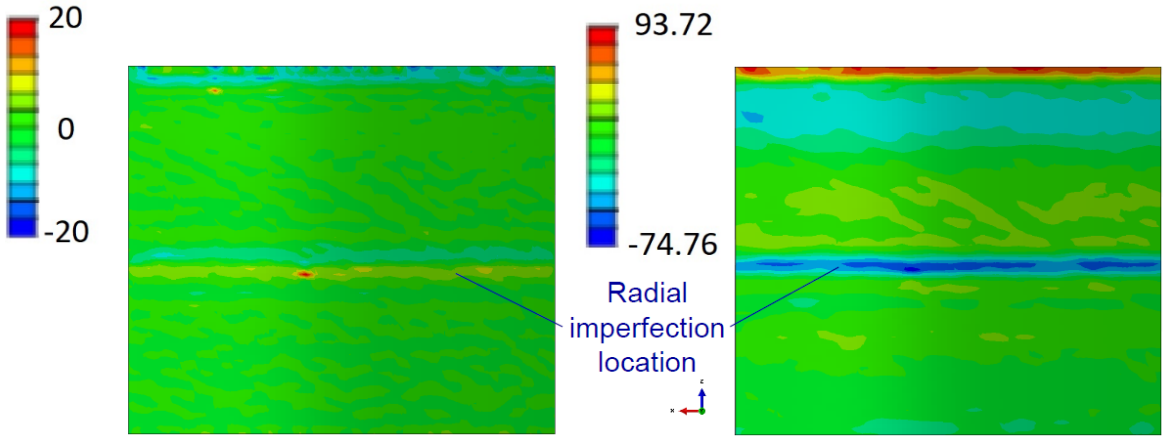

a) Normal stress (psi). b) Shear stress (psi).

Figure 46. Core response at location 1 in the axial direction.

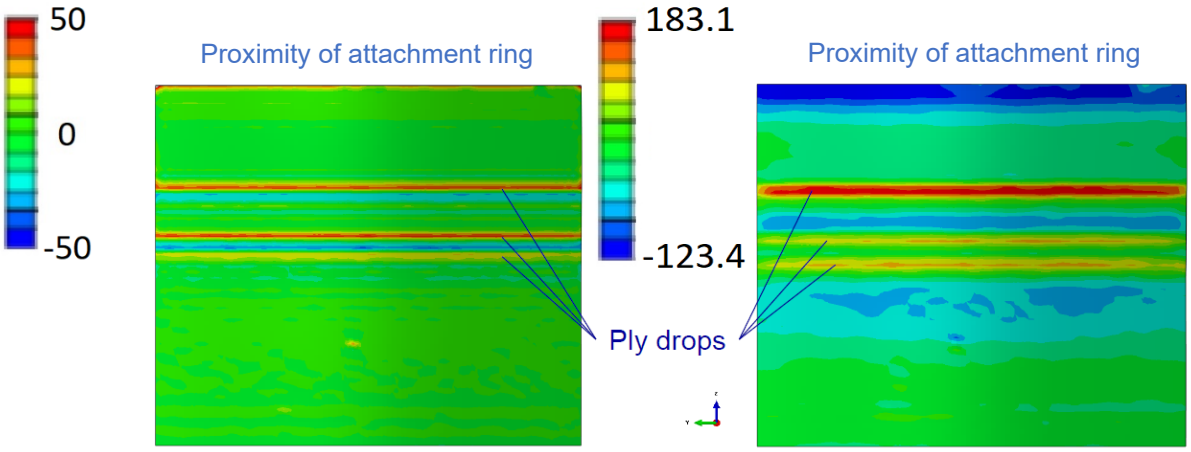

a) Normal stress (psi). b) Shear stress (psi).

Figure 47. Core response at location 2 in the axial direction.

Facesheet strains obtained from the local partitions of the global-local models were also compared with the corresponding results obtained from the shell element model. No substantive differences in the responses were noted (the comparison is not shown here for brevity, but is discussed in Reference 7 for a similar composite sandwich cylinder). Therefore, another benefit of conducting the global-local analysis was the conclusion that no meaningful analysis fidelity loss occurs as a result of the application of the layered shell elements relative to the more complex modeling involving discretization of the honeycomb core with solid elements and discretization of facesheets with continuous shell elements.

4.3 Global Finite Element Analysis with As-Installed Imperfections

Since the global FEA pretest predictions did not capture the essential characteristic of the radial displacement response, it was suspected that the as-manufactured imperfections used in the analysis did not represent all the important conditions of the test article before testing. Several features of the test article were considered and examined as possibly influencing the response; e.g., the core splice pattern, the spacing of the bolt holes in the attachment rings, and the number and periodicity of the load actuators in the test stand. However, none of those factors alone

appeared to be a main driving factor for the differences in the radial displacement response. During the posttest examination it was recognized, however, that the most complete state of the initial geometric imperfection exists when the test article is installed in the test fixture immediately preceding a test. This observation yielded two additional geometric imperfection shapes of interest, other than the as-manufactured imperfections measured after the installation of the attachment rings shown in Figure 3. These imperfections were based on the DIC data captured during the initial part of the final test to failure, test sequence LS8. The midsurface radial deformations shown in Figure 48(a) correspond to the condition when the applied actuator loads are zero so that the full weight of the upper loading structure is compressing the test article, and are called the pre-tare imperfections. The midsurface radial deformations shown in Figure 48(b) correspond to the tare test load, i.e., when the applied actuator loads are such that they effectively remove the weight of the upper loading structure, and are called the at-tare imperfections. One item of note is that the two radial displacements shown in Figure 48 are very similar in pattern and magnitude, but quite distinct from that in Figure 3. More specifically, the skewess (departure from the axial alignment) of the radial deformation patterns is recognizable in Figure 48 while not in Figure 3.

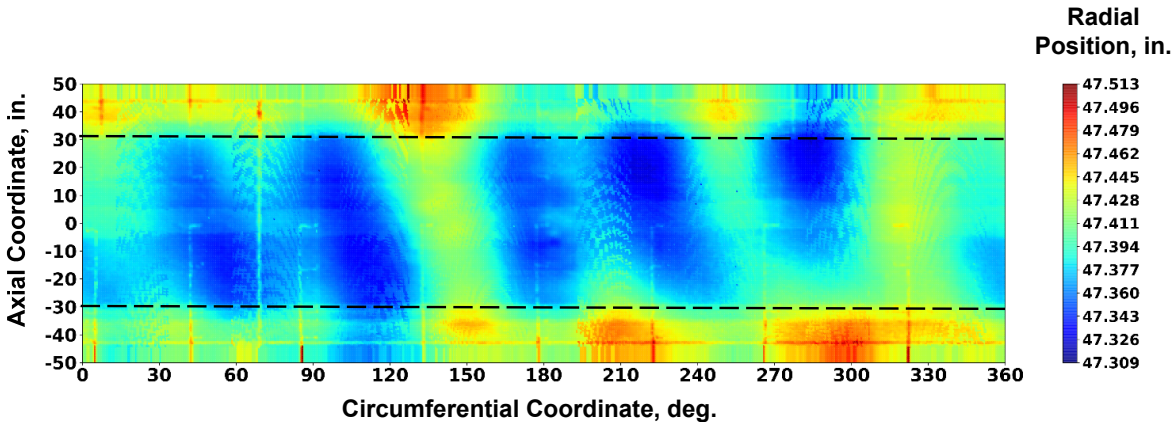

a) Pre-tare load.

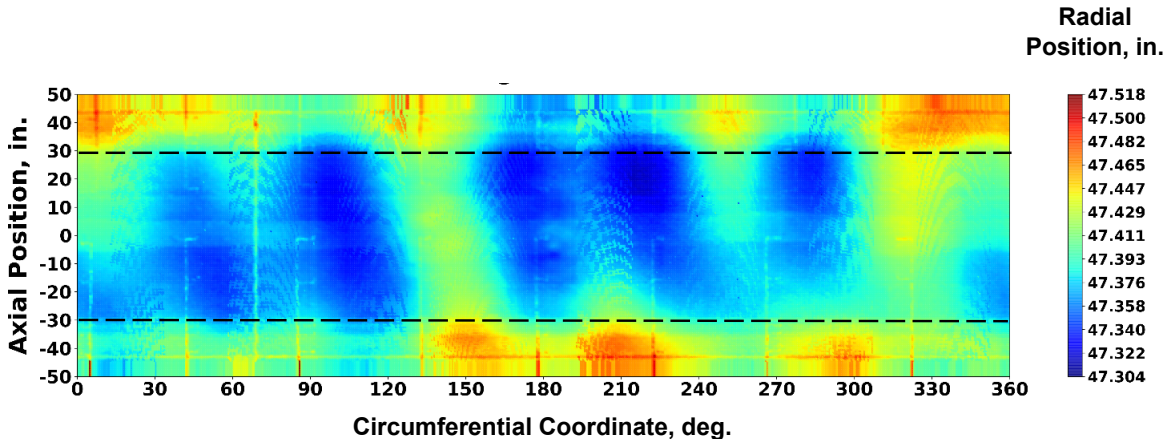

b) At-tare load.

Figure 48. Radial midsurface positions during load sequence LS8.

Nonlinear analyses with the two radial imperfections presented in Figure 48 and the thickness imperfection of Figure 4 were performed. The two analyses yielded nearly identical results as assessed by examining the load versus end-shortening curves and by examining the radial

deformations. In the absence of meaningful differences between the two analysis results with the as-installed imperfections, the remainder of this section presents only the results obtained with the radial imperfection obtained under zero actuator load or pre-tare, i.e., as shown in Figure 48(a). This analysis is referred to herein as the *as-installed imperfection* analysis.

A nonlinear buckling load of 814 kips was obtained from the analysis with the pre-tare as-installed imperfection, compared to 864 kips predicted with the as-manufactured imperfections, which is a 6% reduction. The load versus end-shortening curves for the analysis with the pre-tare as-installed imperfection and for the test are shown in Figure 49. The lower buckling load and reduced load versus end-shortening slope obtained with the as-installed imperfection model, as compared to the as-manufactured imperfection results (shown in Figure 21), can be explained by examining the maximum amplitude of radial imperfections. The posttest predictions using the as-manufactured radial imperfection (shown in Figure 4) had the maximum amplitude of approximately 0.11 in. and the corresponding amplitude of the as-installed imperfection (shown in Figure 48(a)) was approximately 0.20 in.

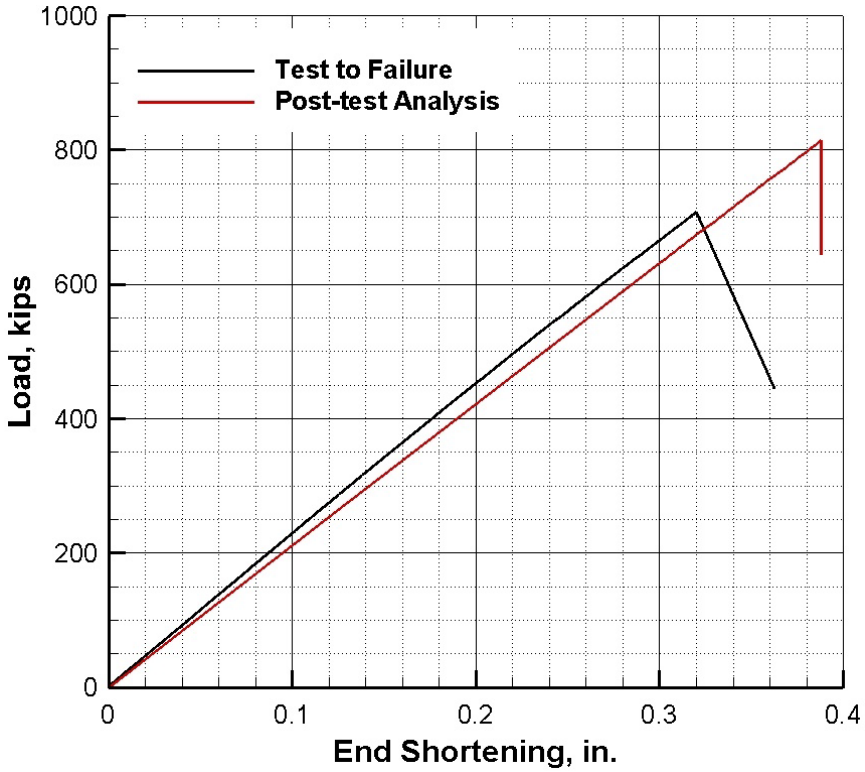

Figure 49. Load versus end-shortening – test versus posttest analysis.

Axial and radial displacements and axial and hoop strains obtained with the as-installed imperfections are presented next for the two load levels discussed in section 3.2, i.e., subcritical regime/last LS8 hold of 643 kips (Figure 50 through 53) and the incipient failure of 708 kips (Figure 54 through 57). The test results presented in section 3.2 are not reproduced in this section for brevity but the analysis results in Figure 50 through 53 are to be compared with the top images in Figure 30 through 33, and Figure 54 through 57 compared with the top images in Figure 34 through 37.

The axial displacement agreement between test and pretest predictions obtained with the as-manufactured imperfection was good, and this favorable comparison was maintained in the

posttest analysis with the as-installed imperfections. The as-installed imperfection analysis results for axial displacement (Figure 50 and Figure 54) still exhibited a more regular axisymmetric pattern when compared to test data (top images in Figure 30 and Figure 34, respectively). The radial displacement results, however, show a much-improved comparison. The six distinct radial patterns leaning away from the axial direction are clearly identified in Figure 51 and Figure 55, and correspond closely to those shown in top images in Figure 31 and Figure 35. Variations in the amplitudes of the six undulations around the circumference are also properly captured. In Figure 51 and Figure 55, the third radial pattern from the left (with its root at circumferential coordinate of approximately 150 degree) has the smallest amplitude, and the first deformation from the right (with its root at circumferential coordinate of approximately 330 degree) is most pronounced. The amplitudes overall compare favorably and mimic the test results by producing maximum values in the padup areas.

The quality of axial strain agreement between test and analysis, while not perfect, is also improved when the analysis results obtained with the as-installed imperfections are considered. Most of the improvement is attributable to more realistic strain variability in the new predictions, which is likely a consequence of the improved radial displacement agreement. The axial strain pretest predictions obtained with the as-manufactured imperfection showed very minimal strain variations in the acreage area when compared to the test results, as shown in Figure 32 and Figure 36. The posttest analysis with the as-installed imperfections clearly shows more axial strain variability in the acreage. While the strain pattern is not exactly matched, the strains obtained from the analysis with the as-installed imperfections are mostly bounded by the measured strain range from the test. This pattern is perceived as an improvement when compared to the pretest analysis with the as-manufactured imperfections. A similar observation, however to a lesser extent, can be made with regard to the hoop strain comparisons: while the test strain scatter, as seen in top images of Figure 33 and Figure 37, is still more pronounced than that obtained from the analysis with the as-installed imperfections (Figure 53 and Figure 57, respectively), there is even less variability within the pretest predictions obtained with the as-manufactured imperfection (bottom images in Figure 33 and Figure 37, respectively).

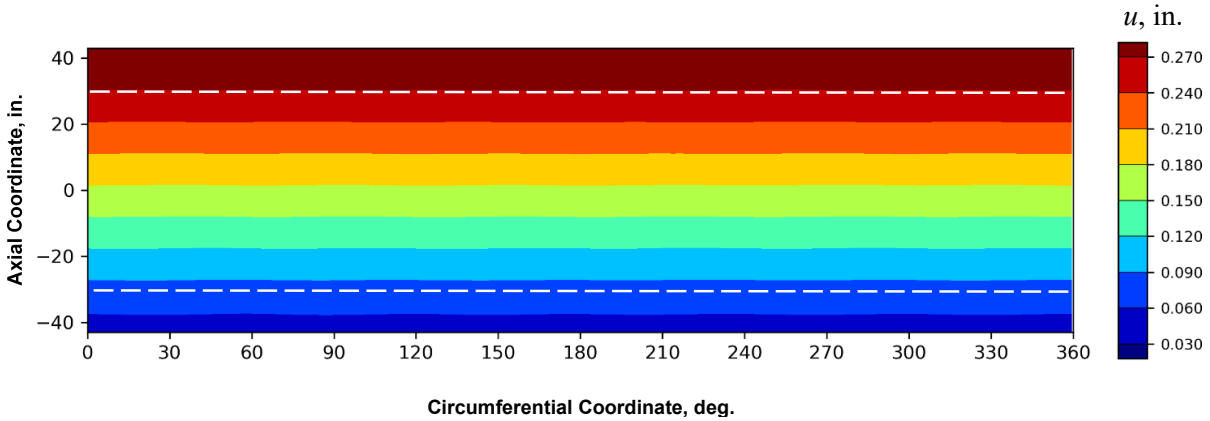

Figure 50. Axial displacement at 643 kips from FEA with as-installed imperfections.

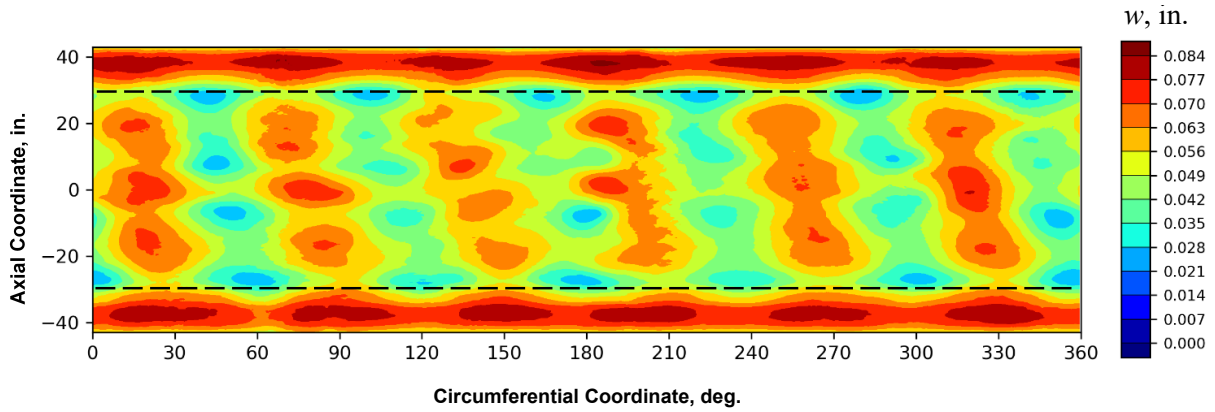

Figure 51. Radial displacement at 643 kips from FEA with as-installed imperfections.

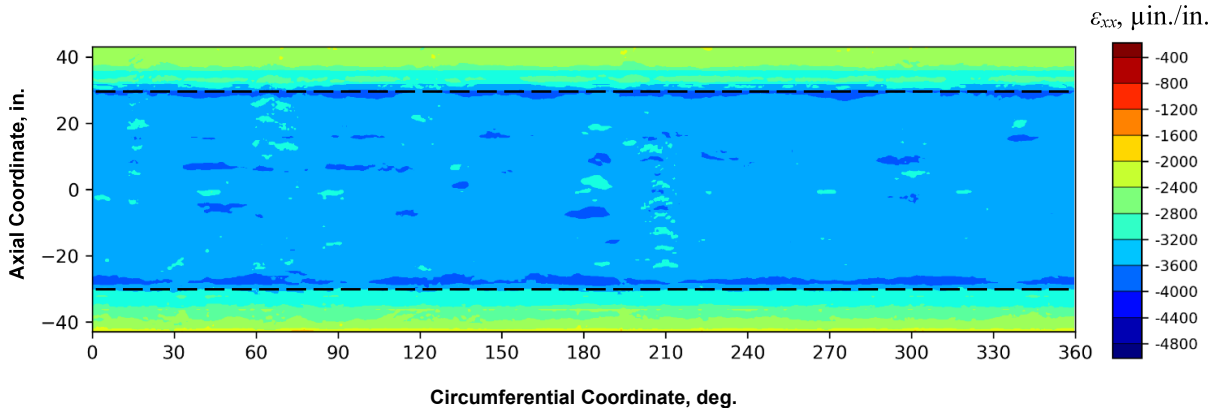

Figure 52. Axial strain at 643 kips from FEA with as-installed imperfections.

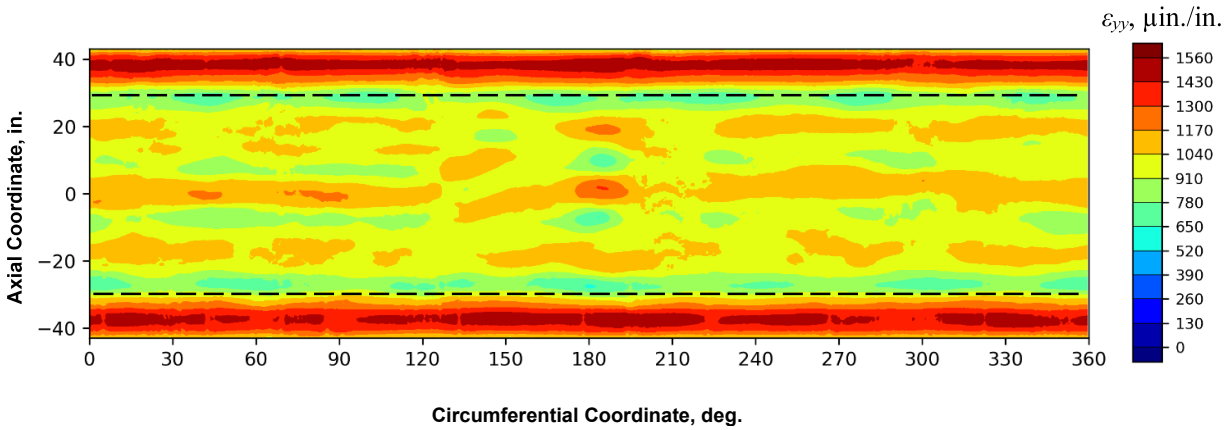

Figure 53. Hoop strain at 643 kips from FEA with as-installed imperfections.

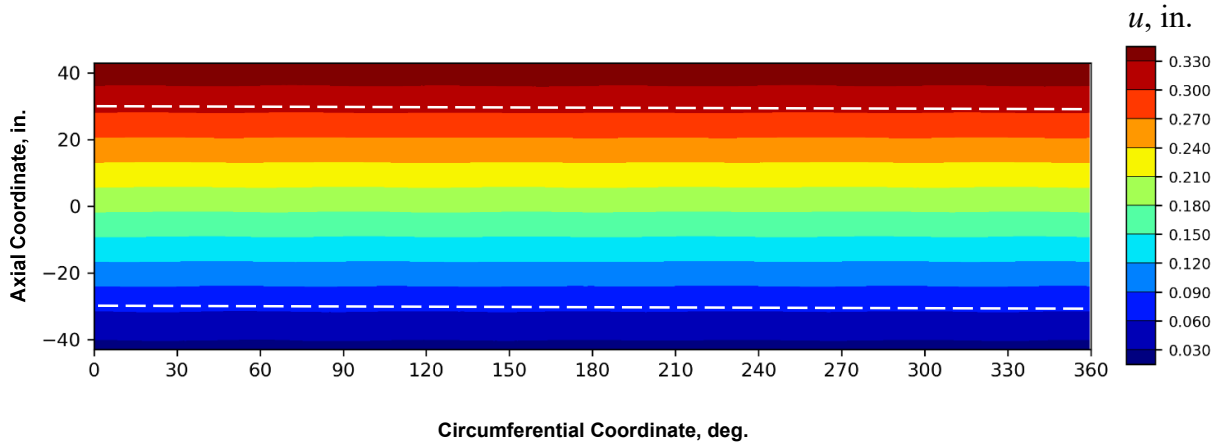

Figure 54. Axial displacement at 708 kips from FEA with as-installed imperfections.

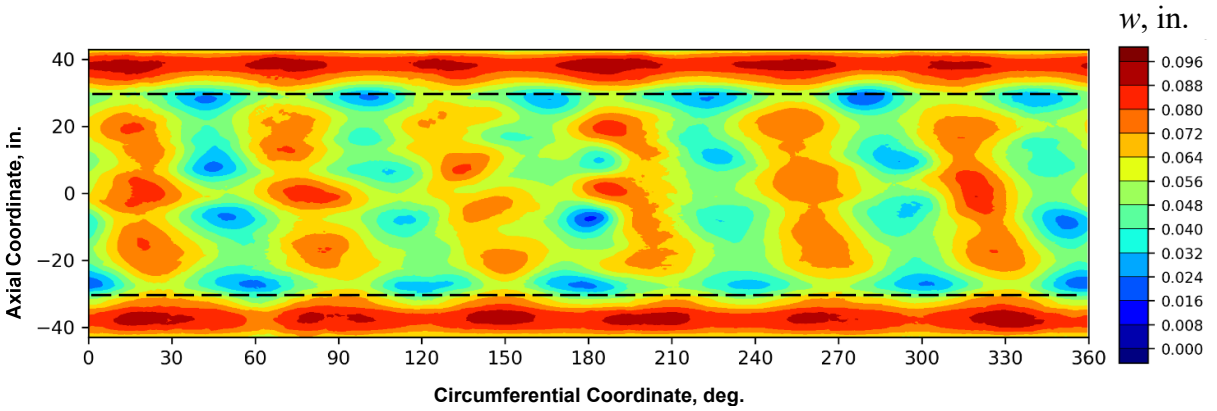

Figure 55. Radial displacement at 708 kips from FEA with as-installed imperfections.

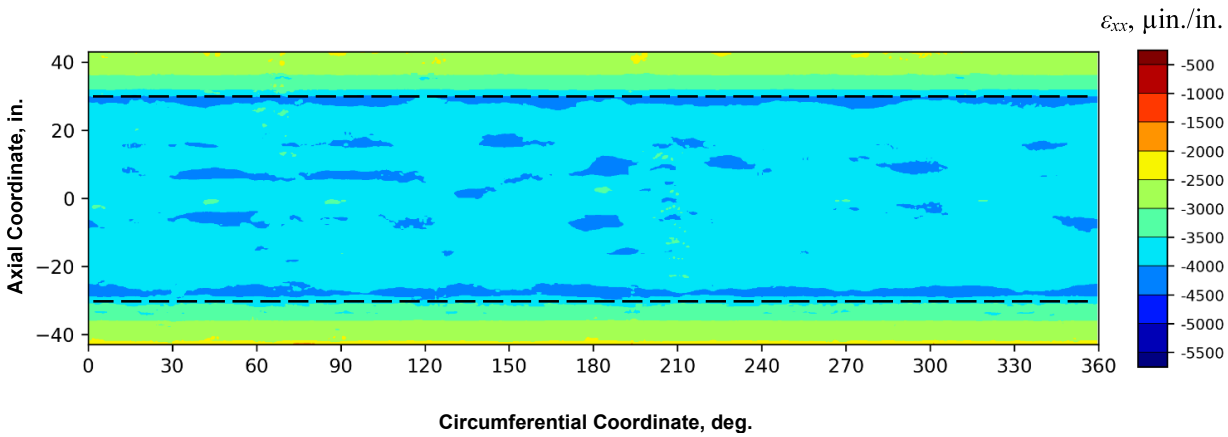

Figure 56. Axial strain at 708 kips from FEA with as-installed imperfections.

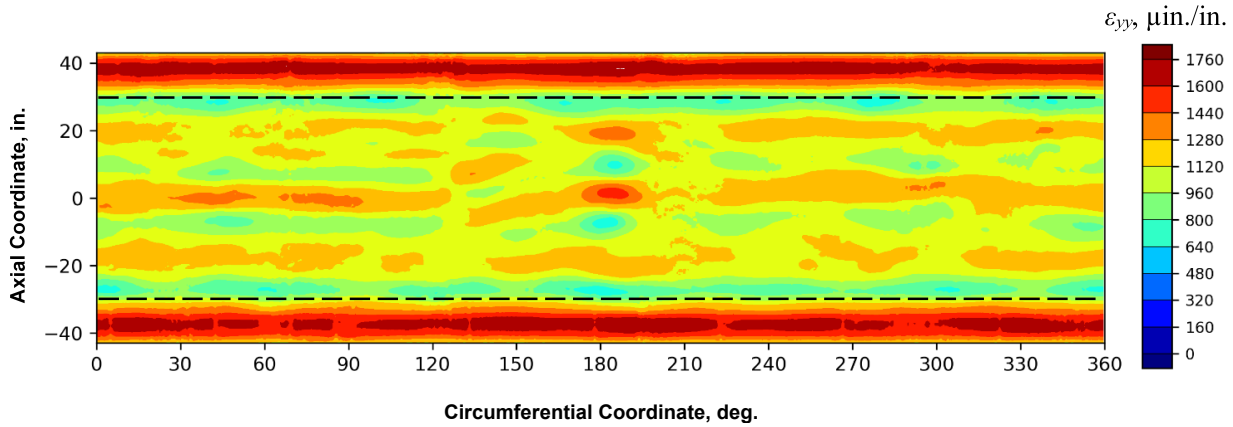

Figure 57. Hoop strain at 708 kips from FEA with as-installed imperfections.

A comparison of strains at discrete locations on the OML and IML surfaces is presented next. All results were obtained at the incipient failure from the test (708 kips), and the test data were obtained from the conventional strain gages affixed to the test article as shown in Figure A5 of Appendix A. For both the axial and hoop strain components, the measurements were taken and are compared at every 45 degrees along the circumferential coordinate. Selected acreage area axial strains are compared in Figure 58 at the midlength (or 0-in. axial coordinate) locations and in Figure 59 at the ±14.5-in. axial coordinates. Selected padup axial strains are compared in Figure 60 at the ±40-in. axial coordinate. Hoop strain measurements in the acreage area were only available at the midlength (or 0-in. axial coordinate) locations and are compared in Figure 61. Hoop strain measurements in the padup area were available at the ±40-in. axial coordinates and are compared in Figure 62.

Overall fair to good agreement is observed when examining axial strains. Test and analysis values at the midlength of the cylinder, Figure 58, do not match exactly, but to a large extent capture the fluctuation characteristics around the circumference. A favorable comparison is also observed at the ±14.5-in. axial coordinate, Figure 59, with the better agreement on the OML than on the IML where the analysis overpredicted the axial strain magnitudes. Similar axial strain magnitude overestimation by analysis, but on the OML side, is also noted in the padup area near the attachment ring, Figure 60. While the IML test results shown in Figure 60 are characterized by more scattered distribution when compared to the OML side, the analysis results on the IML side do not show a clear bias for under- or over-estimation of the test results. Averaged errors were computed using all 16 strains (eight OML and eight IML values) for each axial location shown in Figure 58 through 60. The largest average error of 14.4% was obtained at the +40-in. location, and the lowest error of 5.9% at the 0 in. location. Given that the gradients of radial displacement, and consequently axial strains, were generally larger at the ends of test article (in the padup areas) when compared to the acreage, the better agreement in the section of the test article with smaller result gradient is not surprising and quite intuitive.

Generally, small differences in the radial displacements between test results and predictions can attribute to more pronounced strain discrepancies. While the membrane axial strain component (i.e., the average of OML and IML strains) of a uniformly compressed cylinder does not vary significantly, the axial bending strain component (i.e., OML or IML strain after the membrane component is subtracted) is more sensitive to a specific radial displacement response pattern. In

other words, what appears to be a minor radial displacement pattern mismatch on full-field plots can result in a more substantive strain mismatch.

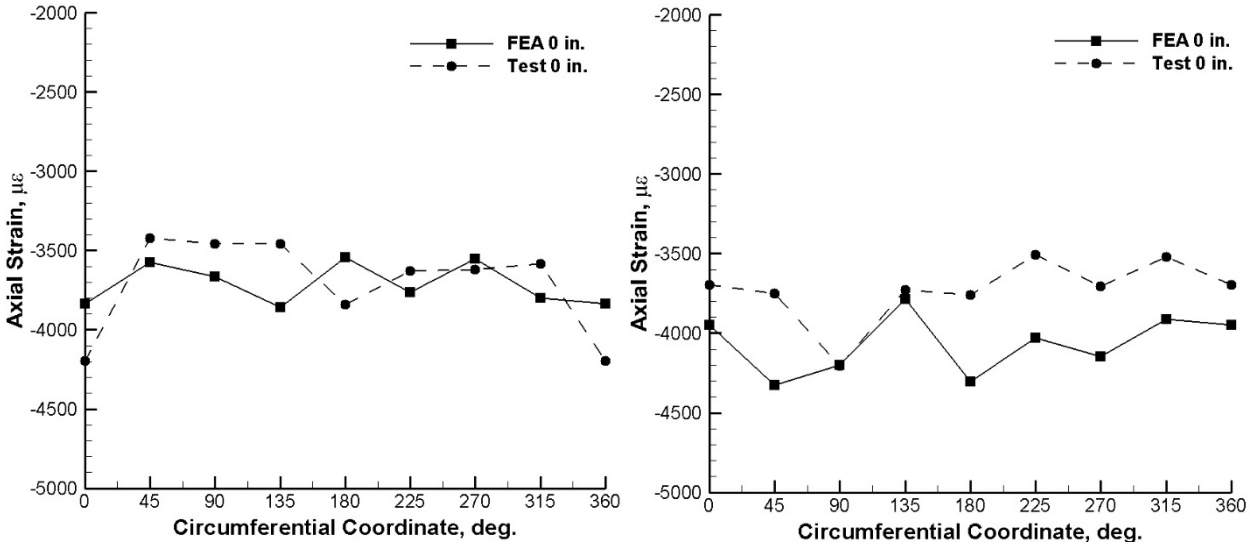

a) OML. b) IML.

Figure 58. FEA with as-installed imperfections and test axial strains at midlength of the test article.

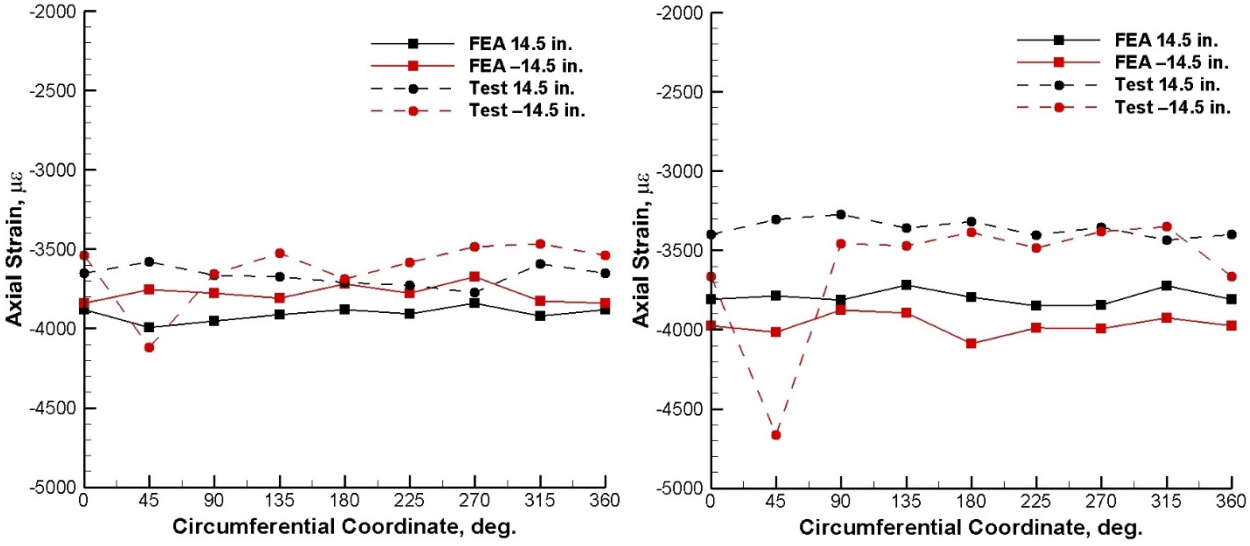

a) OML. b) IML.

Figure 59. FEA with as-installed imperfections and test axial strains at ±14.5-in. height of the test article.

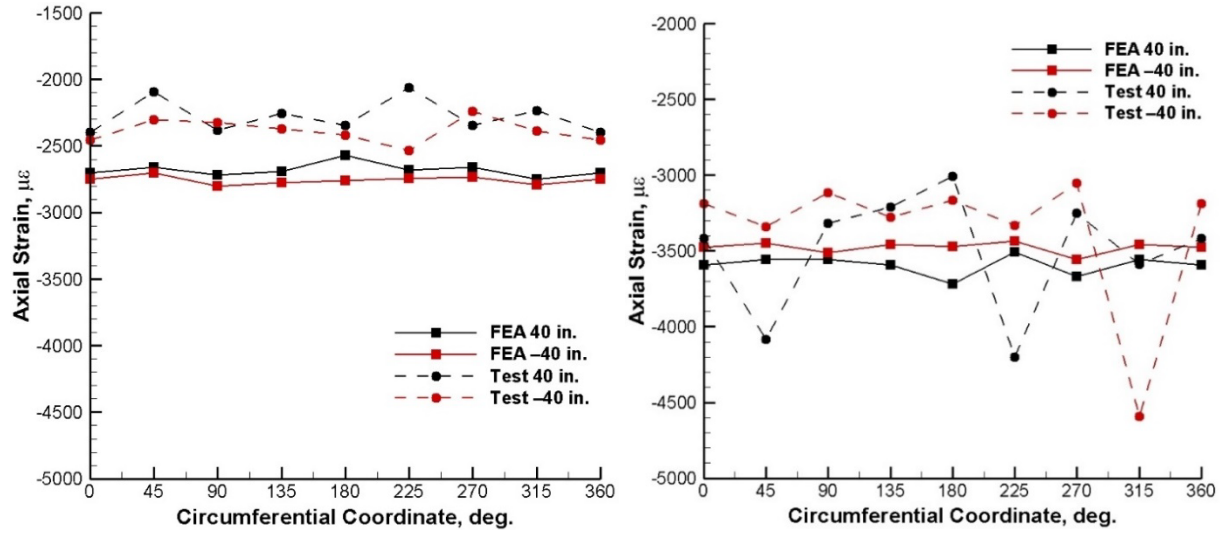

a) OML. b) IML.

Figure 60. FEA with as-installed imperfections and test axial strains at ±40-in. height of the test article.

Elements of acceptable agreement are observed when examining hoop strains at the midlength location, Figure 61. While test and analysis values do not match exactly (an average error of 25.9% when eight OML and eight IML data points are considered), the strain fluctuation trends around the circumference were well captured by the analysis. The comparison is less favorable at the padup locations shown in Figure 62. The predicted hoop strains are consistently larger on both the OML and IML sides (average error of 32.0% at 40 in. and 29.3% at –40 in.). Since the transverse displacement gradients are large in the padup area, small differences in the transverse displacement profiles can translate into large hoop strain differences. Also, as previously discussed, the pre-existing core damage in the proximity of the attachment rings can be one of the factors that has a potential to alter the transverse displacement profile and propagate to the strain results in a manner similar to the one seen in Figure 62.

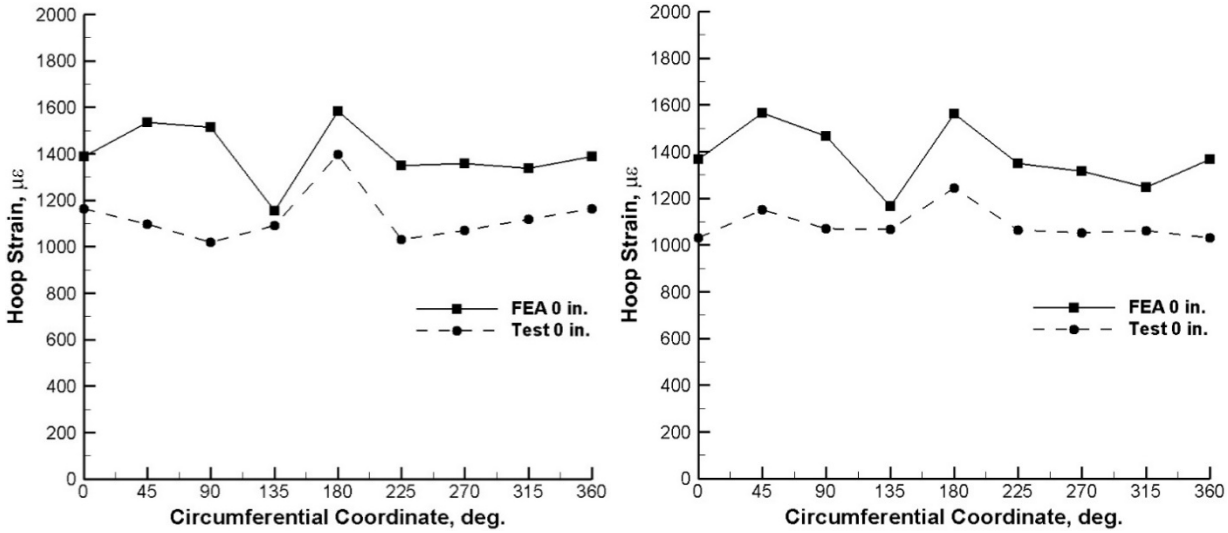

a) OML. b) IML.

Figure 61. FEA with as-installed imperfections and test hoop strains at midlength of the test article.

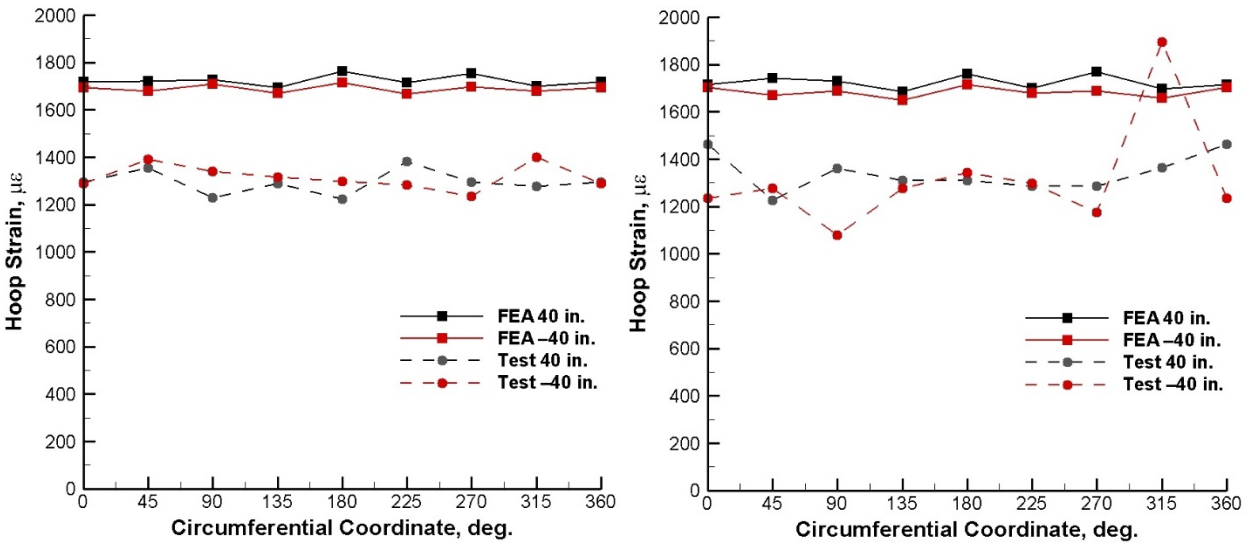

a) OML. b) IML.

Figure 62. FEA with as-installed imperfections and test hoop strains at ±40 in. of the test article.

For the strain results obtained in the padup locations (Figure 60 for the axial component and Figure 62 for the hoop component), something of note is also the limitation of the padup ply drop modeling in a global shell element-based model. Effectively, a padup ply termination occurs as a thickness step function (and consequently as the neutral bending axis location step function change), whereas in an as-built cylinder this transition is far more gradual.

5.0 Concluding Remarks

The composite test article CTA8.2 was manufactured and a nondestructive evaluation of its sandwich wall was performed without adverse findings before potting into the attachment rings. Geometric imperfections were captured after the test article was potted in the attachment rings, but before it was installed in the test stand. This measurement defined the as-manufactured imperfections. A predictive analysis using closed-form solutions and a shell-element-based FEM was performed before testing. The latter included representation of the radial and thickness as-manufactured imperfections. A test plan was devised based on the predictive analysis and the test article was instrumented according to this plan.

After installing the test article in the test facility, a sequence of tests began. Subcritical load sequences were exercised uneventfully, and acceptable agreement between test results and predictions was observed while conducting these tests. The test article, however, failed prematurely and in an unanticipated failure mode during the final load sequence to failure. Analysis of the test data indicated that failure initialization occurred in the FWD padup area in the direct proximity of the attachment ring. Crush and transverse shear damage were evident after sectioning both FWD and AFT padup regions of the failed test article. Additional review of the structured-light scan geometry data that were taken before testing, combined with the visual inspection of the remains of the test article, demonstrated significant thickness variations that would be indicative of preexisting damage in the core sections near both the FWD and AFT attachment rings. This preexisting damage origination was traced back to the excessive torque specified for the safety bolts installed through the end sections of the test article and the aluminum attachment rings. It was acknowledged that the torque specification was carried over from the

previous assembly procedures intended for metallic test articles that could tolerate much larger through-the-thickness compression and that used stiffer steel attachment rings. Since the subject bolts were not in the primary load path, but merely served as a post-failure safety feature, there existed no rationale for torqueing the bolts as prescribed in the assembly procedure. A "finger-tight" installation of the safety bolts was recommended and successfully applied in subsequent tests of other similar sandwich cylinders.

Since no core crush and transverse shear evaluation was performed as part of the pretest analysis, additional analyses targeting such an assessment were conducted. An axisymmetric analysis was devised and exercised with several variations of interactions between the sandwich cylinder wall, potting grout, and the attachment ring. While the sliding interaction, considered as the nominal behavior, resulted in a marginally positive safety factor, all other off-nominal variations that could potentially result from imperfect installation resulted in negative margins. The axisymmetric analyses assumed nominal core properties; i.e., they did not account for a strongly suspected preexisting core damage. Furthermore, the homogenized modeling of the core did not account for interactions between crushing and transverse shear.

Considering that the axisymmetric modeling was unable to capture the realistic geometric imperfections of the as-manufactured cylinder, additional verification that such imperfections do not significantly affect core response was warranted. This objective was accomplished using global-local modeling, where the local parts of the model were collocated with what was perceived as features potentially detrimental to the core behavior. The global-local study yielded a conclusion that typical geometric as-manufactured imperfections are not a strong driver of the core response, and the axisymmetric modeling of a perfect sandwich cylinder should be adequate for the core response evaluation.

The FEA results using a set of as-installed imperfections compared far more favorably with the test data relative to the analysis results obtained with the as-manufactured imperfections. It was concluded that the as-manufactured imperfection was only a component of the total geometric imperfection, with the installation-induced component still missing. The lesson learned based on this observation is to not assume what the main factors are driving the overall geometric imperfection. It is prudent to consider all possible sources of imperfections, and to not introduce simplifying assumptions without verifying them.

Lessons learned from the CTA8.2 design, testing, and pretest and posttest analysis framework became a foundation for an enhanced design procedure for this class of structures [6]. This procedure was successfully applied to two additional test article designs that were manufactured and tested subsequent to CTA8.2, namely CTA8.2B [13] and CTA 8.3 [14]. While CTA8.3 had a distinct sandwich wall architecture, the CTA8.2B article very closely resembled the CTA8.2 design: stronger/higher density core spliced at the ends of the cylinder and more evenly spaced padup ply drop offs were the only two meaningful design modifications relative to CTA8.2.

6.0 References

1. Hilburger, M. W. (editor): *Buckling of thin wall circular cylinders*, NASA/SP-8007-2020/ REV2, NASA Langley Research Center, Hampton, VA, December 2020.
2. Schultz, M. R.; and Przekop, A.: *SBKF-P3-CYL-CTA8.2 Test Plan*, NASA Langley Research Center, Hampton, VA, December 2, 2017.

3. Day, L.: *Test and Checkout Procedure: Shell Buckling Knockdown Factor Test #11 CTA8.2*, SST-TCP-FP17.1, NASA Marshall Space Flight Center, Huntsville, AL, December 4, 2017.
4. Lovejoy, A. E.; and Hilburger, M., W.: *Design of 8-ft-Diameter Barrel Test Article Attachment Rings for Shell Buckling Knockdown Factor Project*, NASA/TM–2010-216839, NASA Langley Research Center, Hampton, VA, August 2010.
5. Kosztowny, C. J. R.: "Implementing Geometric Surface Imperfections into Sandwich Composite Cylinder Finite Element Method Models," AIAA-2021-0439, *The 2021 AIAA SciTech Forum*, doi: 10.2514/6.2021-0439, Virtual Event, 2021.
6. https://www.micorco.com/wp-content/uploads/2014/03/Micorox-Standard-Grout-PDF-3-2014.pdf, retrieved August 26, 2021.
7. Przekop, A.; Schultz, M. R.; Kosztowny, C. J.; Song, K.; Lindell, M. C.; Hilburger, M. W.; and Rudd, M. T.: *Design and Analysis of Buckling-Critical Large-Scale Sandwich Composite Cylindrical Test Articles*, NASA/TM–20205008667, NASA Langley Research Center, Hampton, VA, November 2020.
8. Abaqus/Standard, Software Package, Ver. 6.14-1, SIMULIA, Providence, RI, 2014.
9. Opliger, M.: SBKF testing results, electronic delivery, National Institute for Aviation Research, Wichita, KS.
10. Reeder, J. R.: "Property Values for Preliminary Design of the Ares I Composite Interstage," NASA internal memo to the Marshall Space Flight Center, NASA Langley Research Center, Hampton, VA, March 2007.
11. Anonymous: "HexWeb Honeycomb Attributes and Properties," *Hexcel Composites*, TSB 120, Pleasanton, CA, November 1999.
12. Schultz, M. R.; Sleight, D. W.; Gardner, R. W.; Rudd, M. T.; Hilburger, M. W.; Palm, T. E.; and Oldfield, N. J.: Test and Analysis of a Buckling-Critical Large-Scale Sandwich Composite Cylinder, *The 2018 AIAA SciTech Forum*, Kissimmee, FL, AIAA-2018-1693, doi: 10.2514/6.2018-1693, 2018.
13. Kosztowny, C. J.; Song, K.; Schultz, M. R.; Gardner, N. W.; Przekop, A.; and Rudd, M. T.: *Test and Analysis of the 8-foot Diameter Cylindrical Sandwich Composite Test Article CTA8.2B*, NASA/TM–20210024081, Hampton, VA, 2021.
14. Song, K.; Schultz, M. R.; Kosztowny, C. J.; Przekop, A.; Gardner, N. W.; and Rudd, M. T.: *Buckling Test and Analysis of the 8-foot-diameter Sandwich Composite Cylinder Test Article CTA8.3 as Part of the Shell Buckling Knockdown Factor Project: Test Dates 16-19 December 2019*, NASA/TM–20210024768, Hampton, VA, 2021.

Appendix A – Drawings of the Test Article

Appendix A contains technical drawings of the test article, including: fabrication (Figure A1), trim (Figure A2), aluminum attachment rings (Figure A3), assembly (Figure A4), and instrumentation (Figures A5 and A6).

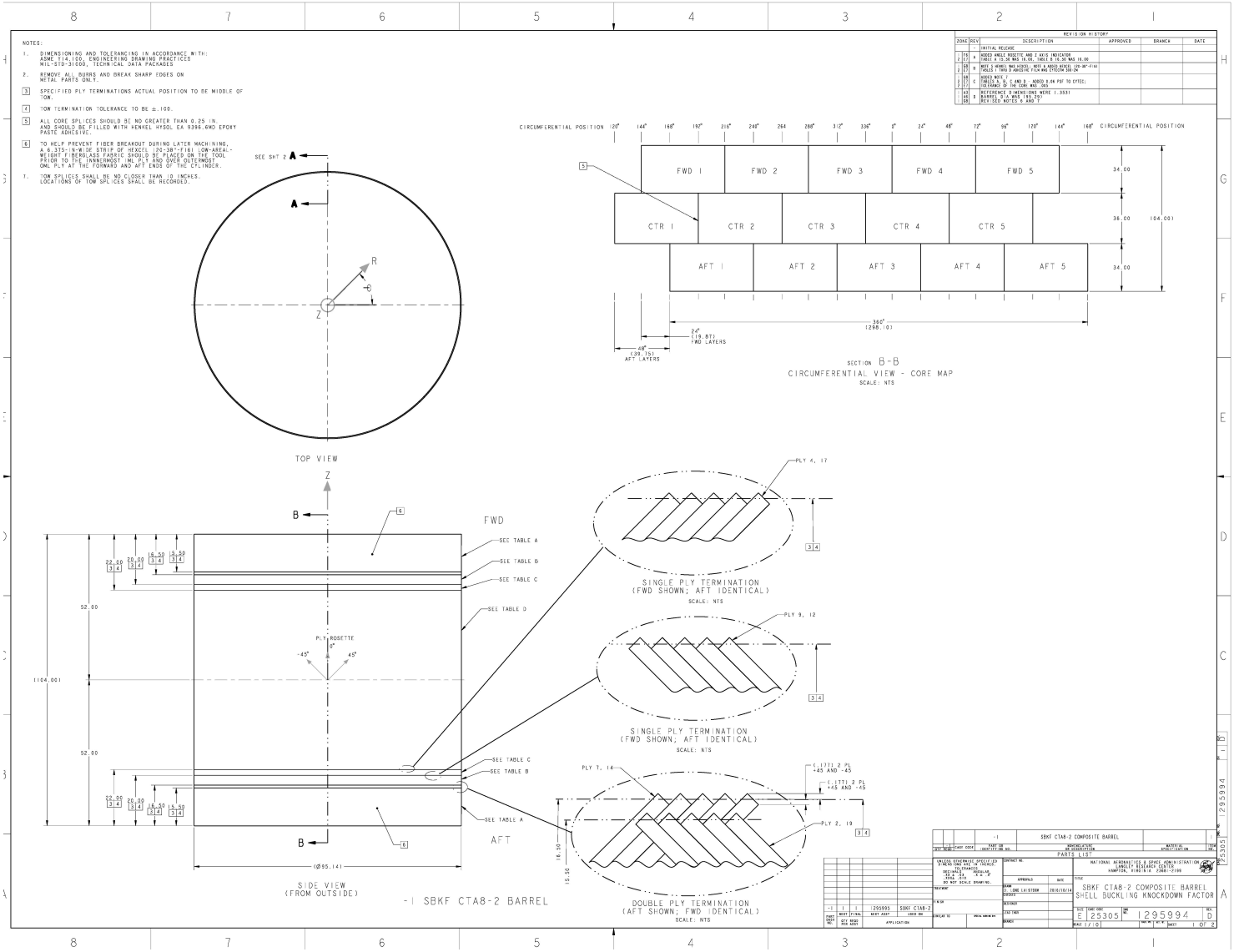

Figure A1. CTA8.2 fabrication drawing showing the design, LaRC drawing 1295994 Rev. D.

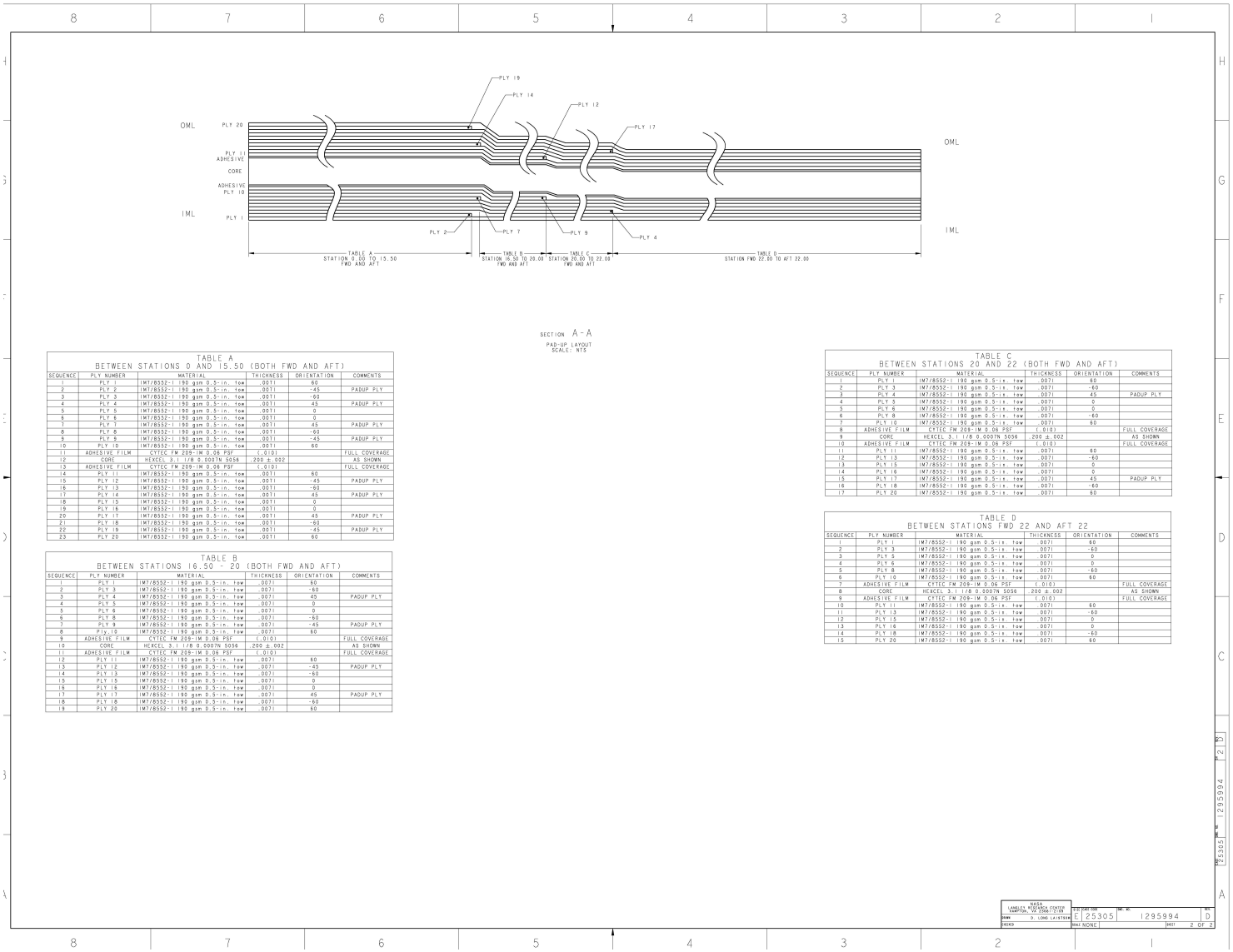

TABLE A
BETWEEN STATIONS 0 AND 15.50 (BOTH FWD AND AFT)

SEQUENCE	PLY NUMBER	MATERIAL	THICKNESS	ORIENTATION	COMMENTS
1	PLY 1	IM7/8552-1 190 gsm 0.5-in. tow	.007†	60	
2	PLY 2	IM7/8552-1 190 gsm 0.5-in. tow	.007†	-45	PADUP PLY
3	PLY 3	IM7/8552-1 190 gsm 0.5-in. tow	.007†	-60	
4	PLY 4	IM7/8552-1 190 gsm 0.5-in. tow	.007†	45	PADUP PLY
5	PLY 5	IM7/8552-1 190 gsm 0.5-in. tow	.007†	0	
6	PLY 6	IM7/8552-1 190 gsm 0.5-in. tow	.007†	0	
7	PLY 7	IM7/8552-1 190 gsm 0.5-in. tow	.007†	45	PADUP PLY
8	PLY 8	IM7/8552-1 190 gsm 0.5-in. tow	.007†	-60	
9	PLY 9	IM7/8552-1 190 gsm 0.5-in. tow	.007†	-45	PADUP PLY
10	PLY 10	IM7/8552-1 190 gsm 0.5-in. tow	.007†	60	
11	ADHESIVE FILM	CYTEC FM 209-1M 0.06 PSF	(.010)		FULL COVERAGE
12	CORE	HEXCEL 3.1 1/8 0.0007N 5056	.200 ± .002		AS SHOWN
13	ADHESIVE FILM	CYTEC FM 209-1M 0.06 PSF	(.010)		FULL COVERAGE
14	PLY 11	IM7/8552-1 190 gsm 0.5-in. tow	.007†	60	
15	PLY 12	IM7/8552-1 190 gsm 0.5-in. tow	.007†	-45	PADUP PLY
16	PLY 13	IM7/8552-1 190 gsm 0.5-in. tow	.007†	-60	
17	PLY 14	IM7/8552-1 190 gsm 0.5-in. tow	.007†	45	PADUP PLY
18	PLY 15	IM7/8552-1 190 gsm 0.5-in. tow	.007†	0	
19	PLY 16	IM7/8552-1 190 gsm 0.5-in. tow	.007†	0	
20	PLY 17	IM7/8552-1 190 gsm 0.5-in. tow	.007†	45	PADUP PLY
21	PLY 18	IM7/8552-1 190 gsm 0.5-in. tow	.007†	-60	
22	PLY 19	IM7/8552-1 190 gsm 0.5-in. tow	.007†	-45	PADUP PLY
23	PLY 20	IM7/8552-1 190 gsm 0.5-in. tow	.007†	60	

TABLE B
BETWEEN STATIONS 16.50 - 20 (BOTH FWD AND AFT)

SEQUENCE	PLY NUMBER	MATERIAL	THICKNESS	ORIENTATION	COMMENTS
1	PLY 1	IM7/8552-1 190 gsm 0.5-in. tow	.007†	60	
2	PLY 3	IM7/8552-1 190 gsm 0.5-in. tow	.007†	-60	
3	PLY 4	IM7/8552-1 190 gsm 0.5-in. tow	.007†	45	PADUP PLY
4	PLY 5	IM7/8552-1 190 gsm 0.5-in. tow	.007†	0	
5	PLY 6	IM7/8552-1 190 gsm 0.5-in. tow	.007†	0	
6	PLY 8	IM7/8552-1 190 gsm 0.5-in. tow	.007†	-60	
7	PLY 9	IM7/8552-1 190 gsm 0.5-in. tow	.007†	-45	PADUP PLY
8	Ply.10	IM7/8552-1 190 gsm 0.5-in. tow	.007†	60	
9	ADHESIVE FILM	CYTEC FM 209-1M 0.06 PSF	(.010)		FULL COVERAGE
10	CORE	HEXCEL 3.1 1/8 0.0007N 5056	.200 ± .002		AS SHOWN
11	ADHESIVE FILM	CYTEC FM 209-1M 0.06 PSF	(.010)		FULL COVERAGE
12	PLY 11	IM7/8552-1 190 gsm 0.5-in. tow	.007†	60	
13	PLY 12	IM7/8552-1 190 gsm 0.5-in. tow	.007†	-45	PADUP PLY
14	PLY 13	IM7/8552-1 190 gsm 0.5-in. tow	.007†	-60	
15	PLY 15	IM7/8552-1 190 gsm 0.5-in. tow	.007†	0	
16	PLY 16	IM7/8552-1 190 gsm 0.5-in. tow	.007†	0	
17	PLY 17	IM7/8552-1 190 gsm 0.5-in. tow	.007†	45	PADUP PLY
18	PLY 18	IM7/8552-1 190 gsm 0.5-in. tow	.007†	-60	
19	PLY 20	IM7/8552-1 190 gsm 0.5-in. tow	.007†	60	

TABLE C
BETWEEN STATIONS 20 AND 22 (BOTH FWD AND AFT)

SEQUENCE	PLY NUMBER	MATERIAL	THICKNESS	ORIENTATION	COMMENTS
1	PLY 1	IM7/8552-1 190 gsm 0.5-in. tow	.007†	60	
2	PLY 3	IM7/8552-1 190 gsm 0.5-in. tow	.007†	-60	
3	PLY 4	IM7/8552-1 190 gsm 0.5-in. tow	.007†	45	PADUP PLY
4	PLY 5	IM7/8552-1 190 gsm 0.5-in. tow	.007†	0	
5	PLY 6	IM7/8552-1 190 gsm 0.5-in. tow	.007†	0	
6	PLY 8	IM7/8552-1 190 gsm 0.5-in. tow	.007†	-60	
7	PLY 10	IM7/8552-1 190 gsm 0.5-in. tow	.007†	60	
8	ADHESIVE FILM	CYTEC FM 209-1M 0.06 PSF	(.010)		FULL COVERAGE
9	CORE	HEXCEL 3.1 1/8 0.0007N 5056	.200 ± .002		AS SHOWN
10	ADHESIVE FILM	CYTEC FM 209-1M 0.06 PSF	(.010)		FULL COVERAGE
11	PLY 11	IM7/8552-1 190 gsm 0.5-in. tow	.007†	60	
12	PLY 13	IM7/8552-1 190 gsm 0.5-in. tow	.007†	-60	
13	PLY 15	IM7/8552-1 190 gsm 0.5-in. tow	.007†	0	
14	PLY 16	IM7/8552-1 190 gsm 0.5-in. tow	.007†	0	
15	PLY 17	IM7/8552-1 190 gsm 0.5-in. tow	.007†	45	PADUP PLY
16	PLY 18	IM7/8552-1 190 gsm 0.5-in. tow	.007†	-60	
17	PLY 20	IM7/8552-1 190 gsm 0.5-in. tow	.007†	60	

TABLE D
BETWEEN STATIONS FWD 22 AND AFT 22

SEQUENCE	PLY NUMBER	MATERIAL	THICKNESS	ORIENTATION	COMMENTS
1	PLY 1	IM7/8552-1 190 gsm 0.5-in. tow	.007†	60	
2	PLY 3	IM7/8552-1 190 gsm 0.5-in. tow	.007†	-60	
3	PLY 5	IM7/8552-1 190 gsm 0.5-in. tow	.007†	0	
4	PLY 6	IM7/8552-1 190 gsm 0.5-in. tow	.007†	0	
5	PLY 8	IM7/8552-1 190 gsm 0.5-in. tow	.007†	-60	
6	PLY 10	IM7/8552-1 190 gsm 0.5-in. tow	.007†	60	
7	ADHESIVE FILM	CYTEC FM 209-1M 0.06 PSF	(.010)		FULL COVERAGE
8	CORE	HEXCEL 3.1 1/8 0.0007N 5056	.200 ± .002		AS SHOWN
9	ADHESIVE FILM	CYTEC FM 209-1M 0.06 PSF	(.010)		FULL COVERAGE
10	PLY 11	IM7/8552-1 190 gsm 0.5-in. tow	.007†	60	
11	PLY 13	IM7/8552-1 190 gsm 0.5-in. tow	.007†	-60	
12	PLY 15	IM7/8552-1 190 gsm 0.5-in. tow	.007†	0	
13	PLY 16	IM7/8552-1 190 gsm 0.5-in. tow	.007†	0	
14	PLY 18	IM7/8552-1 190 gsm 0.5-in. tow	.007†	-60	
15	PLY 20	IM7/8552-1 190 gsm 0.5-in. tow	.007†	60	

NASA
LANGLEY RESEARCH CENTER
HAMPTON, VA 23681-2199

DRWN	D. LONG 1/4/1994	SIZE E	DWG. NO. 1295994 REV. D
CHKD		SCALE NONE	SHEET 2 OF 2

1295994 D SHT 2

Figure A1. CTA8.2 fabrication drawing showing the design, LaRC drawing 1295994 Rev. D (concluded).

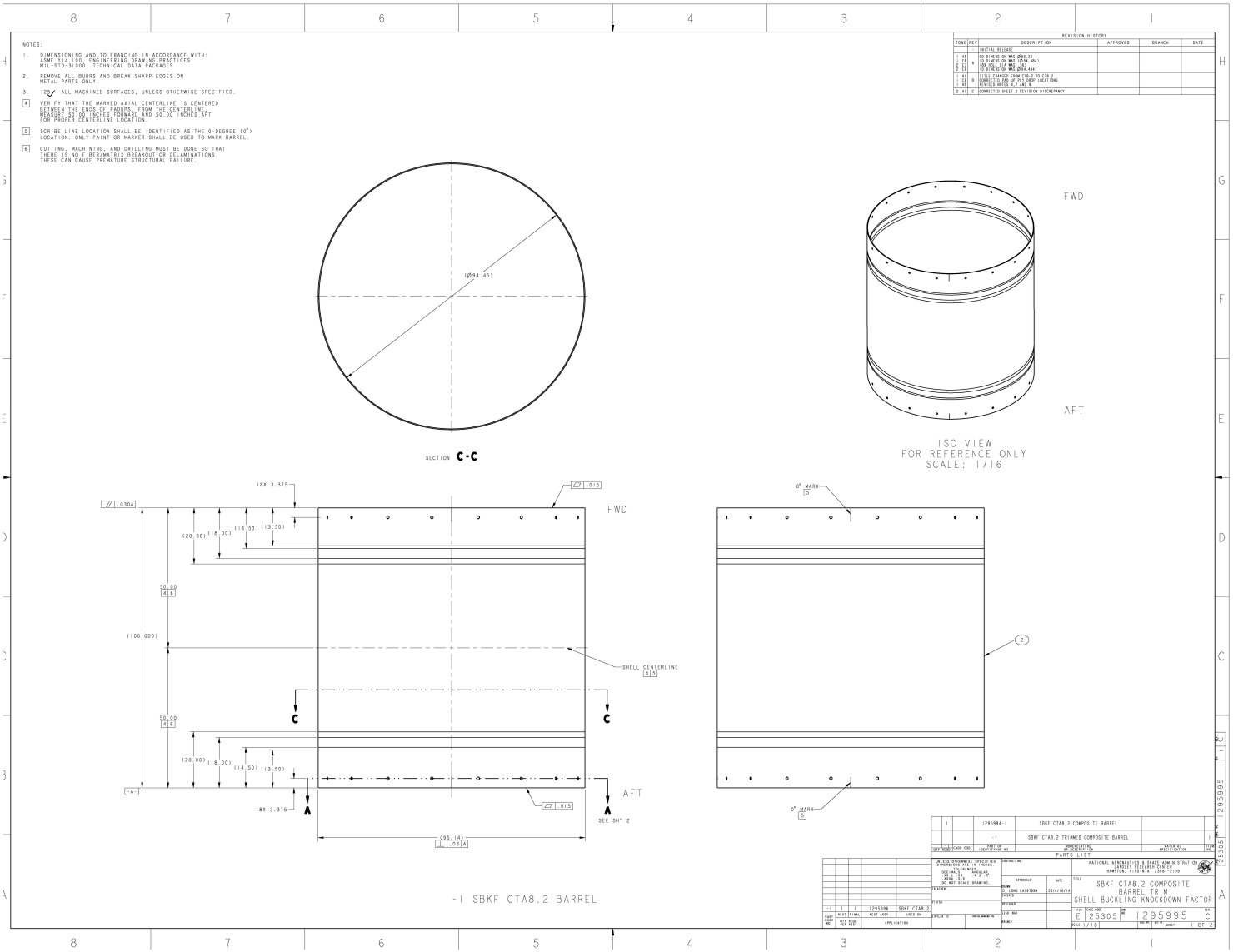

Figure A2. CTA8.2 Trimmed Composite Cylinder, LaRC Drawing 1295995 Rev. C.

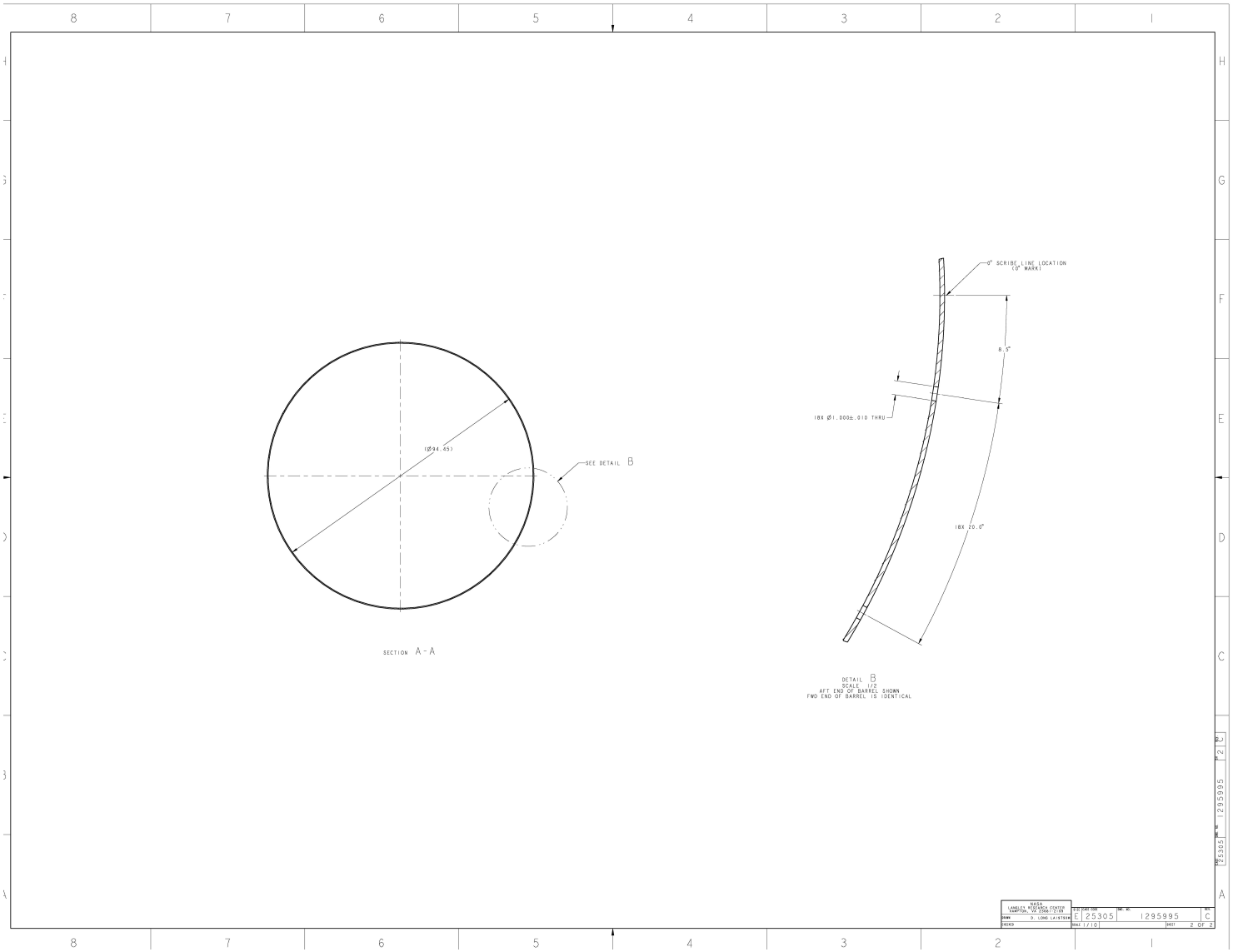

Figure A2. CTA8.2 Trimmed Composite Cylinder, LaRC Drawing 1295995 Rev. C (concluded).

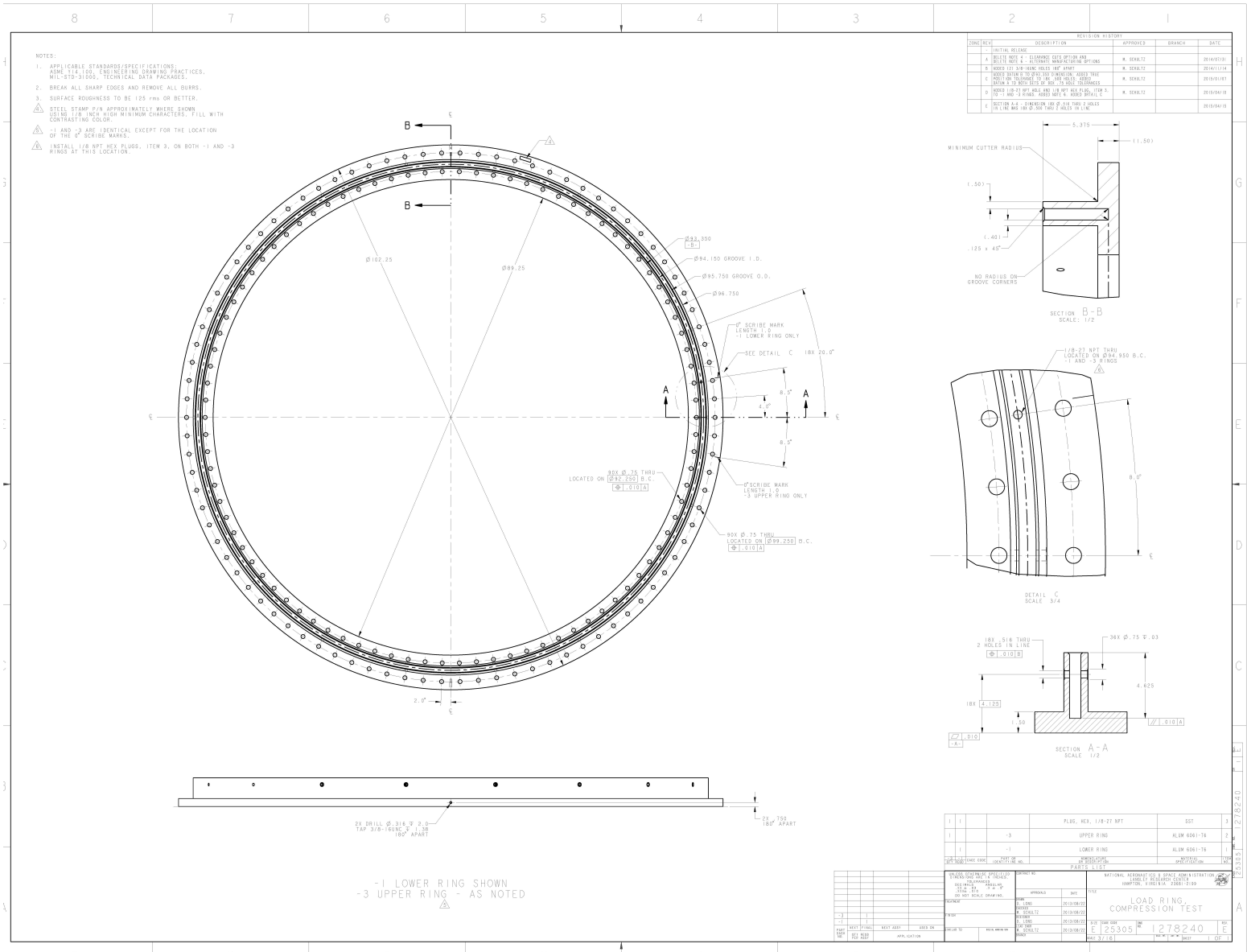

Figure A3. Cylindrical Test Article Aluminum Attachment Ring Design, LaRC Drawing 1278240 Rev. E.

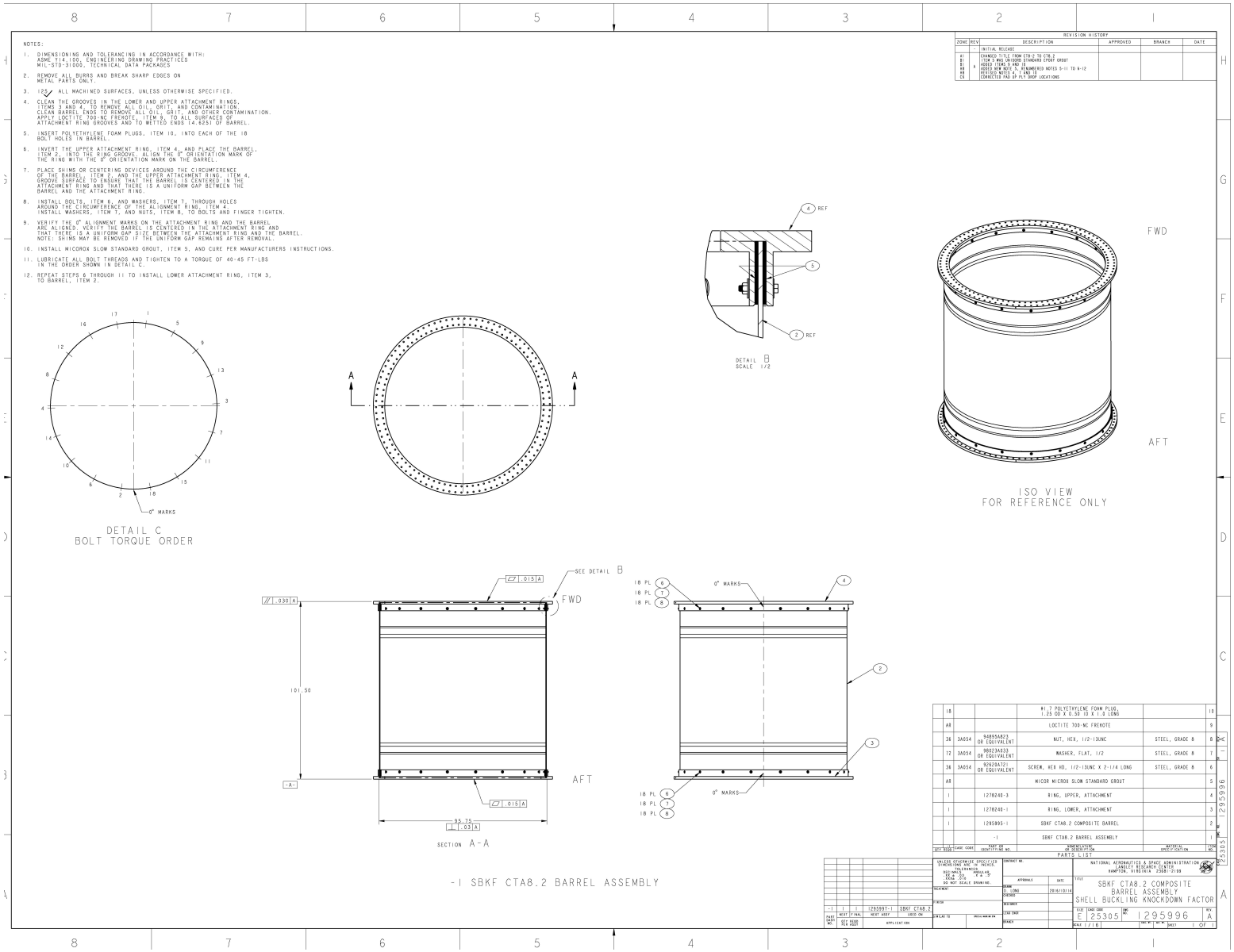

Figure A4. CTA8.2 trimmed and potted in the metallic attachment rings, LaRC drawing 1295996 Rev. A.

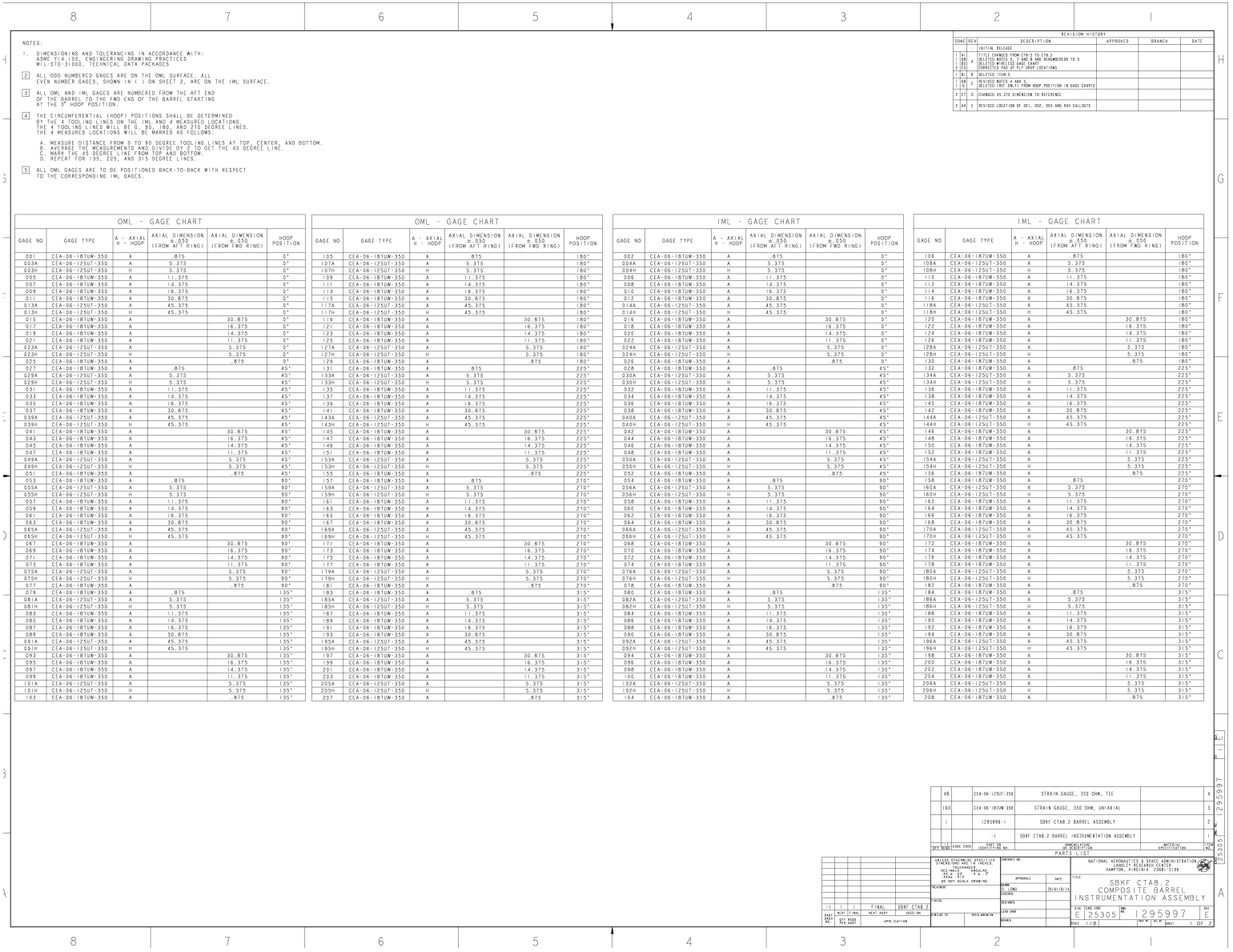

NOTES:

1. DIMENSIONING AND TOLERANCING IN ACCORDANCE WITH: ASME Y14.100, ENGINEERING DRAWING PRACTICES MIL-STD-31000, TECHNICAL DATA PACKAGES
2. ALL ODD NUMBERED GAGES ARE ON THE OML SURFACE, ALL EVEN NUMBER GAGES, SHOWN IN ( ) ON SHEET 2, ARE ON THE IML SURFACE.
3. ALL OML AND IML GAGES ARE NUMBERED FROM THE AFT END OF THE BARREL TO THE FWD END OF THE BARREL STARTING AT THE 0° HOOP POSITION.
4. THE CIRCUMFERENTIAL (HOOP) POSITIONS SHALL BE DETERMINED BY THE 4 TOOLING LINES ON THE IML AND 4 MEASURED LOCATIONS. THE 4 TOOLING LINES WILL BE 0, 90, 180, AND 270 DEGREE LINES. THE 4 MEASURED LOCATIONS WILL BE MARKED AS FOLLOWS:
   A. MEASURE DISTANCE FROM 0 TO 90 DEGREE TOOLING LINES AT TOP, CENTER, AND BOTTOM.
   B. AVERAGE THE MEASUREMENTS AND DIVIDE BY 2 TO GET THE 45 DEGREE LINE.
   C. MARK THE 45 DEGREE LINE FROM TOP AND BOTTOM.
   D. REPEAT FOR 135, 225, AND 315 DEGREE LINES.
5. ALL OML GAGES ARE TO BE POSITIONED BACK-TO-BACK WITH RESPECT TO THE CORRESPONDING IML GAGES.

REVISION HISTORY

ZONE	REV	DESCRIPTION	APPROVED	BRANCH	DATE
	-	INITIAL RELEASE			
1 | A1	A	TITLE CHANGED FROM CTB-2 TO CTB.2			
1 | B8		DELETED NOTES 5, 7 AND 8 AND RENUMBERING TO 5			
2 | B5		DELETED WIRELESS GAGE CHART			
2 | C5		CORRECTED PAD BY FLY DROP LOCATIONS			
1 | B1	B	DELETED ITEM 5			
1 | B8	C	REVISED NOTES 4 AND 5, DELETED (B3) ONLY FROM HOOP POSITION IN GAGE CHARTS			
2 | C7	D	CHANGED 45.315 DIMENSION TO REFERENCE			
2 | A4	E	REVISED LOCATION OF 001, 002, 003 AND 004 CALLOUTS			

OML - GAGE CHART

GAGE NO	GAGE TYPE	A - AXIAL H - HOOP	AXIAL DIMENSION ±.050 (FROM AFT RING)	AXIAL DIMENSION ±.050 (FROM FWD RING)	HOOP POSITION
001	CEA-06-18TUW-350	A	.875		0°
003A	CEA-06-12SUT-350	A	5.375		0°
003H	CEA-06-12SUT-350	H	5.375		0°
005	CEA-06-18TUW-350	A	11.375		0°
007	CEA-06-18TUW-350	A	14.375		0°
009	CEA-06-18TUW-350	A	16.375		0°
011	CEA-06-18TUW-350	A	30.875		0°
013A	CEA-06-12SUT-350	A	45.375		0°
013H	CEA-06-12SUT-350	H	45.375		0°
015	CEA-06-18TUW-350	A		30.875	0°
017	CEA-06-18TUW-350	A		16.375	0°
019	CEA-06-18TUW-350	A		14.375	0°
021	CEA-06-18TUW-350	A		11.375	0°
023A	CEA-06-12SUT-350	A		5.375	0°
023H	CEA-06-12SUT-350	H		5.375	0°
025	CEA-06-18TUW-350	A		.875	0°
027	CEA-06-18TUW-350	A	.875		45°
029A	CEA-06-12SUT-350	A	5.375		45°
029H	CEA-06-12SUT-350	H	5.375		45°
031	CEA-06-18TUW-350	A	11.375		45°
033	CEA-06-18TUW-350	A	14.375		45°
035	CEA-06-18TUW-350	A	16.375		45°
037	CEA-06-18TUW-350	A	30.875		45°
039A	CEA-06-12SUT-350	A	45.375		45°
039H	CEA-06-12SUT-350	H	45.375		45°
041	CEA-06-18TUW-350	A		30.875	45°
043	CEA-06-18TUW-350	A		16.375	45°
045	CEA-06-18TUW-350	A		14.375	45°
047	CEA-06-18TUW-350	A		11.375	45°
049A	CEA-06-12SUT-350	A		5.375	45°
049H	CEA-06-12SUT-350	H		5.375	45°
051	CEA-06-18TUW-350	A		.875	45°
053	CEA-06-18TUW-350	A	.875		90°
055A	CEA-06-12SUT-350	A	5.375		90°
055H	CEA-06-12SUT-350	H	5.375		90°
057	CEA-06-18TUW-350	A	11.375		90°
059	CEA-06-18TUW-350	A	14.375		90°
061	CEA-06-18TUW-350	A	16.375		90°
063	CEA-06-18TUW-350	A	30.875		90°
065A	CEA-06-12SUT-350	A	45.375		90°
065H	CEA-06-12SUT-350	H	45.375		90°
067	CEA-06-18TUW-350	A		30.875	90°
069	CEA-06-18TUW-350	A		16.375	90°
071	CEA-06-18TUW-350	A		14.375	90°
073	CEA-06-18TUW-350	A		11.375	90°
075A	CEA-06-12SUT-350	A		5.375	90°
075H	CEA-06-12SUT-350	H		5.375	90°
077	CEA-06-18TUW-350	A		.875	90°
079	CEA-06-18TUW-350	A	.875		135°
081A	CEA-06-12SUT-350	A	5.375		135°
081H	CEA-06-12SUT-350	H	5.375		135°
083	CEA-06-18TUW-350	A	11.375		135°
085	CEA-06-18TUW-350	A	14.375		135°
087	CEA-06-18TUW-350	A	16.375		135°
089	CEA-06-18TUW-350	A	30.875		135°
091A	CEA-06-12SUT-350	A	45.375		135°
091H	CEA-06-12SUT-350	H	45.375		135°
093	CEA-06-18TUW-350	A		30.875	135°
095	CEA-06-18TUW-350	A		16.375	135°
097	CEA-06-18TUW-350	A		14.375	135°
099	CEA-06-18TUW-350	A		11.375	135°
101A	CEA-06-12SUT-350	A		5.375	135°
101H	CEA-06-12SUT-350	H		5.375	135°
103	CEA-06-18TUW-350	A		.875	135°

OML - GAGE CHART

GAGE NO	GAGE TYPE	A - AXIAL H - HOOP	AXIAL DIMENSION ±.050 (FROM AFT RING)	AXIAL DIMENSION ±.050 (FROM FWD RING)	HOOP POSITION
105	CEA-06-18TUW-350	A	.875		180°
107A	CEA-06-12SUT-350	A	5.375		180°
107H	CEA-06-12SUT-350	H	5.375		180°
109	CEA-06-18TUW-350	A	11.375		180°
111	CEA-06-18TUW-350	A	14.375		180°
113	CEA-06-18TUW-350	A	16.375		180°
115	CEA-06-18TUW-350	A	30.875		180°
117A	CEA-06-12SUT-350	A	45.375		180°
117H	CEA-06-12SUT-350	H	45.375		180°
119	CEA-06-18TUW-350	A		30.875	180°
121	CEA-06-18TUW-350	A		16.375	180°
123	CEA-06-18TUW-350	A		14.375	180°
125	CEA-06-18TUW-350	A		11.375	180°
127A	CEA-06-12SUT-350	A		5.375	180°
127H	CEA-06-12SUT-350	H		5.375	180°
129	CEA-06-18TUW-350	A		.875	180°
131	CEA-06-18TUW-350	A	.875		225°
133A	CEA-06-12SUT-350	A	5.375		225°
133H	CEA-06-12SUT-350	H	5.375		225°
135	CEA-06-18TUW-350	A	11.375		225°
137	CEA-06-18TUW-350	A	14.375		225°
139	CEA-06-18TUW-350	A	16.375		225°
141	CEA-06-18TUW-350	A	30.875		225°
143A	CEA-06-12SUT-350	A	45.375		225°
143H	CEA-06-12SUT-350	H	45.375		225°
145	CEA-06-18TUW-350	A		30.875	225°
147	CEA-06-18TUW-350	A		16.375	225°
149	CEA-06-18TUW-350	A		14.375	225°
151	CEA-06-18TUW-350	A		11.375	225°
153A	CEA-06-12SUT-350	A		5.375	225°
153H	CEA-06-12SUT-350	H		5.375	225°
155	CEA-06-18TUW-350	A		.875	225°
157	CEA-06-18TUW-350	A	.875		270°
159A	CEA-06-12SUT-350	A	5.375		270°
159H	CEA-06-12SUT-350	H	5.375		270°
161	CEA-06-18TUW-350	A	11.375		270°
163	CEA-06-18TUW-350	A	14.375		270°
165	CEA-06-18TUW-350	A	16.375		270°
167	CEA-06-18TUW-350	A	30.875		270°
169A	CEA-06-12SUT-350	A	45.375		270°
169H	CEA-06-12SUT-350	H	45.375		270°
171	CEA-06-18TUW-350	A		30.875	270°
173	CEA-06-18TUW-350	A		16.375	270°
175	CEA-06-18TUW-350	A		14.375	270°
177	CEA-06-18TUW-350	A		11.375	270°
179A	CEA-06-12SUT-350	A		5.375	270°
179H	CEA-06-12SUT-350	H		5.375	270°
181	CEA-06-18TUW-350	A		.875	270°
183	CEA-06-18TUW-350	A	.875		315°
185A	CEA-06-12SUT-350	A	5.375		315°
185H	CEA-06-12SUT-350	H	5.375		315°
187	CEA-06-18TUW-350	A	11.375		315°
189	CEA-06-18TUW-350	A	14.375		315°
191	CEA-06-18TUW-350	A	16.375		315°
193	CEA-06-18TUW-350	A	30.875		315°
195A	CEA-06-12SUT-350	A	45.375		315°
195H	CEA-06-12SUT-350	H	45.375		315°
197	CEA-06-18TUW-350	A		30.875	315°
199	CEA-06-18TUW-350	A		16.375	315°
201	CEA-06-18TUW-350	A		14.375	315°
203	CEA-06-18TUW-350	A		11.375	315°
205A	CEA-06-12SUT-350	A		5.375	315°
205H	CEA-06-12SUT-350	H		5.375	315°
207	CEA-06-18TUW-350	A		.875	315°

IML - GAGE CHART

GAGE NO	GAGE TYPE	A - AXIAL H - HOOP	AXIAL DIMENSION ±.050 (FROM AFT RING)	AXIAL DIMENSION ±.050 (FROM FWD RING)	HOOP POSITION
002	CEA-06-18TUW-350	A	.875		0°
004A	CEA-06-12SUT-350	A	5.375		0°
004H	CEA-06-12SUT-350	H	5.375		0°
006	CEA-06-18TUW-350	A	11.375		0°
008	CEA-06-18TUW-350	A	14.375		0°
010	CEA-06-18TUW-350	A	16.375		0°
012	CEA-06-18TUW-350	A	30.875		0°
014A	CEA-06-12SUT-350	A	45.375		0°
014H	CEA-06-12SUT-350	H	45.375		0°
016	CEA-06-18TUW-350	A		30.875	0°
018	CEA-06-18TUW-350	A		16.375	0°
020	CEA-06-18TUW-350	A		14.375	0°
022	CEA-06-18TUW-350	A		11.375	0°
024A	CEA-06-12SUT-350	A		5.375	0°
024H	CEA-06-12SUT-350	H		5.375	0°
026	CEA-06-18TUW-350	A		.875	0°
028	CEA-06-18TUW-350	A	.875		45°
030A	CEA-06-12SUT-350	A	5.375		45°
030H	CEA-06-12SUT-350	H	5.375		45°
032	CEA-06-18TUW-350	A	11.375		45°
034	CEA-06-18TUW-350	A	14.375		45°
036	CEA-06-18TUW-350	A	16.375		45°
038	CEA-06-18TUW-350	A	30.875		45°
040A	CEA-06-12SUT-350	A	45.375		45°
040H	CEA-06-12SUT-350	H	45.375		45°
042	CEA-06-18TUW-350	A		30.875	45°
044	CEA-06-18TUW-350	A		16.375	45°
046	CEA-06-18TUW-350	A		14.375	45°
048	CEA-06-18TUW-350	A		11.375	45°
050A	CEA-06-12SUT-350	A		5.375	45°
050H	CEA-06-12SUT-350	H		5.375	45°
052	CEA-06-18TUW-350	A		.875	45°
054	CEA-06-18TUW-350	A	.875		90°
056A	CEA-06-12SUT-350	A	5.375		90°
056H	CEA-06-12SUT-350	H	5.375		90°
058	CEA-06-18TUW-350	A	11.375		90°
060	CEA-06-18TUW-350	A	14.375		90°
062	CEA-06-18TUW-350	A	16.375		90°
064	CEA-06-18TUW-350	A	30.875		90°
066A	CEA-06-12SUT-350	A	45.375		90°
066H	CEA-06-12SUT-350	H	45.375		90°
068	CEA-06-18TUW-350	A		30.875	90°
070	CEA-06-18TUW-350	A		16.375	90°
072	CEA-06-18TUW-350	A		14.375	90°
074	CEA-06-18TUW-350	A		11.375	90°
076A	CEA-06-12SUT-350	A		5.375	90°
076H	CEA-06-12SUT-350	H		5.375	90°
078	CEA-06-18TUW-350	A		.875	90°
080	CEA-06-18TUW-350	A	.875		135°
082A	CEA-06-12SUT-350	A	5.375		135°
082H	CEA-06-12SUT-350	H	5.375		135°
084	CEA-06-18TUW-350	A	11.375		135°
086	CEA-06-18TUW-350	A	14.375		135°
088	CEA-06-18TUW-350	A	16.375		135°
090	CEA-06-18TUW-350	A	30.875		135°
092A	CEA-06-12SUT-350	A	45.375		135°
092H	CEA-06-12SUT-350	H	45.375		135°
094	CEA-06-18TUW-350	A		30.875	135°
096	CEA-06-18TUW-350	A		16.375	135°
098	CEA-06-18TUW-350	A		14.375	135°
100	CEA-06-18TUW-350	A		11.375	135°
102A	CEA-06-12SUT-350	A		5.375	135°
102H	CEA-06-12SUT-350	H		5.375	135°
104	CEA-06-18TUW-350	A		.875	135°

IML - GAGE CHART

GAGE NO	GAGE TYPE	A - AXIAL H - HOOP	AXIAL DIMENSION ±.050 (FROM AFT RING)	AXIAL DIMENSION ±.050 (FROM FWD RING)	HOOP POSITION
106	CEA-06-18TUW-350	A	.875		180°
108A	CEA-06-12SUT-350	A	5.375		180°
108H	CEA-06-12SUT-350	H	5.375		180°
110	CEA-06-18TUW-350	A	11.375		180°
112	CEA-06-18TUW-350	A	14.375		180°
114	CEA-06-18TUW-350	A	16.375		180°
116	CEA-06-18TUW-350	A	30.875		180°
118A	CEA-06-12SUT-350	A	45.375		180°
118H	CEA-06-12SUT-350	H	45.375		180°
120	CEA-06-18TUW-350	A		30.875	180°
122	CEA-06-18TUW-350	A		16.375	180°
124	CEA-06-18TUW-350	A		14.375	180°
126	CEA-06-18TUW-350	A		11.375	180°
128A	CEA-06-12SUT-350	A		5.375	180°
128H	CEA-06-12SUT-350	H		5.375	180°
130	CEA-06-18TUW-350	A		.875	180°
132	CEA-06-18TUW-350	A	.875		225°
134A	CEA-06-12SUT-350	A	5.375		225°
134H	CEA-06-12SUT-350	H	5.375		225°
136	CEA-06-18TUW-350	A	11.375		225°
138	CEA-06-18TUW-350	A	14.375		225°
140	CEA-06-18TUW-350	A	16.375		225°
142	CEA-06-18TUW-350	A	30.875		225°
144A	CEA-06-12SUT-350	A	45.375		225°
144H	CEA-06-12SUT-350	H	45.375		225°
146	CEA-06-18TUW-350	A		30.875	225°
148	CEA-06-18TUW-350	A		16.375	225°
150	CEA-06-18TUW-350	A		14.375	225°
152	CEA-06-18TUW-350	A		11.375	225°
154A	CEA-06-12SUT-350	A		5.375	225°
154H	CEA-06-12SUT-350	H		5.375	225°
156	CEA-06-18TUW-350	A		.875	225°
158	CEA-06-18TUW-350	A	.875		270°
160A	CEA-06-12SUT-350	A	5.375		270°
160H	CEA-06-12SUT-350	H	5.375		270°
162	CEA-06-18TUW-350	A	11.375		270°
164	CEA-06-18TUW-350	A	14.375		270°
166	CEA-06-18TUW-350	A	16.375		270°
168	CEA-06-18TUW-350	A	30.875		270°
170A	CEA-06-12SUT-350	A	45.375		270°
170H	CEA-06-12SUT-350	H	45.375		270°
172	CEA-06-18TUW-350	A		30.875	270°
174	CEA-06-18TUW-350	A		16.375	270°
176	CEA-06-18TUW-350	A		14.375	270°
178	CEA-06-18TUW-350	A		11.375	270°
180A	CEA-06-12SUT-350	A		5.375	270°
180H	CEA-06-12SUT-350	H		5.375	270°
182	CEA-06-18TUW-350	A		.875	270°
184	CEA-06-18TUW-350	A	.875		315°
186A	CEA-06-12SUT-350	A	5.375		315°
186H	CEA-06-12SUT-350	H	5.375		315°
188	CEA-06-18TUW-350	A	11.375		315°
190	CEA-06-18TUW-350	A	14.375		315°
192	CEA-06-18TUW-350	A	16.375		315°
194	CEA-06-18TUW-350	A	30.875		315°
196A	CEA-06-12SUT-350	A	45.375		315°
196H	CEA-06-12SUT-350	H	45.375		315°
198	CEA-06-18TUW-350	A		30.875	315°
200	CEA-06-18TUW-350	A		16.375	315°
202	CEA-06-18TUW-350	A		14.375	315°
204	CEA-06-18TUW-350	A		11.375	315°
206A	CEA-06-12SUT-350	A		5.375	315°
206H	CEA-06-12SUT-350	H		5.375	315°
208	CEA-06-18TUW-350	A		.875	315°

ITEM	QTY	PART OR IDENTIFYING NO.	NOMENCLATURE OR DESCRIPTION	MATERIAL SPECIFICATION
4	48	CEA-06-12SUT-350	STRAIN GAUGE, 350 OHM, TEE	
3	160	CEA-06-18TUW-350	STRAIN GAUGE, 350 OHM, UNIAXIAL	
2	1	1295896-1	SBKF CTAB.2 BARREL ASSEMBLY	
1	-1		SBKF CTAB.2 BARREL INSTRUMENTATION ASSEMBLY	

PARTS LIST

DRAWN	DATE
D. LONG	2016|10|18
CHECKED	
RELEASED	
LEAD ENGR	
BRANCH	

CONTRACT NO.

NATIONAL AERONAUTICS & SPACE ADMINISTRATION
LANGLEY RESEARCH CENTER
HAMPTON, VIRGINIA 23681-2199

TITLE
SBKF CTA8.2
COMPOSITE BARREL
INSTRUMENTATION ASSEMBLY

SIZE	CAGE CODE	DWG NO	REV
E	25305	1295997	E

SCALE 1/8 | WT. | SHEET 1 OF 2

DRAWING NEXT ASSY	USED ON
FINAL	SBKF CTA8.2

APPLICATION

NEXT ASSY | PROG MANAGER

DO NOT SCALE DRAWING

UNLESS OTHERWISE SPECIFIED DIMENSIONING & TOLERANCE PER ASME Y14.5M-1994
DECIMALS: X ±.1 XX ±.01 XXX ±.005 ANGLES ±2°

Figure A5. Strain gauge instrumentation, LaRC drawing 1295997 Rev. E.

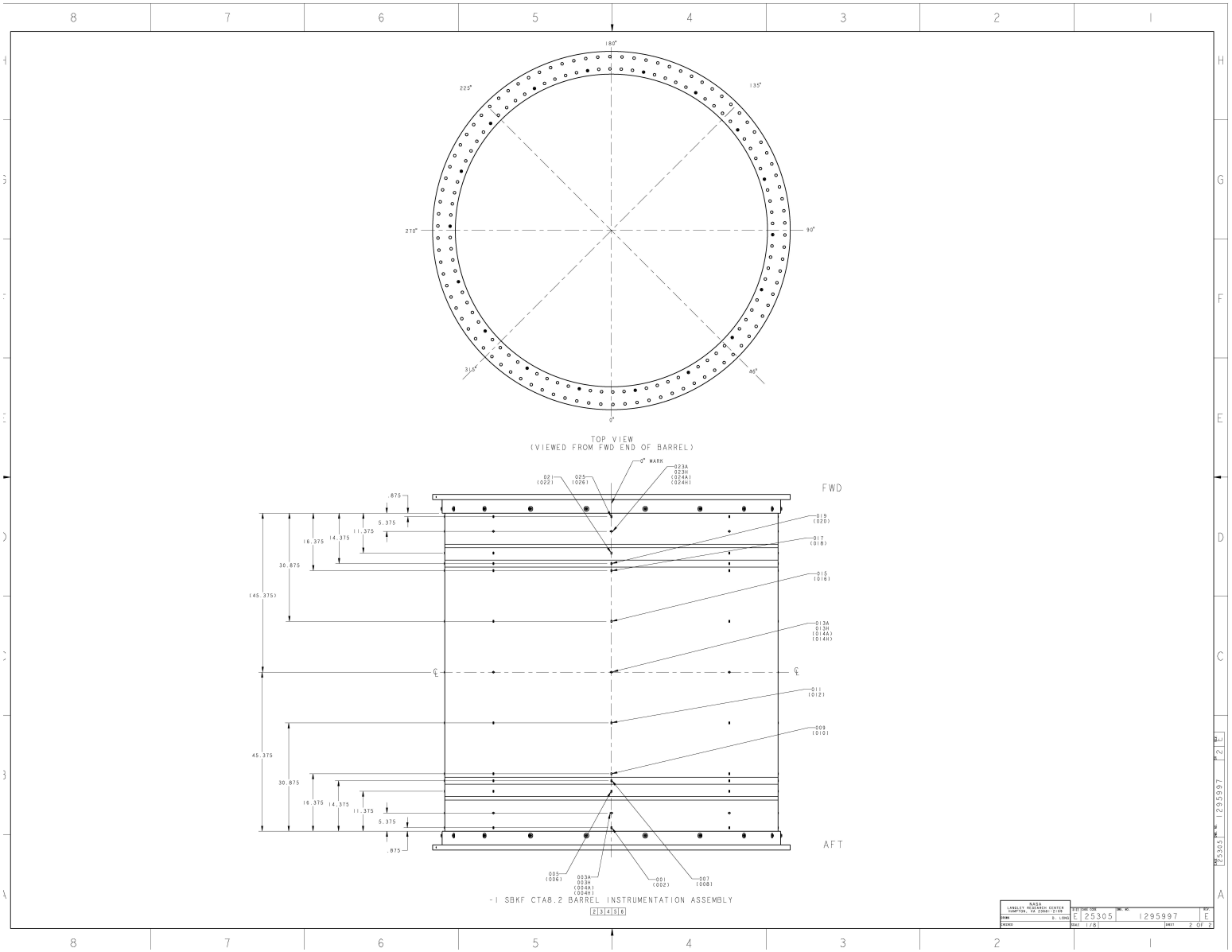

Figure A5. Strain gauge instrumentation, LaRC drawing 1295997 Rev. E (concluded).

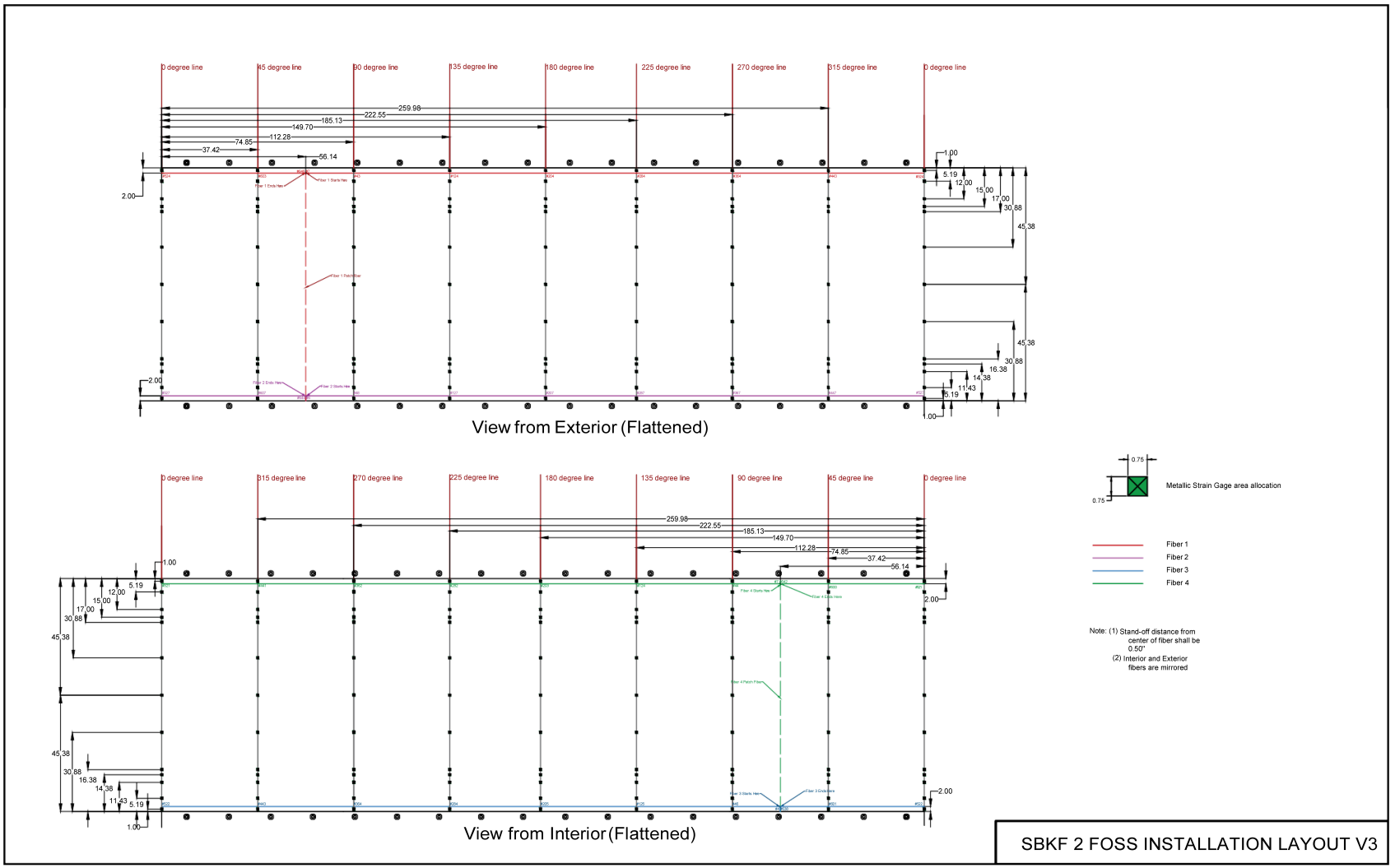

Figure A6. Fiber-optic strain sensor instrumentation drawing (AFRC).

Appendix B – Closed-Form Sandwich Composite Failure Predictions

Classical closed-form equations were used to interrogate the most relevant honeycomb-core sandwich composite failure modes. Specifically, the global buckling load, axial membrane strain at buckling, facesheet wrinkling, facesheet dimpling, and core crimping loads were calculated. The global buckling equation of Reese and Bert [B1], which considers transverse shear compliance in the core, but neglects the in-plane core stiffness, was used to calculate the global buckling load, P_{cr}^{CF},

$$P_{cr}^{CF} = 4\pi\, R\, t_f\, \phi\, \sigma_{cr}^{rc} \left(1 - \frac{1}{2}\frac{\phi\, \sigma_{cr}^{rc\,f}\, t_f\, t_c}{G_{xz}\, h^2}\right) \tag{B1}$$

where R is the radius, t_f is the facesheet thickness, t_c is the core thickness, h is the distance between facesheet midsurfaces, and G_{xz} is the core transverse shear modulus in the axial-transverse plane. The parameter ϕ is given by

$$\phi = \text{Minimum: } 1 \text{ or } \sqrt{\frac{2G_{xz}\left(1+\sqrt{\bar{\nu}_{xy}\,\bar{\nu}_{yx}}\right)}{\sqrt{\bar{E}_x\,\bar{E}_y}}}, \tag{B2}$$

and the parameter σ_{cr}^{rc}, the rigid-core facesheet stress, is given by

$$\sigma_{cr}^{rc\,f} = \frac{h}{R}\sqrt{\frac{\bar{E}_x\,\bar{E}_y}{1-\bar{\nu}_{xy}\,\bar{\nu}_{yx}}}. \tag{B3}$$

The variables $\bar{\nu}_{xy}$ and $\bar{\nu}_{yx}$ are the effective facesheet in-plane Poisson's ratios, and $\bar{E}_x$ and $\bar{E}_y$ are the effective facesheet extensional moduli in the axial and circumferential directions. The effective Poisson's ratios and extensional moduli were calculated with the assumption that the facesheets were balanced and symmetric, even though not all considered facesheets were symmetric, and are given by [B2]

$$\bar{E}_x = \frac{A_{11}^f\, A_{22}^f - A_{12}^{f\,2}}{A_{22}^f\, t_f} \tag{B4a}$$

$$\bar{E}_y = \frac{A_{11}^f\, A_{22}^f - A_{12}^{f\,2}}{A_{11}^f\, t_f} \tag{B4b}$$

$$\bar{\nu}_{xy} = \frac{A_{12}^f}{A_{22}^f} \tag{B4c}$$

$$\bar{\nu}_{yx} = \frac{A_{12}^f}{A_{11}^f} \tag{B4d}$$

where the A_{ij}^f are the facesheet membrane stiffnesses. Using these simplified effective properties was reasonable for the case of this buckling prediction because the sandwich shell itself was balanced and symmetric.

The axial membrane strain at buckling, ε_{cr}, was calculated based on P_{cr}, the cylinder axial stiffness, and the assumption that all the load was carried by the facesheets

$$\varepsilon_{cr} = \frac{P_{cr}}{4\pi\, R\, t_f\, \bar{E}_x}. \tag{B5}$$

The facesheet wrinkling, facesheet dimpling, and core crimping failure loads were calculated based on equations given by Vinson [B3] for honeycomb-core sandwich panels, and assuming pure compression loading of the cylinders. As such, the facesheet wrinkling load, P_{FW}, was calculated as

$$P_{FW} = 4\pi R t_f \sqrt{\frac{2}{3}\frac{t_f}{t_c}\frac{E_C\sqrt{\bar{E}_x\bar{E}_y}}{1-\bar{\nu}_{xy}\bar{\nu}_{yx}}} \tag{B6}$$

where E_c is the effective core transverse shear modulus. The facesheet dimpling load, P_{FD}, was calculated as

$$P_{FD} = 4\pi\, R\, t_f \frac{2\sqrt{\bar{E}_x\, \bar{E}_y}}{1-\bar{\nu}_{xy}\, \bar{\nu}_{yx}}\left(\frac{t_f}{d}\right)^2 \tag{B7}$$

where d is the honeycomb-core cell size. Finally, the core-shear-instability load, P_{CS}, was calculated as

$$P_{CS} = 4\pi\, R\, t_f \frac{G_{xz}\, t_c}{2t_f}. \tag{B8}$$

It is noted that Eq. (B8) is simplified for very thin facesheets. This simplified version was used herein because it predicted more conservative loads than a corresponding equation without this simplification (similar to the equation given in Reference B1 for core shear buckling in terms of facesheet stress). It was more difficult to justify using the simplified effective properties in the equations for P_{FW} and P_{FD} than it was for P_{cr} because these calculations were meant to predict the performance of the individual facesheets. However, the main objective of this initial analysis was to have all other predicted failure loads be 1.4 times higher than the predicted global buckling load to provide reasonable separation between failure modes, and these equations could be used in this capacity. As shown in Section 3.1, the calculated P_{FW} and P_{FD} for all the selected designs were quite high—between nine and 56 times P_{cr}.

Appendix B References

B1. Reese, C. D.; and Bert, C. W.: "Buckling of Orthotropic Sandwich Cylinders Under Axial Compression and Bending," *Journal of Aircraft*, vol. 11, 1974, pp. 207-212.

B2. Hyer, M. W.: *Stress Analysis of Fiber-reinforced Composite Materials*, McGraw-Hill, New York, 1998.

B3. Vinson, J. R.: *The Behavior of Sandwich Structures of Isotropic and Composite Materials*, Technomic, Lancaster, PA, 1999.